**Title**
Searching for New Physics with the Fermi Large Area Telescope



**Author**
Johnson, Arne Christian

**Publication Date**
2019

UNIVERSITY OF CALIFORNIA
SANTA CRUZ

# SEARCHING FOR NEW PHYSICS WITH THE *FERMI* LARGE AREA TELESCOPE

A dissertation submitted in partial satisfaction of the requirements for the degree of

DOCTOR OF PHILOSOPHY

in

PHYSICS

by

Arne Christian Johnson III

March 2019

The Dissertation of Arne Christian Johnson III
is approved:

Professor Steven Ritz, Chair

Professor William Atwood

Professor Jason Nielsen

Lori Kletzer
Vice Provost and Dean of Graduate Studies

# Table of Contents

# List of Figures

# List of Tables

**Abstract**

Searching for New Physics with the *Fermi* Large Area Telescope

by

Arne Christian Johnson III

Compelling astronomical evidence suggests that a majority of the matter in the Universe, known as dark matter, is not described by the Standard Model of paricle physics. Primordial black holes (PBHs), which could have formed in the early Universe from the collapse of primordial overdensities, are a plausible candidate for dark matter. Detecting Hawking radiation from low-mass PBHs would be a monumental achievement in its own right, and the PBH light curve could be exploited as a probe of other physics beyond the Standard Model. Another popular dark matter candidate is weakly interacting massive particles (WIMPs), which are well-motivated in part because they naturally reproduce the correct dark matter relic density in a standard thermal freeze-out scenario. Moreover, WIMP interactions with Standard Model particles can be used to detect WIMPs experimentally with a variety of complementary techniques. The *Fermi* Large Area Telescope (*Fermi*-LAT), which is capable of detecting $\gamma$ rays over a wide range of energies and across the entire sky, is an excellent instrument for studying both of these dark matter candidates. Techniques for detecting the Hawking radiation from evaporating PBHs are developed and used to search the *Fermi*-LAT catalog of $\gamma$-ray point sources for PBH candidates.

The phenomenology of a WIMP model with a velocity-dependent annihilation cross-section is discussed, and an analysis of *Fermi*-LAT data at the Galactic Center is performed to search for the sharp kinematic features in the $\gamma$-ray spectrum predicted by the model. The searches return no significant indications of WIMPs or PBHs, and in both cases the nonobservation is used to place constraints on the presence of new physics.

To my family and friends

## Acknowledgments

The work presented here would not have been possible without the help of a large number of people. First and foremost, I'd like to thank Steve Ritz for being an excellent advisor. I've learned so much from him, and his patience, wisdom, and thoughtfulness never fail to inspire me to be a better scientist.

*Fermi*-LAT is, in large part, the brainchild of Bill Atwood, who I have been fortunate to work with and learn from; I have found his guidance and perspective invaluable over the course of my graduate career.

I'd also like to thank all the members of the *Fermi*-LAT collaboration, who have generously dedicated their time to helping me grow as a physicist. Regina Caputo, as both a collaborator and *Fermi*-LAT Analysis Coördinator, is particularly deserving of thanks, and I'm glad to have worked closely with her.

The work presented in Chapters 5 and 6 are in large part due to Jessie Shelton of UIUC. Jessie has been a terrific collaborator on this project- perpetually answering my naïve questions, patiently working through the beaurocracy of the *Fermi*-LAT collaboration- and for that I thank her.

In addition to Steve and Bill, other UCSC faculty I'd like to especially thank are Robert Johnson, Jason Nielsen, Stefano Profumo, and David Williams, all of whom have engaged me with numerous helpful discussions. The administrative staff in SCIPP, especially Vicki Johnson, have also been tremendously helpful in navigating the department.

I'd also like to express my thanks to the cohort of graduate students in my class: Adam Reyes, Jeff Shahinian, Natasha Woods, Amita Kuttner, and Nico Fernandez. Each of them has helped me with my research, and, more importantly, provided me with great friendship.

Needless to say, I wouldn't be where I am now without my family, who have shown me nothing but love and support. I want thank them for everything they've done for me over the years.

Lastly, I want to thank my friends from the Ultimate community, especially my teammates on Revolver, who have brought me incredible joy during my tenure on the team. I'll miss them.

The text of this dissertation includes reprints of the following previously published material [1]:

- M. Ackermann, W. B. Atwood, L. Baldini, et al. *Search for Gamma-Ray Emission from Local Primordial Black Holes with the Fermi Large Area Telescope.* The Astrophysical Journal, 857 (1): 49, **2018**. ISSN 0004-637X. doi: 10.3847/1538-4357/aaac7b

- C. Johnson, R. Caputo, C. Karwin et al, Search for Gamma-ray Emission from p-wave Dark Matter Annihilation in the Galactic Center, *Physical Review D*, submitted February 2019

The co-author Steve Ritz listed in these publications directed and supervised the research which forms the basis for the dissertation.

The contribution of the author to these publications is as follows: for the publication *Search for Gamma-Ray Emission from Local Primordial Black Holes with the* Fermi *Large Area Telescope* (Chapter 4), the entirety of the modeling and analysis (with the exception of the simple calculations of Section 4.2) were performed by the author; some of the theoretical background, and the calculations of Section 4.2, were performed by the co-authors. For the publication *Search for Gamma-Ray Emission from p-wave Dark Matter Annihilation in the Galactic Center* (Chapter 6), all of the modeling and analysis (with the exception of the systematic uncertainty check mentioned in Section 6.3.2) were performed by the author; the theoretical motivations of Section 6.2 were performed by the co-authors.

# Chapter 1

# Introduction

The Standard Model (SM) of particle physics has enjoyed an extraordinary level of success since its theoretical foundations were put together by Glashow [2], Weinberg [3], Salam [4], and 't Hooft [5, 6] in the late 1960s and early 1970s. Together with Einstein's theory of general relativity (GR), the SM is part of a powerful toolkit that allows today's physicsts to understand Nature on both the smallest and largest of scales.

Experimental results from recent years continue to uphold predictions made by the SM. An illustrative example is the 2012 discovery of the Higgs boson, the final predicted (but unseen) elementary particle in the theory, by the ATLAS [7] and CMS [8] teams at the Large Hadron Collider (LHC). Further analyses [e.g. 9] by ATLAS and CMS have been unable to find any discrepancy between the observed Higgs and the SM prediction. GR has likewise held up under experimental scrutiny: the discovery of gravitational waves in 2015 by the LIGO collaboration [10] provided spectacular confirmation of one of its most interesting predictions.

Yet for all its successes, the SM remains incomplete. A multitude of astronomical observations indicate the presence of large amounts of as-yet-unidentified dark matter, whose energy density dwarfs that of the known SM components. Moreover, although no experiment to date has seen significant deviations from the predictions of GR or the SM, neither theory on its own can successfully describe physics simultaneously at extremely large and small scales.

This chapter provides a broad overview of a few of the problems facing the SM, and introduces some of the general methods by which they have been previously studied by experiment. To find clues to physics beyond the SM, however, it is worthwhile not only to push current experimental techniques to their limits, but to develop novel experimental techniques that reconsider traditional assumptions. The searches for new physics described in Chapters 3–6 are characteristic of this approach.

## 1.1 Dark Matter

### 1.1.1 History

Multiple lines of inquiry have firmly established that a large majority of the mass in the Universe is neither luminous nor composed of SM particles. The first evidence of what we now call the dark matter (DM) were Fritz Zwicky's observations in 1933 that the velocity dispersion of galaxies in the Coma Cluster was far higher than the escape velocity predicted from the mass of the luminous galaxies alone [11]. Zwicky posited that the presence of a large amount of unseen mass (his *dunkle Materie*) allowed the galaxies to remain gravitationally bound in the cluster. Later observations of galaxy clustering, such as Kahn & Woltjer's analysis of the motion of the Andromeda galaxy in 1959 [12], were consistent with this interpretation, finding that an accounting of the luminous mass was insufficient to explain the high observed velocity.

Evidence for DM continued to mount in the 1970s with the advent of telescopes capable of measuring galactic rotation curves—the orbital speed of stars as a function of their distance from their galactic center. With a given distribution of mass, the rotation curve can be predicted in a straightforward manner with Newtonian gravity, and for most galaxies, the visible mass predicts a rotation curve that decreases with distance from the galactic center. Pioneering work done by Rubin & Ford [13] and Roberts & Rots [14] instead showed that the rotation curve of Andromeda was flat out to large distances (30 kiloparsecs) from its center. Further data from Rubin et al. [15] confirmed that the same result held true for nearly all the spiral galaxies in a broad sample considered—see Figure 1.1.

Flat rotation curves are readily explained if the visible galaxy is embedded in a DM halo—a large, spherically symmetric DM distribution [e.g. 16]. However, the inconsistency between Newtonian theory and flat rotation curves does not uniquely point to a DM solution, as proponents of modified Newtonian dynamics (MOND) pointed out in 1983 [17]. MOND is capable of explaining both the observed flat rotation curves and the strong correlation between absolute galactic rotation speeds and luminosity (known as the baryonic Tully-Fisher relation) [18] by introducing an acceleration scale $a_0$ below which Newton's second law is modified to read, approximately, $F = ma^2/a_0$. The

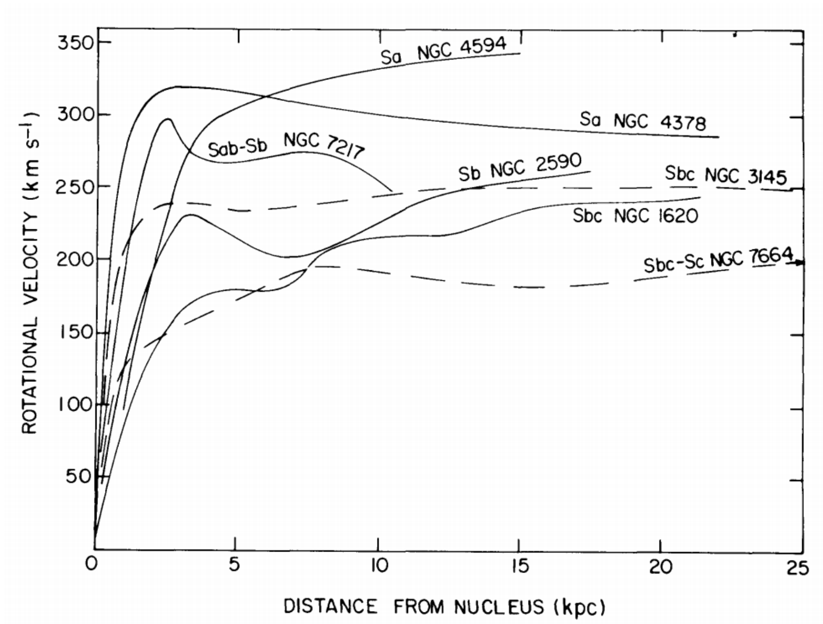


Figure 1.1: Rotation curves of ten spiral galaxies, measured by Rubin et al. by observation of the Hydrogen-$\alpha$ emission line with telescopes at the Kitt Peak and Cerro Tololo observatories. The galaxies, which span a variety of ages and types, consistently have flat or rising rotation curves, consistent with the presence of DM. Figure reproduced from [15].

observed baryonic mass would then be sufficient to explain the dynamics of galaxies; to discriminate between the DM and MOND paradigms, measurements of galactic mass that do not rely on the assumption of Newtonian gravitation are needed.

An independent probe of mass comes from gravitational lensing: in GR, the presence of massive objects causes light from distant sources to be deflected (see [19, 20] for reviews). One of the earliest lensed objects seen was the giant arc in the Abell 370 galaxy cluster, shown in Figure 1.2. Spectroscopic data indicated that the arc did not belong to the Abell 370 cluster, and a subsequent model of the system as a gravitational lens by Soucail et al. in 1987 [21] was in excellent agreement with the data. Crucially, in order to achieve a good fit, the model relied on a smooth DM distribution which dominated the total cluster mass.

A particularly striking example of how gravitational lensing can indicate the presence of DM was given by Clowe et al. [23] in 2006. Comparison of the gravitational lensing by merging galaxies in the Bullet Cluster to an X-ray tracer of the gas content [23] is shown in Figure 1.3. The data show conclusively that although the gas (which dominates the luminous mass of the cluster) is slowed by self-interaction, the bulk of the total mass is nonluminous, and passes through itself apparently unimpeded.

The mystery around the missing mass deepened as it became clear that DM could not be composed of traditional "dark" baryonic matter, such as brown dwarfs. Big Bang nucleosynthesis (BBN)—the process by which heavy (i.e. $Z > 1$) elements are formed in the early Universe—is well understood, and theoretical predictions of primordial element abundance match observations to an extraordinary degree of accuracy.

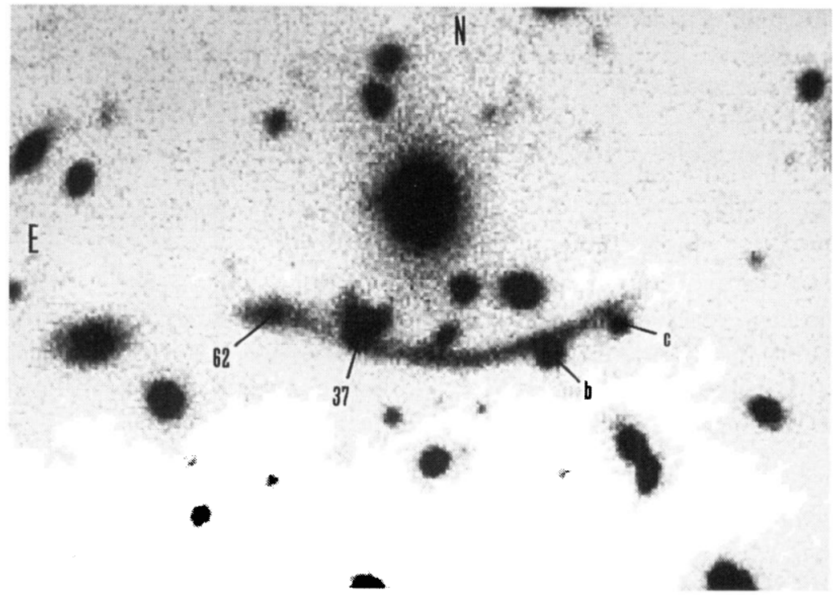


Figure 1.2: Giant arc of Abell 370, first imaged in 1985 with the Canada-France-Hawaii telescope at Mauna Kea. Initial analysis indicated that the arc structure was due to star formation from the infall of gas onto a massive galaxy, but later modeling strongly indicated that the arc was due to the gravitational lensing of a distant galaxy aligned with Abell 370. The gravitational potential needed to reproduce the ring requires an amount of DM that dominates the total mass of the system. Figure reproduced from [22].

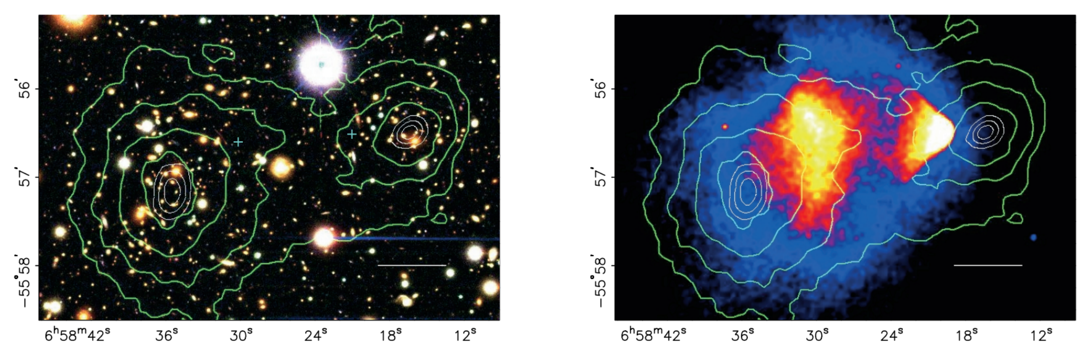


Figure 1.3: *Left panel*: Optical image of the colliding Bullet cluster, taken with the Magellan telescope. *Right panel*: X-ray image of the same region from the Chandra space telescope. In both panels, the white contours show the location of the region of maximum gravitational shear. In both of the colliding regions, the gas content, traced by the X-ray emission, lags behind the bulk of the total mass due to scattering during the collision. Figure reproduced from [23].

BBN calculations turn out to be sensitive to the total density of baryons $\rho_b$, and fits to the data yield $\rho_b/\rho_c \approx 0.04$, where $\rho_c = 0.863 \times 10^{-29}$ g cm$^{-3}$ [24] is the critical density of the Universe—the density above which the Universe is closed and eventually collapses, and below which the Universe is open and expands forever [25]. On the other hand, the density of all matter $\rho_M$ is known to be about $0.3\rho_c$ from a number of independent measurements, including the cosmic microwave background (see below). The scale of the discrepancy is immediately apparent: baryonic matter accounts for less than 15% of the total mass in the Universe!

The cosmic microwave background (CMB) is a powerful probe of physics on a cosmological scale. The CMB is composed of the remnant thermal radiation from the surface of last scattering at a redshift of $z \approx 1100$ (the so-called "recombination" era), as the Universe cooled below the ionization energy of hydrogen. Fluctuations in the CMB temperature have been accurately measured across a wide range of angular scales by several experiments, most recently the *Planck* satellite [26]. The observed fluctuations in the CMB temperature, which originate from acoustic oscillations in the plasma at times prior to recombination, are of the order $10^{-5}$, while models of gravitational clustering require fluctuations near $10^{-3}$ in order to reproduce the amount of structure observed today [27]. A large amount of nonbaryonic mass can resolve this discrepancy by deepening the gravitational wells of density perturbations, allowing structure formation to occur faster.

### 1.1.2 Cold Dark Matter

In cosmology today, DM plays a key role in the successful ΛCDM (cold dark matter with cosmological constant Λ) model of the Universe by seeding the density fluctuations around which galaxies grow. In the ΛCDM model, acoustic fluctuations in the density of photons and charged particles suppress the growth of structure during the radiation-dominated era of the Universe, but once the Universe cools sufficiently to become matter-dominated, the infall of mass onto the potential wells created by initial density perturbations in the DM to grow larger. As the baryonic matter increases in density, it sheds angular momentum and energy via thermal radiation and Compton scattering with CMB photons, allowing it to collapse into familiar structures like stars and galaxies. Structure formation continues in this manner until about a redshift of $z \sim 1$, after which time dark energy comes to dominate the Universe, suppressing further growth of structure [28].

The size of the first structures to form is set by the horizon mass at the time the DM becomes nonrelativistic; prior to this decoupling, density perturbations will be smoothed out by DM free-streaming out of gravitational potential wells. Models of DM can therefore be classified by the time at which they decouple: "hot" DM, for instance, becomes nonrelativistic when the horizon mass is of the order $10^{15}\,\mathrm{M}_\odot$, about the mass of a supercluster [29]. "Warm" DM decouples earlier, and forms initial structures on the scale of galaxies ($10^{11}\,\mathrm{M}_\odot$), and "cold" DM decouples early enough that the smallest structures formed are smaller than typical galaxies. Cold DM tends to be favored over hot and warm DM models because it is the most consistent with observations: hot DM, for instance, predicts that the ratio of baryonic matter to DM should be different in structures of different scales, as larger structures can trap light particles more efficiently. Observations on a wide range of scales instead show a relatively constant ratio[1], consistent with the "bottom-up" approach predicted by cold DM [29].

The CMB angular power spectrum is well-described by the ΛCDM model, and the latest global fits to the *Planck* data yield a DM density of $\Omega_{DM} = \rho_{DM}/\rho_c = 0.258$ and a baryonic density $\Omega_b = 0.0484$ [26]. N-body simulations of galaxy formation with CDM have also shown great success at reproducing the observed large scale structure, and are capable of making concrete predictions about the DM substructure. Future developments will allow simulations to probe the DM halo mass function—the number of DM halos per logarithmic mass bin—to ever-smaller distance scales [28].

Depite its continued success describing astronomical observations, the identity of DM remains unkown. Most of the known massive neutral particles in the Standard Model (e.g. the Higgs or Z bosons, the neutron) decay too quickly to account for the presence of DM in the current era. Neutrinos satisfy the requirements of being massive, neutral, and stable, but the neutrino mass is so small (constrained by measurements of the cosmic microwave background to be $\sum m_\nu < 0.12$ eV [26]) that neutrinos move relativistically, and therefore will free-stream out of gravitational potential wells the size of galactic halos [27].

A variety of candidates for the identity of DM have been proposed, many of

[1]With some interesting exceptions: a recent study of the velocity dispersion in the galaxy NGC1052-DF2, for example, showed that galaxy to be entirely devoid of DM [30]

which require extensions to the SM. These extensions typically predict the existence of new neutral, stable particles, of which some of the most well-motivated are axions (Section 1.1.3) and weakly interacting massive particles (Section 1.1.4).

### 1.1.3 Axions

Axions are hypothetical particles motivated by the strong $CP$ problem—the question of why $CP$ (charge & parity) symmetry is conserved to a high degree in the strong interaction despite the potentially large $CP$-violating phase in the Lagrangian of quantum chromodynamics (QCD). The offending term is [31]:

$$\mathcal{L} \supset \frac{g_3^2\bar{\theta}}{32\pi^2}\epsilon^{\mu\nu\rho\sigma}G^{\alpha}_{\mu\nu}G^{\alpha}_{\rho\sigma} \tag{1.1}$$

where $\epsilon^{\mu\nu\rho\sigma}$ is the totally antisymmetric tensor, $G$ are the gluon fields, $g_3$ is the QCD coupling constant, and $\bar{\theta}$ is an angle known as the strong $CP$ phase. The term in Equation 1.1 is a pure gradient, which typically can be added to a Lagrangian without impact, but nonperturbative processes known as instantons allow it to have physical effects [32]. In particular, if $\bar{\theta}$ is O(1), this term contributes to a neutron electric dipole moment of $d_n \sim 10^{-16}e$ cm [31]. Experiments, however, have constrained $d_n$ to be less than $2.9 \times 10^{-26}e$ cm [33], implying $\bar{\theta}$ is extraordinarily (i.e. one part in $10^{10}$) close to 0.

There are a number of proposed solutions to the strong $CP$ problem—for example, if one of the quarks is massless, the term in Equation 1.1 can be removed by a field redefinition. Observations and QCD lattice calculations suggest that none of the quarks are massless, however [34]. The most well-studied solution to the strong $CP$ problem is to make $\bar{\theta}$ small dynamically by the introduction of a new global U(1) symmetry (the Peccei-Quinn symmetry [35]). As shown by Wilczek [36] and Weinberg [37], the Peccei-Quinn symmetry introduces new pseudoscalar particles, known as axions, that are the Nambu-Goldstone bosons of the theory. The coupling of the axion field $A$ to the gluon fields $G$ is given by:

$$\mathcal{L} \supset -\frac{g_3^2}{32\pi^2}\frac{A}{f_a}\epsilon^{\mu\nu\rho\sigma}G^{\alpha}_{\mu\nu}G^{\alpha}_{\rho\sigma} \tag{1.2}$$

where $f_a$ is the axion coupling constant and $A$ is the axion field. With the addition of the term in Equation 1.2, the strong $CP$ phase $\bar{\theta}$ becomes dependent on the expectation value of $A$, and is 0 when the axion field reaches the minimum of its potential at $\langle A \rangle = 0$. The Peccei-Quinn axion was not compatible with observations, but a simple generalization of the theory by Dine, Fischler, and Srednicki [38] yields an axion that is both extremely light and weakly coupled to ordinary matter, and therefore compatible with experimental results.

Beam-dump experiments and searches for rare decays [39] constrain the axion to be lighter than 1 MeV, while complementary limits from the longevity of red giants and data from SN 1987A [40] require the axion mass to be less than a few meV. On the other hand, the axion mass must be greater than approximately $10^{-6}$ eV in order to not overclose the Universe [41]. Recent calculations with lattice QCD suggest the most viable axion mass range is 1-100 $\mu$eV, with a coupling to photons on the scale of $10^{-17} - 10^{-12}$ GeV$^{-1}$ [42, 43].

If the axion mass is near its lower bound, axions are plausible DM candidates. Compared to standard cold DM, axions are examples of "warm" DM, as they become nonrelativistic at later times and free-stream out of small density perturbations. Therefore axion DM produces far fewer DM halos at low mass, which may allow future gravitational lensing experiments to distinguish between the "warm" and "cold" DM paradigms [44]. A variety of terrestrial experiments [e.g. 45] to search for axions have also been conducted. These experiments generally seek to exploit the axion's small mixing with the electromagnetic field to produce resonant photons [46].

It should be emphasized that axions may exist (and solve the strong CP problem) but still fail to be the DM, if their mass is too high. In addition, relatives of the axion, called axion-like particles (ALPs), can be important building blocks of other DM models. In the hidden sector axion portal (HSAP) model introduced in Chapter 5, for instance, the mediator ALP is not a DM candidate itself, but allows the DM particle to annihilate to SM final states.

### 1.1.4 WIMPs

Weakly Interacting Massive Particles (WIMPs) are a proposed class of particles that generally possess masses and coupling strengths on the order of the electroweak scale (roughly 100 GeV). Although WIMPs can be produced nonthermally (e.g. gravitational pair production of superheavy particles called WIMPZILLAs [47, 48]), thermal production, described in Section 1.1.4.1, naturally lead to the observed relic abundance, which is a powerful motivation for studying WIMPs. WIMPs also present straightforward strategies for detection, which are discussed in Section 1.1.4.2.

#### 1.1.4.1 Thermal WIMP Freeze-out

The early Universe (the era prior to BBN, a few seconds after the Big Bang) was hot and radiation-dominated. In the standard theory, WIMPs are assumed to have been in thermal equilibrium with the rest of the early Universe, i.e. annihilation and production of WIMPs $\chi$ to and from SM states $\chi\chi \leftrightarrow \gamma\gamma, e^+e^-, ZZ, HH$, etc. took place at equal rates. However, as the Universe expanded and cooled below the WIMP rest mass, production of WIMPs would have been suppressed, while annihilation continued. Therefore the WIMP population would have been depleted until the Hubble rate (describing the expansion of the Universe) exceeded the WIMP annihilation rate—in other words, WIMPs ceased to annihilate when they became too diluted. This process of becoming decoupled from the plasma is referred to as freeze-out[2].

The calculation of the WIMP abundance at late times is relatively straightforward: the rate of change in the WIMP number density $n$ in an out-of-equilibrium scenario can be described by the Boltzmann Equation:

$$\frac{dn}{dt} = -3Hn - \langle\sigma v\rangle(n^2 - n_{\rm eq}^2) \tag{1.3}$$

Where $\langle\sigma v\rangle$ is the velocity-averaged WIMP annihilation cross-section, and $n_{\rm eq}$ is the equilibrium WIMP number density. Here $H \equiv \dot{a}/a$ is the Hubble parameter, where $a$ is the scale factor of the Universe and has dimension of length. The first term on

[2]The derivation in this section follows from the pedagogical discussions by Gelmini and Gondolo [41], Tanedo [49], and Kolb and Turner [50]

the right hand side of Equation 1.3 comes from the expansion of the Universe; if the WIMPs are totally decoupled from the rest of the Universe ($\langle\sigma v\rangle = 0$), the solution is straightforward:

$$\frac{dn}{dt} = \frac{-3n}{a}\frac{da}{dt} \quad \longrightarrow \quad n \propto a^{-3} \tag{1.4}$$

with the result that the number density $n$ is simply inversely proportional to the volume, as it should be. In other words, in the absence of annihilation or creation, the total number of particles $na^3$ remains constant as the Universe expands.

The second term on the right hand side of Equation 1.3 captures the dynamics: the WIMP annihilation rate is $\langle\sigma v\rangle n^2$ and the production rate is $\langle\sigma v\rangle n_{\mathrm{eq}}^2$.

It is convenient to reformulate Equation 1.3 in terms of $Y \equiv n/s$, where $s$ is the entropy density. The entropy per comoving volume (i.e. $sa^3$) is taken to be constant, so the time dependence of $s$ is the same as Equation 1.4:

$$\frac{ds}{dt} = -3Hs \tag{1.5}$$

Combining Equations 1.5 and 1.3 and changing variables (by convention) from $t$ to the ratio of the WIMP mass to the temperature T, $x \equiv m_\chi/T$, allows Equation 1.3 to be written as:

$$\frac{dY}{dx} = -\frac{1}{3H}\frac{ds}{dx}\langle\sigma v\rangle(Y^2 - Y^2 eq) \tag{1.6}$$

As the temperature of the Universe drops below the WIMP mass, only particles at the high-energy exponential tail of the Boltzmann distribution are sufficiently energetic to produce WIMPs. Therefore the production of WIMPs (governed by $Yeq$) goes like $e^{-m_\chi/T}$ or $e^x$.

Solving Equation 1.6 requires knowledge of $H(T)$ and $s(T)$. H depends on the energy density $\rho$ and can be found directly from the Friedmann equation of GR:

$$H = \sqrt{\frac{8\pi\rho}{3M_P^2}} \tag{1.7}$$

where $M_P$ is the Planck mass. The dependence of $s$ and $\rho$ on $T$ can be calculated directly from Fermi-Dirac and Bose statistics, with the end result [50]:

$$\rho = \frac{\pi^2}{30} g_{\text{eff}} T_\gamma^4 \qquad s = \frac{2\pi^2}{45} h_{\text{eff}} T_\gamma^3 \tag{1.8}$$

where $g_{\text{eff}}$ and $h_{\text{eff}}$ count the total effective number of degrees of freedom at the photon temperature $T_\gamma$, and are given by:

$$g_{\text{eff}} = \sum_{bosons} g_i \frac{T_i^4}{T_\gamma^4} + \frac{7}{8} \sum_{fermions} g_i \frac{T_i^4}{T_\gamma^4} \qquad h_{\text{eff}} = \sum_{bosons} g_i \frac{T_i^3}{T_\gamma^3} + \frac{7}{8} \sum_{fermions} g_i \frac{T_i^3}{T_\gamma^3} \tag{1.9}$$

where the $g_i$ count the number of internal (i.e. spin) degrees of freedom, and $T_i$ is the effective temperature of species $i$- the temperature at which particle $i$ freezes out. The values of $g_{\text{eff}}$ and $h_{\text{eff}}$ have been computed numerically and are known over many orders of magnitude in $T$, and range in value from about 2 to 100 [51].

Introducing the new variable $\Delta = Y - Yeq$, Equation 1.6 becomes:

$$\Delta' = -Yeq' - \frac{1}{3H}\frac{ds}{dx}\langle\sigma v\rangle\Delta(\Delta + 2Yeq) \tag{1.10}$$

Here and below, the prime symbol ($'$) refers to $\frac{d}{dx}$. Solving Equation 1.10 requires $\frac{ds}{dx}$, which is found by applying the chain and product rules to Equation 1.8:

$$\frac{ds}{dx} = \frac{ds}{dT}\frac{dT}{dx} = \frac{-m_\chi}{x^2}\frac{ds}{dT} = \frac{-m_\chi}{x^2}\frac{2\pi^2}{45}3T^2 h_{\text{eff}}\left(1 + \frac{T}{h_{\text{eff}}}h'_{\text{eff}}(T)\right) \tag{1.11}$$

Substituting Equations 1.8, 1.7, and 1.11 into Equation 1.10:

$$\Delta' = -Yeq' - \langle\sigma v\rangle M_P \frac{m_\chi}{x^2}\sqrt{\frac{\pi}{45}}\frac{h_{\text{eff}}}{g_{\text{eff}}^{\frac{1}{2}}}\left(1 + \frac{T}{3h_{\text{eff}}}h'_{\text{eff}}\right)\Delta(\Delta + 2Yeq) \tag{1.12}$$

Solving Equation 1.12 analytically is difficult (due to the complicated $T$ dependence of $h_{\text{eff}}$ and $g_{\text{eff}}$), but in the late-time limit (i.e. $Yeq = 0$), it simplifies to:

$$\Delta' = -\langle\sigma v\rangle M_P \frac{m_\chi}{x^2}\sqrt{\frac{\pi}{45}}\sqrt{g_*}\Delta^2 \tag{1.13}$$

where $\sqrt{g_*} \equiv \frac{h_{\text{eff}}}{g_{\text{eff}}^{\frac{1}{2}}}\left(1 + \frac{T}{3h_{\text{eff}}}h'_{\text{eff}}\right)$. Integrating Equation 1.13 from the time of freezout ($x_F$) to the present:

$$\int_{\Delta_{x_F}}^{\Delta_\infty}\frac{d\Delta}{\Delta^2} = \langle\sigma v\rangle M_P m_\chi\sqrt{\frac{\pi}{45}}\sqrt{g_*}\int_{x_F}^{\infty}\frac{1}{x^2}dx \tag{1.14}$$

$$\frac{1}{\Delta}\bigg|_{x_F}^{\infty} = \langle\sigma v\rangle M_P m_\chi\sqrt{g_*}\sqrt{\frac{\pi}{45}}\frac{1}{x}\bigg|_{x_F}^{\infty} \tag{1.15}$$

$$\frac{1}{Y_\infty} = \langle \sigma v \rangle M_P \frac{m_\chi}{x_F} \sqrt{g_*} \sqrt{\frac{\pi}{45}} \tag{1.16}$$

Converting to more familiar units, and recalling $Y \equiv n/s$, a simple expression for the cosmological DM density is reached:

$$\Omega_\chi = \frac{s_\infty Y_\infty m_\chi}{\rho_c} = \frac{s_\infty x_F}{\rho_c \langle \sigma v \rangle M_P \sqrt{g_*}} \sqrt{\frac{45}{\pi}} \tag{1.17}$$

Equation 1.12 can also be solved numerically for various values of $\langle \sigma v \rangle$. Several solutions are shown in Figure 1.4- note that higher annihilation cross-sections allow the WIMPs to annihilate for longer times and therefore lead to lower relic abundance, as implied by Equation 1.17 (when it comes to WIMPs, "the weakest wins"). The numerical solutions also show that the freezout time $x_F \approx 20$ is rather insensitive to the WIMP mass and annihilation cross-section [41].

With the value of $x_F = 20$ and other known constants ($s_\infty = 2891$ cm$^{-3}$ [24], $\Omega_\chi = 0.258$, $\rho_c = 0.863 \times 10^{-29}$ g cm$^{-3}$, and $\sqrt{g_*} \approx 8$ is evaluated at the freezout temperature), Equation 1.17 can be rearranged to find the numerical value the cross-section that yields the observed relic abundance:

$$\langle \sigma v \rangle = \frac{s_\infty x_F}{\Omega_\chi \rho_c M_P \sqrt{g_*}} \sqrt{\frac{45}{\pi}} \approx 3 \times 10^{-26}\,\mathrm{cm}^3\,\mathrm{s}^{-1} \tag{1.18}$$

This value (the "thermal relic cross-section") is often canonical in the literature, and is a useful benchmark in searching for SM products of WIMP annihilation (see, for instance, Figures 1.8 and 6.7). If the WIMP freezes out with a characteristic velocity of $v = 0.2c$, then the result of Equation 1.18 corresponds to a mass scale of

$3 \times 10^{-26}\,\mathrm{cm}^3\,\mathrm{s}^{-1}/(0.2\hbar c^3) \approx$ few $\mathrm{TeV}^{-2}$, which is approximately the same scale as the electroweak bosons ($m_Z \approx 90$ GeV, $m_{W^\pm} \approx 80$ GeV, $m_H \approx 125$ GeV).

Tantalizingly, new physics is also expected at the electroweak scale for other reasons, notably the hierarchy problem for the Higgs mass. If the SM Lagrangian is assumed to be the effective field theory of a new, UV-complete theory, the observable Higgs mass is highly sensitive to the parameters in the UV-complete theory, and these parameters must be extremely fine-tuned in order for the physical Higgs mass to be the observed value of $\sim 125$ GeV. But the introduction of new physics at the electroweak scale could potentially allow for these parameters to be O(1), restoring naturalness to the UV-complete theory [31]. The coincidence that new particles (WIMPs) with electroweak-scale cross-section also naturally reproduce the observed DM abundance has been dubbed the "WIMP miracle" [41], and provides more motivation for searches for these potential new particles.

#### 1.1.4.2 WIMP Detection

The same interactions that allow for thermal WIMP production can also be exploited for detecting WIMPs experimentally, so long as WIMPs are stable[3]. Three experimental approaches dominate the search for WIMP dark matter: production, direct detection, and indirect detection (see Figure 1.5).

If WIMPs are not too heavy, high-energy particle accelerators like the LHC can produce WIMPs directly from SM initial states. In this case, the WIMPs (which

[3] In some theories (i.e. SuperWIMPs), WIMPs undergo standard thermal freeze-out, but later decay to other dark particles that are even more weakly coupled to the SM [52].

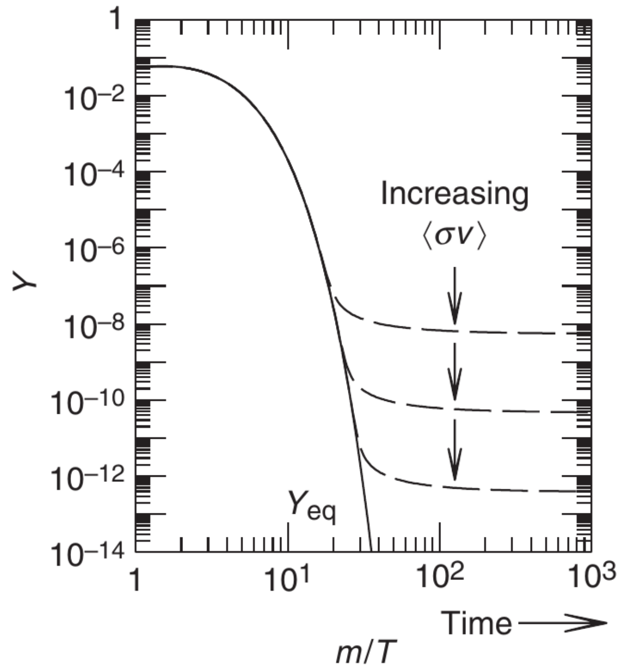


Figure 1.4: Numerical solutions to Equation 1.12, showing the WIMP abundance $Y$ as a function of time. The WIMP abundance tracks its equilibrium value (which decreases like $e^{-m_\chi/T}$) until the Hubble rate exceeds the annihilation rate, at which point the abundance becomes fixed. Increasing the annihilation cross-section leads to a lower relic abundance, and freeze-out takes place at around $x \approx 20$ for most values of $\langle \sigma v \rangle$. Figure reproduced from [41].

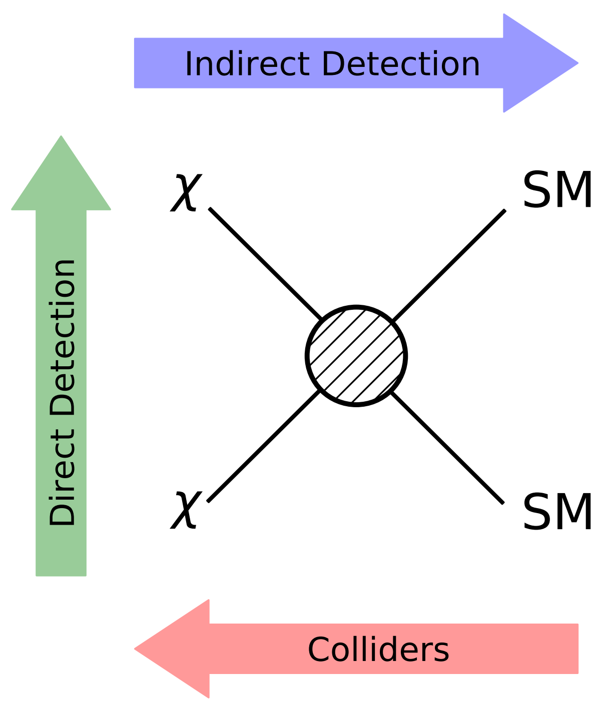


Figure 1.5: Cartoon diagram representing the three major paradigms for detecting WIMP dark matter. Time runs in the direction of the arrow of each experimental approach. The unknown interaction with the SM is represented by the shaded circle.

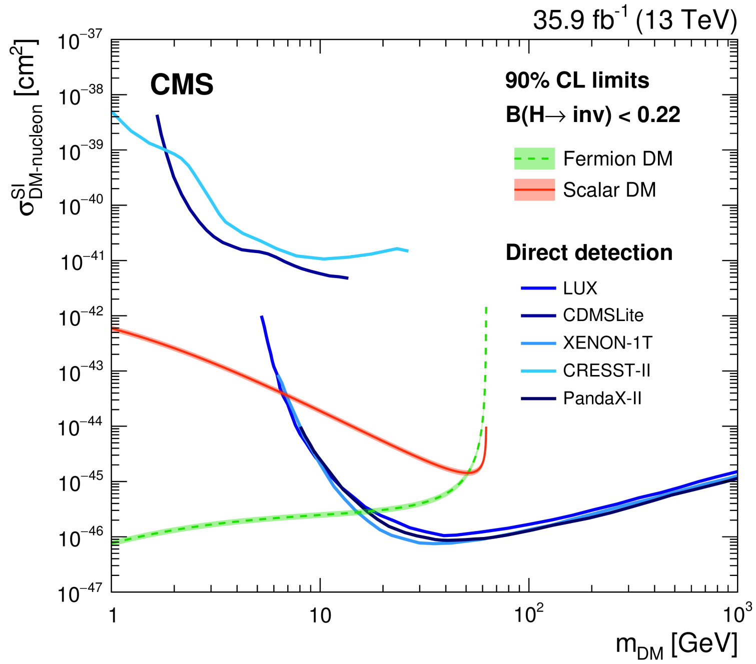


Figure 1.6: Red and green lines show the 95% exclusion on the spin-independent DM-nucleon scattering cross-section from the non-observation of invisible Higgs decays ($H \to \chi\chi$). The collider results compliment the direct detection limits (in blue) by extending them to masses that are kinematically inaccessible to searches with atomic nuclei. Figure reproduced from [54].

are stable, neutral, and weakly interacting) will escape the detector apparatus, leading to missing transverse momentum in the reconstructed final state of particles. Missing transverse momentum is not a smoking gun, however: such searches must contend with significant backgrounds from SM electroweak processes which produce neutrinos. For example, the simplest case of $pp \to \chi\chi + \gamma$ or a jet (where the $\gamma$ or jet comes from initial state radiation) is dwarfed by the background process of $pp \to Z\gamma \to \gamma\nu\bar{\nu}$ or $pp \to Zj \to j\nu\bar{\nu}$ [53]. Instead, collider searches must look for somewhat more complicated signals that are easier to distinguish from SM backgrounds.

Another complication of collider searches for WIMPs is the timescales on which they are sensitive: DM is stable (at least on cosmological timescales), but particles produced in collisions will quickly escape the detector, so only weak bounds on their lifetime can be placed. Therefore, even if a new, neutral particle was discovered at the LHC, complementary techniques from direct or indirect detection experiments would be needed to show that the new particle is consistent with all the characteristics of the DM. By studying the types of interactions and coupling strengths a potential new particle has with the SM, its self-annihilation cross-section could be calculated [31] and compared with results from indirect detection experiments (see below). Colliders results can also be reinterpreted in the context of direct detection experiments, as shown in Figure 1.6.

A robust program of WIMP searches at the LHC has been underway for many years, but results have been in good agreement with the SM (for a recent review, see [55]). For many of the most straightforward models motivated by supersymmetry, LHC results have ruled out new particles less than a few hundred GeV [56]. A next-generation lepton collider, such as the proposed International Linear Collider [57], would have definite initial state energy and polarization, which could help to distinguish signal from background and lead to more robust constraints [58].

Direct detection experiments look for keV-scale deposits of energy from the elastic scattering of incident WIMPs off nucleons in a detector. Because WIMP scattering events are expected to be extremely rare, direct detection experiments are typically performed deep underground to avoid cosmic-ray induced backgrounds, and the experimental apparatuses are built from highly radiopure components. The most sensitive direct-detection experiments to date have employed liquid Xenon (LXe) as a detector medium; in the LXe dual-phase design common to LUX, PandaX-II, and XENON1T, scattered Xe nuclei produce both scintillation and ionization signals that are read out by photomultiplier tubes and electrodes. Comparison between the signals in both channels allows for discrimination against electronic recoils produced by background processes, typically $\beta$-decay of radioactive isotopes. Other detector technologies have been used as well: a highly significant signal in NaI scintillator has been claimed by at least one group [59], based on the expected annual modulation in the WIMP flux from the Earth's orbit. However, the result is in strong tension with results from other experiments, and others [60] have questioned a DM interpretation of the signal.

Direct detection experiments have made rapid progress in recent years, constraining the WIMP-nucleon scattering cross-section to below $10^{-45}$ cm$^2$ for WIMPs with masses between 10 and 1000 GeV. WIMPs with masses below a few GeV are difficult to detect via nuclear recoils in LXe due to unfavorable kinematics, but this is not too disconcerting: in many WIMP models, the scattering process can be described as a simple 4-point interaction that leads to the scattering cross-section being proportional to the square of the WIMP mass. If this is the case, the WIMP mass must be above about 1 GeV to not overclose the Universe (the Lee-Weinberg limit) [61]. At present, the strongest constraints on the WIMP-nucleon scattering cross-section come from the XENON1T experiment [62], which recently overtook the results from LUX [63] and PandaX-II [64] (see Figure 1.7). Future upgrades will continue to improve the sensi-

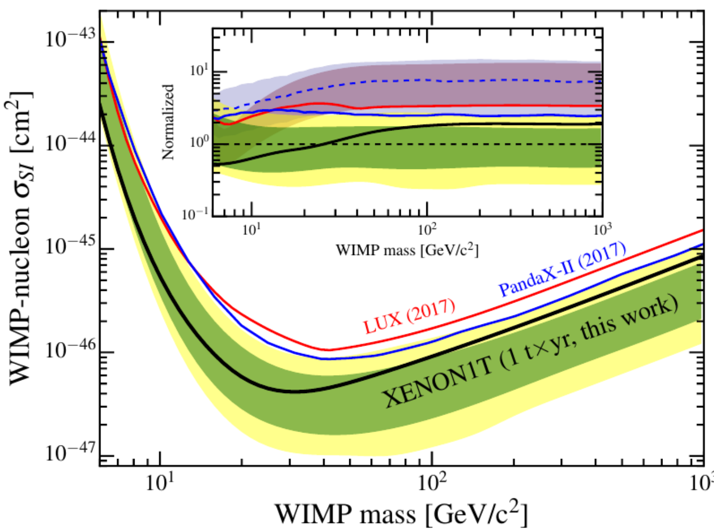


Figure 1.7: 90% confidence upper limit on the spin-independent WIMP-nucleon scattering cross-section from the XENON1T experiment, with 1 tonne-year of data. For low WIMP mass, scattering from a Xe nucleus is kinematically inefficient, while the limit at high mass is subject to the number density of WIMPs. Figure reproduced from [62].

tivity of this class of detectors for the forseeable future, but progress will eventually be limited by an irreduceable background of solar neutrinos, which can mimic nuclear recoil events [65].

Finally, indirect detection experiments observe areas in the Universe where high concentrations of dark matter are believed to exist, searching for SM final states from WIMP annihilation or decay. Searches have been conducted in a variety of channels, typically with neutrinos [e.g. 67, 68] or $\gamma$ rays because they are unaffected by magnetic fields, and therefore point towards the location they originated from. However, indirect detection can also make use of charged particles—some authors have used the observed positron and antiproton fractions observed by, for instance, AMS-02 [69]

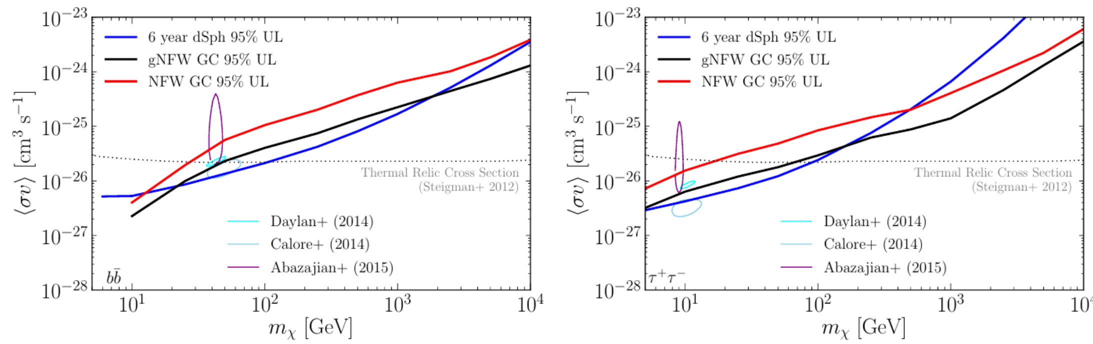


Figure 1.8: 95% confidence upper limit on the WIMP cross-section for annihilation into $b\bar{b}$ (left panel) and $\tau\bar{\tau}$ (right panel) final states in dwarf spheroidal galaxies (blue lines) and at the Galactic center (red, black lines), using data from the *Fermi* Large Area Telescope. The contours show the range of DM masses and cross-sections which result from interpreting the GC excess as WIMP annihilation. Although the countours lie enticingly close to the canonical thermal relic cross-section (grey dashed line), the two interpretations are in tension. Figure reproduced from [66].

to place constraints on the DM annihilation cross-section [70, 71].

In $\gamma$ rays, the strongest signal of DM annihilation is expected to be the Galactic center, due to its proximity and high DM density. A number of studies have indeed seen an excess of $\gamma$ rays at the Galactic center [66], with a spectrum and spatial morphology broadly consistent with DM annihilation [72, 73, 74]. Moreover, the corresponding cross-section is very nearly the canonical value of Equation 1.18. However, the Galactic center has large backgrounds of unresolved point sources and diffuse emission which makes the observed excess difficult to conclusively identify with DM. Complementary limits on the WIMP annihilation cross-section can be placed with studies of dwarf spheroidal galaxies, which are small, DM rich galaxy satellites of the Milky Way whose low $\gamma$-ray backgrounds make them ideal targets for indirect detection searches [75]. The dwarf spheroidal results are in moderate tension (see Figure 1.8) with the interpretation of the Galactic center excess as DM, and other possible interpretations have been proposed to resolve the discrepancy [76, 77].

The observed $\gamma$-ray flux from annihilating WIMPs $\chi$ in the direction $\phi$ is given by:

$$\frac{dN}{dE}(E,\phi) = \frac{\langle\sigma v\rangle}{2m_\chi^2}\sum_i \left(\frac{dN}{dE}\right)_i B_i \times \int_{\text{L.O.S.}} dl(\phi)\frac{\rho(l)_\chi^2}{4\pi} \tag{1.19}$$

Equation 1.19 contains two independent pieces: the integral expression gives the squared DM density along the line of sight, and is known as the $J$-factor; it is estimated from astrophysical models of the DM distribution. Outside the integral are the particle physics terms, involving a sum of the $\gamma$-ray flux over all annihilation channels $i$, multiplied by the branching fraction $B$ of each channel. Because the DM is assumed to be self-annihilating, a factor of 2 is placed in the denominator to avoid double-counting. The factor of $m_\chi^{-2}$, which relates the mass density $\rho_\chi$ to the DM number density, explains the shape of the curves in Figure 1.8—for an observed upper limit on the $\gamma$-ray flux $dN/dE$, the upper limit on the annihilation cross-section $\langle\sigma v\rangle$ goes as $m_\chi^2$.

If the DM annihilates directly to two $\gamma$ rays, kinematics dictates that the $\gamma$ spectrum will be monochromatic. More complicated final states arise from channels that involve annihilation to unstable particles like quarks or heavy leptons, which will generally hadronize and decay, producing a $\gamma$-ray continuum. In these cases, Monte Carlo event generators like Pythia [78] are used to generate the expected $\gamma$-ray spectrum for a given DM model [79]. A single observation can then be used to probe multiple DM models: in Figure 1.8, for instance, the same data is used to consider annihilation into final states of $b\bar{b}$ and $\tau\bar{\tau}$.

Indirect searches for DM annihliation typically assume an annihilation cross-section that is independent of velocity. However, this assumption may be incorrect for a large number of DM models, and searching for velocity-dependent WIMP annihilation via indirect detection methods will be the focus of Chapters 5 & 6.

### 1.1.5 PBHs

Although well-motivated, and despite a multitude of searches conducted, no evidence of particle DM has been found. An attractive possibility is that DM is composed of a population of primordial black holes (PBHs)—black holes that formed from the collapse of overdensities in the early Universe [80]. Producing the correct number of PBHs to account for the present DM density is subject to some theoretical difficulties, but several authors have argued that they could arise naturally in a variety of scenarios, perhaps due to the collapse of cosmic strings [81] or bubble wall creation [82].

PBHs present straightforward detection strategies- heavy PBHs can in principle be detected via the gravitational wave events from their mergers [83]; intermediate-mass PBHs can be constrained by their accretion onto neutron stars and white dwarfs [84] or potentially detected via microlensing events [85]. Low-mass PBHs can potentially be detected by their Hawking radiation; a discussion of PBHs as dark matter candidates and the prospects for detecting low-mass PBHs will follow in Chapter 3.

In addition to their status as DM candidates, PBHs are potential probes of physics at extremely high energy scales. Although GR and the SM excel at describing

Nature on large and small scales, respectively, a full UV-complete theory of quantum gravity remains unknown. Theorists have had some success (see the results in Section 3.2.1, for instance) in describing quantum field theories in a background of curved spacetime, but generally these models neglect perturbative interactions in favor of free fields. As noted by Wald [86], the source of the difficulty in constructing a completely satisfactory theory is rooted in the fact that the metric $g_{\mu\nu}$ is both the dynamical variable of general relativity and the description of the spacetime in which the quantum theory lives. Attempts to construct a UV-complete theory of gravitation by building a quantum field theory for a massless spin-2 field have therefore been unsuccessful, due to the fact that such a theory is nonperturbative at energies above the Planck scale [87]. PBHs provide a natural laboratory for observing physics at the Planck scale, where quantum gravity effects become important: as PBHs evaporate via Hawking radiation, their temperature diverges towards the Planck scale and new physics must describe their dynamics at late times.

## 1.2 Overview of this dissertation

The work that follows presents two analyses that make use of data collected by the *Fermi* Large Area Telescope (*Fermi*-LAT) to search for evidence of WIMP dark matter and low-mass PBHs. This document is laid out as follows: Chapter 2 describes the design of *Fermi*-LAT instrument and provides an overview of the data it has collected. Chapter 3 provides history and context for the low-mass PBH search described in Chapter 4. The phenomenology of an illustrative WIMP DM model that has a velocity-dependent annihilation cross-section is described in Chapter 5, and a search for this model with *Fermi*-LAT data is carried out in Chapter 6. A few concluding thoughts are found in Chapter 7.

# Chapter 2

# *Fermi*-LAT and the Gamma-Ray Sky

This chapter provides an overview of the design and analysis abilities of the Large Area Telescope on board the *Fermi* Gamma Ray Space Telescope (*Fermi*-LAT), with particular emphasis on the features most relevant to the searches described in Chapters 4 and 6. *Fermi*-LAT is an all-sky imaging $\gamma$-ray telescope currently in low-Earth orbit and is capable of detecting photons from about 10 MeV to more than 1 TeV in energy. A complete in-depth description of the LAT design can be found in a technical paper by the *Fermi*-LAT collaboration [88].

## 2.1 History

The field of $\gamma$ ray astronomy begins in earnest with a paper by Morrison in 1958 [89], in which the motivation for making astronomical observations at high energies is laid out. Morrison argued that visible light from high-energy processes is only created indirectly; energetic photons and charged particles originating from the nuclear reactions that power stars, for instance, are thermalized by huge amounts of stellar medium. Other high-energy regions of interest, such as the neighborhoods of neutron stars, are visible, but tend to produce charged particles whose momenta are altered by large-scale magnetic fields. $\gamma$-rays, on the other hand, can be produced both directly (via nuclear de-excitations), or as secondary emission (via bremsstrahlung, inverse Compton scattering, or the formation of neutral pions) from energetic charged particles upon their interaction with matter. Because they are unaffected by magnetic fields, $\gamma$ rays can provide a window directly into these high-energy regions.

A number of experiments were inspired by the ideas that Morrison put forward, including the balloon-based $\gamma$-ray instrument EXP X1, which observed the first extraterrestrial $\gamma$ rays in 1962 [90]. Rapid progress in $\gamma$-ray observation followed, with the launch of the OSO-3 [91], SAS-2 [92], and COS-B [93] telescopes in the late 1960s and 1970s. Because $\gamma$ rays are relatively rare, telescopes were designed to be ever larger in order to accumulate sufficient statistics, culminating in the launch of Energetic Gamma Ray Experiment Telescope (EGRET) [94] in 1991, which was the spiritual predecessor of *Fermi*-LAT [1].

A proposal for the telescope that would eventually become *Fermi*-LAT was first written by Atwood in 1994 [96]. From the beginning, *Fermi*-LAT was designed to be superior to its predecessors in its angular resolution, energy range, effective area, field of view, and lifetime. Over the next 14 years, an international collaboration of scientists and engineers, primarily from the United States, Italy, Japan, France, and

[1] The Italian satellite *Agile* [95], which employed many of the same technologies as *Fermi*-LAT on a smaller scale, was launched in 2008.

Sweden, worked together to build *Fermi*-LAT. On June 11, 2008, the *Fermi* Gamma Ray Space Telescope, carrying both the LAT and its sister experiment the Gamma-ray Burst Monitor (GBM) [97], was launched into low-Earth orbit aboard a Delta II Heavy rocket. Extensive pre-launch tests of the various *Fermi*-LAT components in accelerator test beams and in Monte Carlo simulations contributed to a successful scientific mission: in its ten years in orbit, *Fermi*-LAT has measured the angular positions, energies, and arrival times of over 1 billion photons.

## 2.2 Design

The design of *Fermi*-LAT is informed by the fact that $\gamma$ rays cannot be focused or reflected in the same manner as visible light, as their wavelength $\lambda = \hbar/E_\gamma \sim 10^{-15}\,\mathrm{m}$ (for GeV-scale $\gamma$ rays) is far smaller than typical atomic spacings of $\sim 10^{-10}\,\mathrm{m}$. At energies above a few MeV, $\gamma$ rays preferentially interact with matter via pair production, which comes to dominate over photoexcitation and Compton scattering processes (see Figure 2.1). *Fermi*-LAT takes advantage of this fact by measuring the momenta of electrons and positrons that are pair-produced by incident $\gamma$ rays.

A cartoon schematic of *Fermi*-LAT is displayed in Figure 2.2. The measurement of the $e^+/e^-$ momenta takes place in two main stages: directional information is reconstructed from hits in silicon strip sensors in the tracker (the dark gray columns), while energies are measured via detection of scintillation light in the calorimeter (light gray, bottom of the figure). Although $\gamma$ rays are incident on *Fermi*-LAT from all directions, proper reconstruction requires the $\gamma$ ray to pass through the tracker prior to the calorimeter[2]; given the relatively squat LAT geometry ($1.8\,\mathrm{m} \times 1.8\,\mathrm{m} \times 0.72\,\mathrm{m}$), the total field of view is quite large (approximately 2.4 sr, similar to that of the human eye).

The most important backgrounds for *Fermi*-LAT are primary cosmic rays (energetic protons, nuclei, electrons, and positrons) and secondary particles generated by the interactions of cosmic rays with the atmosphere. The exact background rate varies as *Fermi* orbits the Earth, but is roughly O($10^3$) events per second, compared with a $\gamma$-ray rate of about 2 per second.

*Fermi*-LAT makes use of a variety of techniques to perform background rejection. Pair-conversion is a representative example: charged particle backgrounds are likely to leave only a single track, whereas some $e^+/e^-$ pairs (especially below 1 GeV) will leave separate tracks connected by a vertex. The contamination rate for events with a well-defined pair-conversion vertex is reduced by about an order of magnitude compared with events that only have a single track [99].

### 2.2.1 Tracker

There are 16 individual tracker towers on the LAT, arranged in a 4x4 grid. Each tower has 18 double layers of orthogonally-oriented silicon strip detectors. 16 layers of a high-$Z$ material (tungsten foil) are placed in front of each of the first 16 pairs of silicon strip detectors, providing a location where the $\gamma$ rays preferentially pair-convert.

[2]Events using only the data from the calorimeter have also been analyzed, and can be useful for studying sources at very high energies. However, these events have poor angular resolution as they do not use the information from the tracker, and are not generally included in standard LAT analysis [98].

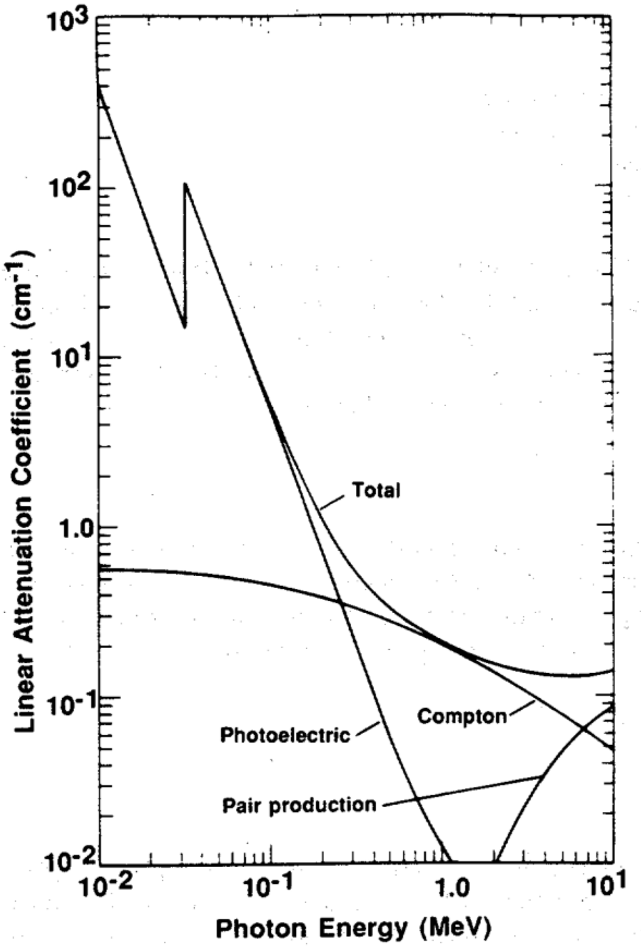


Figure 2.1: Attenuation coefficient of $\gamma$ rays in sodium iodide as a function of energy. At low energy, the dominant form of energy loss is through the photoelectric effect and Compton scattering, while pair production dominates above a few MeV. The sharp feature at 30 keV arises from the excitation of K-band electrons. Figure reproduced from [100].

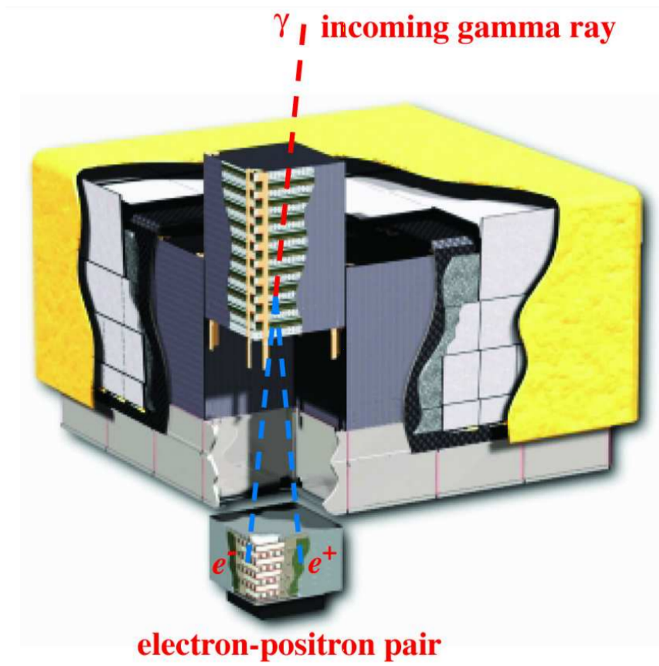


Figure 2.2: Exploded cartoon diagram of *Fermi*-LAT, showing an incoming $\gamma$ ray in red which pair-converts in the tracker into a blue $e^+/e^-$ pair. The $e^+/e^-$ pair come to rest below in the calorimeter. The anticoincidence detector (ACD) is shown as white tiles below the yellow micrometeroid shield. Figure reproduced from [88].

As the pair-produced $e^+/e^-$ traverse the tracker, they undergo Coulomb interactions that impart energy to the electrons in the silicon. If more than about 3.5 eV of energy is transferred to a given electron, it becomes ionized and vacates its position in the atomic lattice, leaving behind a positively charged hole. A voltage applied across the silicon separates the electrons and holes, which are collected and read out by electronics. The positions of the $e^+/e^-$ pair are recorded at each subsequent tracker layer, and a track reconstruction algorithm (based on a Kalman filter) is used to find the path of the $e^+$ and $e^-$.

As the $e^+/e^-$ pairs traverse the tracker layers, they undergo random multiple scattering, which is the predominant source of uncertainty in the reconstruction of the $\gamma$-ray angular position. The root mean square (RMS) multiple scattering angle is given by [101]:

$$\theta_{\mathrm{RMS}} = \frac{13.6\mathrm{MeV}}{\beta cp} Z \sqrt{\frac{x}{X_0}} \left[ 1 + 0.038 \ln\left(\frac{xz^2}{X_0 \beta^2}\right) \right] \tag{2.1}$$

Where $\beta c$ is the speed of the particle, $p$ is its momentum, $z$ is its charge number, and $x$ is the thickness of the material in units of the radiation length $X_0$ (the mean distance over which an electron loses $1/e$ of its energy). Because the RMS deflection is proportional to the square root of the thickness of the scattering layer, there is incentive to minimize the amount of material in the tracker, especially in the high-$z$ tungsten foils. On the other hand, the probability of a $\gamma$-ray conversion is proportional to the thickness of the tungsten, so a compromise between two competing goals (good angular resolution and high conversion efficiency) must be reached. In the LAT, the tracker is segmented into two stages: the first 12 layers (the front) have relatively thin tungsten foils while the last 4 layers (back) are approximately 6 times thicker. The total number of radiation lengths is approximately equal in the front and back segments, though the front-converting photons have somewhat better angular resolution, by roughly a factor of two.

Multiple scattering generally involves a large number of small deflections, so the central limit theorem predicts the resulting angular distribution to be nearly Gaussian. Occasional hard scattering into large angles, however, is somewhat more likely than predicted from a purely Gaussian distribution. Therefore when describing the angular resolution of an instrument like *Fermi*-LAT whose angular resolution is dominated by multiple scattering, it is insufficient to give only the standard deviation of the scattering angle—instead, the typical descriptor is the point spread function (PSF), the angular spread resulting from a perfect point source. The 68% and 95% containment radii of the Fermi-LAT PSF for front- and back- converting photons are shown in Figure 2.3. Notably, the resolution improves dramatically as the energy of the incident photon increases—this is a consequence of the fact that the RMS multiple scattering deflection is inversely proportional to the momentum of the particle.

### 2.2.2 Calorimeter

Behind each tracker tower lies a calorimeter module containing 96 scintillating thallium-doped cesium iodide crystals, with dimensions 2.7 cm × 2.0 cm × 32.6 cm. The crystals are oriented in 8 rows of 12 crystals in an alternating $x - y$ (hodoscopic) array, yielding a total calorimeter depth of 8.6 radiation lengths at normal incidence. As

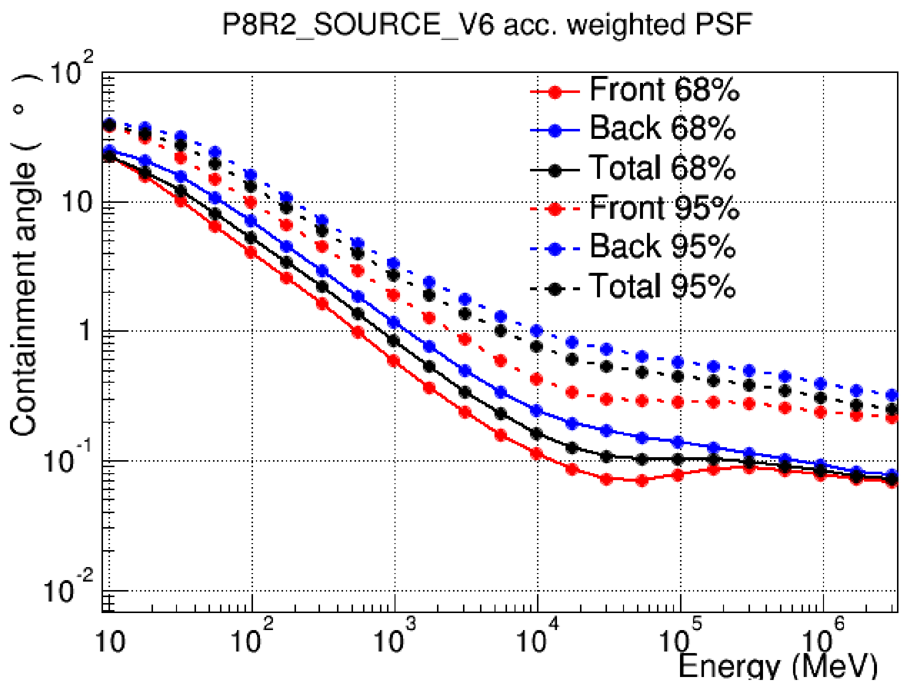


Figure 2.3: 68% and 95% contours of the point-spread function (PSF) of *Fermi*-LAT as a function of $\gamma$-ray energy. The title of the figure ("P8R2_SOURCE_V6 acc. weighted PSF") refers to the particular reconstruction algorithm (the second release of Pass 8 [102]), the event class (how rigorously particle backgrounds are rejected), and the fact that the curve is weighted by the acceptance (the effective area of the LAT integrated over the solid angle). The PSF is dominated by multiple scattering which depends inversely on energy, causing the PSF to improve by about two orders of magnitude between 10 MeV and 10 GeV. Front-converting photons have better angular resolution compared to back-converting photons, because the $e^+$ and $e^-$ from back-converting photons must traverse thicker layers of tungsten, which results in more multiple scattering. Figure reproduced from the *Fermi*-LAT performance website [103].

the primary high-energy electrons and positrons from the tracker encounter the dense calorimeter medium, they radiate secondary photons which in turn pair-convert into more $e^+/e^-$ pairs, generating further photons. The resulting collection of particles, called an electromagnetic shower, continues to grow until the energy of the radiated $\gamma$ rays falls below the rest energy of an electron, at which point pair production ceases. The shape and orientation of the electromagnetic shower are sensitive to the total energy and momentum of the primary electron or positron, and with its segmented calorimeter, *Fermi*-LAT is capable of generating a 3D image of the shower to aid in event reconstruction and background rejection.

Each crystal in the calorimeter is read out by 2 PIN photodiodes on each end, the larger of which covers the energy range 2 MeV - 1.6 GeV, and the smaller of which covers 100 MeV - 70 GeV. The light asymmetry between the two ends of the crystal is used to calculate the location of the energy deposit along the crystal axis, which is used along with the crystal position to give a 3D location of the energy deposit. The raw reconstructed energy is the sum of all the collected energy in the scintillators, subject to corrections (estimated from Monte Carlo studies) for showers that are large enough to escape the detector volume, and for low-energy $\gamma$ rays that can deposit significant amounts of their energy in the material of the tracker. The eigenvectors of the shower shape are then computed and used to guess a preliminary track direction to seed the track reconstruction algorithm.

Beam tests at CERN with electrons fired directly into the calorimeter at an angle of $45°$ from normal resulted in an energy resolution of a few percent for energies above a few GeV. The complete reconstruction of $\gamma$ rays results in an average energy resolution better than 10% between 1 GeV and about 1 TeV (see Figure 2.4), though the value for a given $\gamma$ ray depends on the angle at which the track intersects the calorimeter: the showers from front-converting tracks at a high incidence angle (more than about 70° from normal) are less contained by the calorimeter and therefore have poor energy resolution [103].

The calorimeter is also useful for rejection of particle backgrounds: tracks that are not associated with a deposit of energy in the calorimeter are more likely to be associated with backgrounds. The task of discriminating against backgrounds is left to a series of classification trees (CTs), which are machine learning algorithms trained, in this case, on data from Monte Carlo simulations. Points of information, including the shower profile in the calorimeter and the topology of the track(s) in the tracker, are fed into the CTs, which generate a probability of an event being a non-$\gamma$ particle background [88]. *Fermi*-LAT data is classified by the quality of its reconstruction and the purity against particle backgrounds, as different analyses can have different purity requirements.

### 2.2.3 Anticoincidence Detector

Surrounding the tracker and calorimeter is a segmented anticoincidence detector composed of scintillating plastic, whose purpose is the rejection of charged particle backgrounds from cosmic rays. The material of the ACD is chosen to be low-$Z$ so as to not absorb $\gamma$ rays, and to not provide a location for incident protons to generate pions

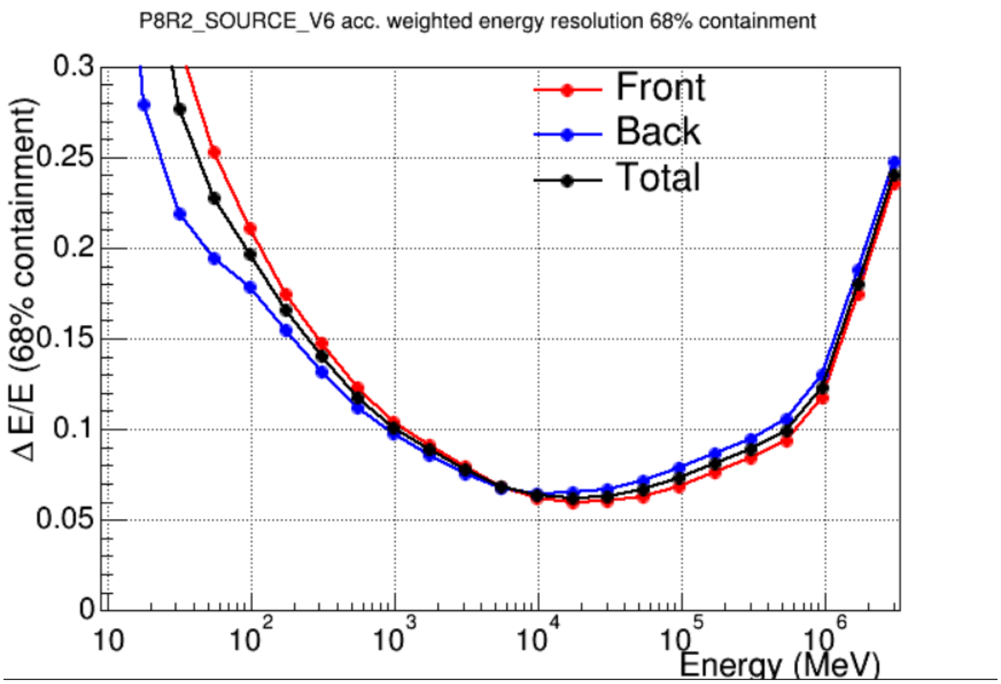


Figure 2.4: Energy resolution of *Fermi*-LAT as a function of the energy of the incident $\gamma$ ray. The title includes the same information as described in the caption of Figure 2.3. At high energy, the electromagnetic shower is able to leak out of the calorimeter and corrections to the deposited energy must be made, increasing the uncertainty. Figure reproduced from the *Fermi*-LAT performance website [103].

(which would generate a substantial background by subsequent decay to two $\gamma$ rays). Events are vetoed only if the ACD triggers at a position consistent with reconstructed track, which prevents spurious vetos from backsplash—an effect that occurs when the EM shower in the calorimeter causes the emission of secondary particles that strike the ACD. By segmenting the ACD into 89 tiles, these self-veto events are present for less than 20% of the photons at 300 GeV, compared to 50% at 10 GeV for the non-segmented EGRET.

### 2.2.4 Data

*Fermi*-LAT most often operates in survey mode, during which it scans the entire sky with roughly uniform exposure on a time scale of about 3 hours (or 2 orbital periods). However, alternate observing patterns also take place, such as when *Fermi*-LAT reorients itself to observe the potential afterglow of a LIGO event, or points towards a flaring blazar for an extened period. Other interruptions to regular data collection include the times *Fermi* traverses the South Atlantic Anomaly (during which the background rate becomes extremely high), and the handful of orbits during which *Fermi* has faced the Earth in order to detect terrestrial gamma-ray flashes from lightning. The pointing history is recorded and available for download with the rest of the *Fermi*-LAT data, and is used for calculating the integrated exposure in a given direction.

Shortly after launch, the *Fermi*-LAT collaboration began a campaign of on-orbit calibration and improvements to the event reconstruction algorithm. So-called "ghost" events, in which arrival of multiple photons in a short amount of time leads to degraded reconstruction accuracy, were found in the real data but were not present in the Monte Carlo simulations (which simulated the arrival of individual photons only) [104]. Two major advances in the event reconstruction algorithms that take into account these types of on-orbit effects, named Pass 7 [105] and Pass 8 [102], resulted in increased acceptance (especially at energies below 300 MeV), and improved angular and energy resolution. The latest event reconstruction (Pass 8 R2) classifies photons based on the quality of the event reconstruction; the best-quality photons at ∼TeV energies have a 68% containment radius nearly an order of magnitude smaller than the overall Pass 7 reconstruction.

Data collected by *Fermi*-LAT is downloaded via radio link, and sent on to SLAC National Accelerator Laboratory for processing to reconstruct the photons and reject backgrounds. The vast majority of photons detected by *Fermi*-LAT are available for download to the public from the Goddard Space Flight Center website within 10 hours of their detection.

## 2.3 $\gamma$-Ray Sky

A typical *Fermi*-LAT $\gamma$ ray has an energy in the GeV range. An approximate measure for the corresponding temperature of such a photon is given by $E/k = 10^{13}$ K; for comparison, the temperature at the center of the Sun is approximately $10^7$ K. Most GeV-scale $\gamma$ rays are therefore produced via nonthermal processes.

Relativistic charged particles are the primary source of the observed $\gamma$ rays seen by *Fermi*-LAT: they emit synchrotron radiation in the presence of magnetic fields, radiate bremsstrahlung upon interactions with matter, and can upscatter starlight or CMB photons via inverse Compton scattering. High-energy protons can interact hadronically with interstellar gas, producing neutral pions which then decay to two $\gamma$ rays. Excited nuclei, such as those produced in supernovae, can de-excite via the emission of $\gamma$ rays—this occurs notably in the afterglow of Type 1a supernovae [106]. Other, more exotic sources of $\gamma$ rays are also possible—Chapter 1 discussed the potential for WIMP dark matter to annihilate to final states that include $\gamma$ rays. With this in mind, it is not surprising that the $\gamma$-ray sky looks rather different from visible sky—see Figure 2.5.

The $\gamma$-ray sky is also variable over a wide range of timescales. The most highly variable sources, millisecond pulsars and $\gamma$-ray bursts, are variable on timescales of less than a second to tens of seconds. Active galaxies, described below, exhibit variability in their $\gamma$-ray flux on timescales ranging from days to months [107]. Some sources are variable over even longer periods; the blazar PG 1553+113, for instance, shows quasiperiodic oscillations in its $\gamma$-ray flux with a period of about 2 years, although the mechanism by which its oscillations are driven is not yet fully understood [108].

### 2.3.1 Diffuse Emission

Much of the sky's $\gamma$-ray emission in the Galactic plane is due to energetic charged particles (cosmic rays) hadronically interacting with the interstellar medium. These interactions produce neutral pions, which then decay to two $\gamma$ rays, whose energy depends on the initial energy of the cosmic ray. The origin of high-energy cosmic rays

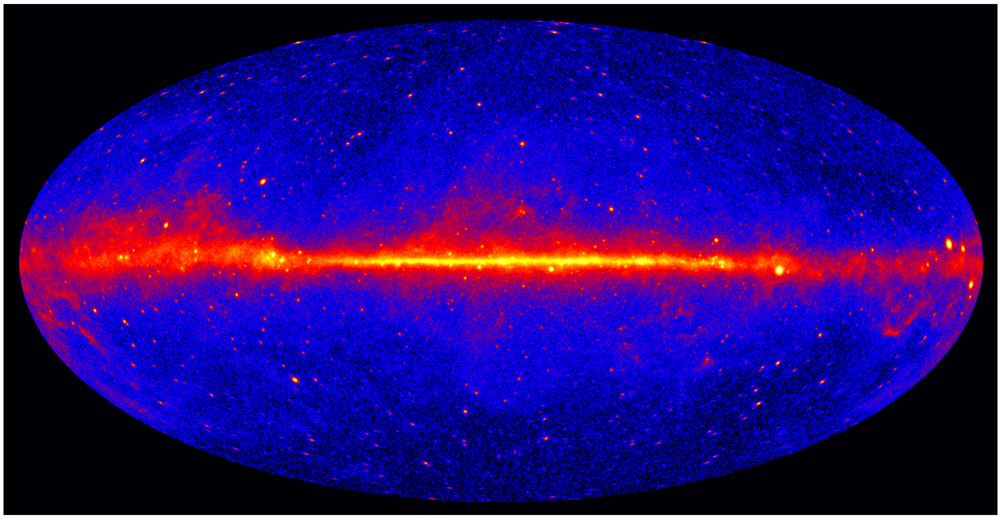

Figure 2.5: False-color image of the *Fermi* sky above 1 GeV in Galactic coordinates with 5 years of data. Warmer colors indicate the location of higher $\gamma$-ray flux. The Galactic plane is prominently seen across the center of the image, and a large number of point sources are visible above and below the plane. Image credit: *NASA/DOE/Fermi-LAT Collaboration*

was a mystery for some time, as second-order Fermi acceleration seemed insufficient to produce particles with GeV-scale energies [109]. A number of authors in the 1970s [e.g. 110], however, discovered that collisionless shock boundary of supernova remnants could sufficiently energize charged particles. At the shock boundary, the magnetic field is nearly discontinuous, and first-order Fermi acceleration is sufficient to give protons many GeV of energy. Models of the galactic diffuse emission are generated by the *Fermi*-LAT collaboration by fitting templates of interstellar emission at several wavelengths to observed regions of the $\gamma$-ray sky [111].

Some diffuse emission extends beyond the Galactic plane, and appears to be isotropic across the sky. Much of this isotropic component likely originates from unresolved point sources (see below) and truly diffuse processes such as the formation of large-scale structure [112], though some backgrounds of cosmic-rays also contribute [113].

### 2.3.2 Point Sources

Most large galaxies contain a rapidly rotating supermassive black hole at their center [114], some of which actively accrete material. These so-called active galaxies possess two main features—a thermal accretion disk, and a relativistic jet of charged particles aligned along the black holes rotation axis. When the Earth lies in the direction of the jet axis, the active galaxy is called a blazar.

Jets in active galactic nuclei (AGN) are believed to derive their power directly from the rotational energy of the supermassive black hole. Via the Blandford-Znajek process [115], magnetic fields from the accretion disk reach inside the black holes ergosphere, causing them to be twisted into a helical shape. The electric fields induced by these rapidly rotating magnetic fields are powerful, and cause charged particles to be accelerated to high speeds along the jets. These relativistic particles can then emit $\gamma$ rays via synchrotron radiation, bremsstrahlung, or inverse Compton scattering [107]. Blazars can be seen across the entire electromagnetic spectrum, and are the most numerous type of point source seen by *Fermi*-LAT.

Rapidly rotating neutron stars, known as pulsars, are surrounded by extraordinarily powerful and rapidly rotating magnetic fields. As electrons stripped from the neutron star surface interact with these magnetic fields, they emit synchrotron radiation that is observable in $\gamma$ rays. A small fraction of pulsars have periods smaller than 1 second, and are referred to as millisecond pulsars; a novel and unresolved population of millisecond pulsars may exist near the Galactic center and contribute to the $\gamma$-ray excess that has been observed there by a number of authors [116].

The brightest region in the gamma-ray sky by far is the Galactic center, containing the supermassive black hole at the center of the Milky Way coincident with the radio source Sagittarius A* (Sgr A*). A number of models have been proposed to explain the gamma-ray emission at Sgr A*, generally involving charged particles injected into the region by tidal disruption of stars. Upon interaction with the surrounding medium and magnetic fields, these charged particles emit synchrotron and bremsstrahlung radiation, and protons undergo hadronic interactions [117]. Other sources of $\gamma$ ray emission in the $\sim$ 300 pc region around Sgr A* include supernova remnants, pulsars, and star-forming regions [118]. As discussed in Chapter 5, some DM models predict annihilation to occur in the region surrounding Sgr A* as well, which may lead to additional $\gamma$-ray emission.

## 2.4 Analysis Tools

*Fermi*-LAT data and LAT-specific analysis tools are publicly available for download from the Fermi Science Support Center at NASAs Goddard Space Flight Center[3]. Processing *Fermi*-LAT data for analysis begins by removing photons (via the tool `gtselect`) that are incident from angles far from the zenith, as these mostly originate from cosmic ray interactions with the atmosphere (the Earth's limb). For a typical

[3] `https://fermi.gsfc.nasa.gov/ssc`

analysis, the photons are then binned (with the use of the tool `gtbin`) in angular position and energy. The LAT effective area is convolved (by use of the tool `gtltcube`) with its pointing history over the time period considered to produce an exposure map binned in energy and angular position.

A standard *Fermi*-LAT analysis makes use of the maximum likelihood technique to test differing hypotheses (e.g., spectral features or angular location) about the source(s) in question. The process begins by defining a model of the region of interest (ROI), typically composed of a list of catalog sources and their associated spectral shapes, locations, and spatial morphology. With the model and a map of *Fermi*-LAT exposure in the ROI, the expected number of photons $\mu_i$ in each bin $i$ can be computed and compared to the actual counts $n_i$. The value of the likelihood $\mathcal{L}$ for the model is then given by the product of Poisson factors over the number of bins $N$:

$$\mathcal{L} = \prod_{i=1}^{N} \frac{\mu_i^{n_i}}{n_i!} e^{-\mu_i} \tag{2.2}$$

Maximizing the likelihood is then equivalent to finding the best-fit parameters for the model. The Jacobian of the likelihood at its maximum is the Fisher information matrix, which gives the correlation between different components of the model.

*Fermi*-LAT analyses often seek to discriminate between two competing hypotheses: if a sharp spectral feature is present or not, for example. In the maximum-likelihood framework, evaluating the statistical significance of a hypothesis $H$ is straightforward: the likelihood is maximized twice, once for the null hypothesis (yielding $\mathcal{L}_0$), and once for the hypothesis of interest (yielding $\mathcal{L}_H$). For cases with sufficient statistics and that satisfy Wilks's criteria [119], the value of the likelihood ratio test statistic (TS) $2\log(\mathcal{L}_H/\mathcal{L}_0) = 2\Delta\log\mathcal{L}$ is distributed as a $\chi^2$, with a number of degrees of freedom equal to the difference in numbers of degrees of freedom between the competing hypotheses. If this is the case, the significance of the varied parameter can be determined by looking up the $p$-value associated with the $\chi^2$ distribution; if this is not the case, the significance can be determined through a Monte Carlo study to find the actual distribution of $2\Delta\log\mathcal{L}$.

### 2.4.1 Catalogs

The *Fermi*-LAT collaboration has used these techniques to compile several catalogs of $\gamma$-ray sources. The most current general-purpose catalog is the Third Fermi Source Catalog (3FGL)[120][4], which lists sources that are significant in the energy range 100 MeV-316 GeV. The 3FGL contains 3033 sources, of which a majority (3008) are point sources and 25 are modeled as extended. Among point sources, the most common class is active galactic nuclei (AGN), accounting for 1720 sources, while most of the remaining sources are pulsars or nebulae associated with pulsars (190 sources), or supernova remnants (72 sources). Because they are extragalactic, AGN are distributed isotropically across the sky, while sources of Galactic origin (pulsars and supernova remnants, for instance) are primarily located along the Galactic plane.

A sizable component (1010 sources) are unassociated with sources seen in other wavelengths and are therefore unidentified. Unassociated sources can be found at both

[4] A forthcoming catalog covering 8 years of data, the 4FGL, should be released in 2019; a preliminary list of sources in it is available at `https://fermi.gsfc.nasa.gov/ssc/data/access/lat/fl8y/`

high latitude and along the plane, and likely fall into one of the previous classes, though they have also been investigated as candidates for DM subhalos [121] and other new physics.

Building an all-sky source catalog is a difficult task, since finding the spectral and spatial parameters of all sources is equivalent to optimizing the likelihood over a high-dimensional space. To simplify the problem, the sky is tiled into 1728 spatial bins using HEALPix (Hierarchecal Equal Area isoLatitude Pixelization)[122], each of which is approximately $5^\circ \times 5^\circ$. A preliminary list of sources is modeled, and the likelihood is maximized in each HEALPix bin by varying the spectral parameters of each source, adding candidate sources where potential sources have a TS of greater than 10. The location of each source is determined by fixing the spectral parameters and maximizing the likelihood with respect to the position of each source. Sources whose position do not converge well (due to inaccurate modeling of the diffuse emission, for instance), are localized with a moments analysis, restricting the semimajor axis of the moment to be less than $0.25^\circ$. Because the HEALPix tiles overlap, there is correlation between sources across the entire sky, and the positional and spectral fits are iterated until an approximate whole-sky fit is accomplished.

The search described in Chapter 4 makes use of the 3FGL to identify potential PBH candidates, and to place limits on their presence. Similar techniques are used to generate more specialized catalogs as well, for instance a catalog of sources near the Galactic center (the 1FIG catalog)[123], or sources significant above 10 GeV (the 3FHL catalog)[124]. The model built of the Galactic center at high energy in Chapter 6 is composed of sources from the 3FHL catalog.

# Chapter 3

# Black Holes

This chapter provides background information on black holes, with the main goal of motivating the search for evaporating primordial black holes discussed in Chapter 4. A high-level introduction to Hawking radiation is presented in Section 3.2.1. Primordial black holes are discussed in Section 3.3, and their potential as DM candidates is considered over a wide range of masses.

## 3.1 History

As early as 1784 [125], Michell used Newtonian physics to posit the existence of dark objects (the classical precursors of modern black holes) whose escape velocity was higher than the speed of light. Although the light from these objects could not be seen, Michell predicted that by studying the orbits of nearby objects, the presence and mass of the dark objects could be inferred via Newton's second law. Newtonian gravitation has since been supplanted by GR, but Michell was prescient, and his strategy of observing nearby orbits is used today to measure the mass of supermassive black holes (SMBHs) [e.g. 126].

The modern story of black holes begins with Einstein's formulation of GR, which was completed in late 1915 [127] with the publication of the Einstein equation (Equation 3.1). Shortly after the publication of Equation 3.1, Schwarszchild discovered the unique vacuum solution of the Einstein equation for a nonrotating and uncharged point mass [128, translated from German], which today bears his name (the Schwarszchild metric, Equation 3.2 below). Although the concept of a black hole follows naturally from the Schwarszchild solution, black holes were initially met with skepticism from the scientific community, including by Einstein himself [129]. Nevertheless, the viability of black holes started to become more widely accepted after Chandrasekhar [130] showed that electron degeneracy could not prevent the collapse of objects heavier than $1.44\,M_\odot$ (where $M_\odot$ is the mass of the Sun). Whether or not black holes were realized in Nature, however, remained an experimental question.

Observational evidence for a black hole was first described in Webster and Murdin's analysis of the X-ray star Cygnus X-1 [131]. Spectroscopic data taken in 1971 showed periodic oscillation in the line-of-sight velocity, suggesting the star was in a binary system with a massive companion. The derived orbital radius was found to be smaller than the Roche limit for the star, implying that accretion onto the companion could be taking place (explaining the observed X-ray emission). The companion mass was initially found to be $2.5\ M_\odot < m < 6\ M_\odot$ (although later estimates placed the mass at around $16\ M_\odot$ [132]), and the observed variability of X-ray emission (as small as 1 ms) implied the companion was quite compact, leading to the the possibility that the companion was a potential black hole.

The star in Cygnus X-1 has a relatively high mass (estimated to be somewhere near $33\,M_\odot$), but there is signficant uncertainty in its exact value, and therefore uncertainty in the mass of its companion [132]. Later observations of other X-ray sources, in particular V404 Cygni, firmly established that the mass of compact objects in X-ray binary systems can have mass $> 10\,M_\odot$ [133]. Because neutron degeneracy can only support a mass of at most a few $M_\odot$ against gravitational collapse [134], the compact companions are almost certainly black holes.

The most convincing evidence for the existence of black holes comes from studies of stellar dynamics near the Galactic center. In 1996 Genzel et al. [135] used spectroscopic data of the stars closest to the dynamical center to infer their velocity dispersion, concluding that the data was consistent with either a cluster of $10 - 20\,M_\odot$ black holes, or a single heavier black hole. More detailed measurements were taken by Ghez et al. [136] in 1998 that confirmed the high density at the dynamical Galactic center, and implied the presence of a single SMBH coincident with the position of the radio source Sgr A*. Recent analysis [126] places the mass of the SMBH at Sgr A* at around $5.7 \times 10^6\,M_\odot$, although there is some uncertainty in the exact value. It is now believed that nearly every large galaxy has a supermassive black hole at its center, some of which are over $10^9\,M_\odot$ [114]. This abundance of SMBHs, especially those in an active environment, is responsible for the majority of $\gamma$-ray sources in the Fermi 3FGL catalog.

Although the indirect evidence for the presence of black holes is substantial, it is difficult to image a black hole directly due to their small angular size. In the near future, observations from an array of radio telescopes (the Event Horizon Telescope [137]) may be able to directly image the SMBH at Sgr A* with long-baseline interferometry to perform tests of GR in a region of strong gravity.

## 3.2 Theory

General relativity (GR) is a theory of gravitation, and relates the curvature of spacetime (encoded in the metric $g_{\mu\nu}$) to the presence of matter. In GR, free particles trace the path of geodesics, which are straight lines in familiar Minkowski space, but are curved for other metrics. A full review of GR is outside the scope of this dissertation; the interested reader is referred to Wald [86] for a comprehensive review.

The relation between curvature and matter is given by Einstein's equation, which in natural units (i.e. $c, h = 1$) reads:

$$R_{\mu\nu} - \frac{1}{2}Rg_{\mu\nu} = 8\pi G T_{\mu\nu} \tag{3.1}$$

where $R_{\mu\nu}$ is the Ricci tensor, $R \equiv g^{\mu\nu}R_{\mu\nu}$ is the Ricci scalar, and $T_{\mu\nu}$ is the energy-momentum tensor. The Ricci tensor is generated by contraction of the Riemann tensor $R_{\mu\nu} = R^{\lambda}{}_{\mu\lambda\nu}$, which in turn can be derived directly from the metric of the spacetime $g_{\mu\nu}$. Therefore the left-hand side of Equation 3.1 is related to the curvature of the spacetime, while the right-hand side depends only on the presence of energy-momentum.

Solving Equation 3.1 in general is difficult due to its nonlinearity: gravitational fields themselves carry energy density. In a few particular cases, however, Einstein's equation can be solved exactly. The quintessential example is the Schwarzschild metric, which is the unique static, spherically-symmetric solution to Equation 3.1:

$$ds^2 = -\left(1 - \frac{2M}{r}\right) dt^2 + \left(1 - \frac{2M}{r}\right)^{-1} dr^2 + r^2 d\Omega^2 \tag{3.2}$$

The Schwarszchild metric describes a nonrotating, uncharged point mass $M$ at the origin of the coordinate system in a vaccum, and is therefore of great interest in astrophysical contexts. As expected, the Schwarzschild metric reduces to familiar Minkowski space ($ds^2 = -dt^2 + dr^2 + r^2 d\Omega^2$) in the limiting cases of small mass ($M \to 0$) and at large distances away from the gravitating body ($r \to \infty$). Two singularities are apparent in the Schwarszchild metric, at $r = 0$ and $r = 2M$. It so happens that the singularity at the Schwarszchild radius $r = 2M$ is not a true singularity; instead it is caused by the choice of coordinates. However, scalars from the Riemann tensor can be constructed that diverge at $r = 0$, indicating the presence of a true singularity there:

$$R^{\mu\nu\rho\sigma} R_{\mu\nu\rho\sigma} = \frac{48G^2M^2}{r^6} \tag{3.3}$$

The $r = 0$ singularity should not be too surprising; after all, the Schwarzschild solution is only valid in vacuum, so to extend the solution down to $r = 0$, the density must diverge as well. For normal gravitating spherically symmetric bodies (e.g. stars, planets), the Schwarszchild metric (valid on the exterior) can be matched to an interior metric, whose curvature scalars are nonsingular. The $r = 0$ singularity would be no problem at all if not for the fact that for $r < 2GM$, the coefficient of $dr^2$ and $dt^2$ change signs, meaning the $r$ becomes timelike and the $t$ coordinate becomes spacelike. Therefore if a mass M is contained entirely within its Schwarzschild radius $R_S = 2GM$, its constituent particles will, in a finite time, move towards $r = 0$ in the same way that normal particles in Minkowski space move towards $t \to \infty$. The resulting object is a black hole, and the spherical surface at the radius $R_S$ is interpreted as the event horizon: a surface which the worldlines of particles can enter but never escape.

### 3.2.1 Hawking Radiation

In the classical treatment, black holes have no temperature and do not emit blackbody radiation; intuitively, energy cannot escape a black hole because particles inside the event horizon are trapped within Schwarschild radius $R_S$. In the 1970s, however, it was noted that black holes appear to exhibit many of the same properties as classical thermodynamic systems. Hawking's black hole area theorem [138] is one example: during black hole mergers, the total black hole surface area is nondecreasing in much the same way that the Second Law of thermodynamics states that the entropy of a closed system is nondecreasing. Further work led to the following identifications thermodynamic quantities and black hole properties:

$$\begin{aligned} \text{Entropy } S &\longleftrightarrow \text{Black hole surface area } A \\ \text{Temperature } T &\longleftrightarrow \text{Surface gravity } \tfrac{\kappa}{2\pi} \\ \text{Energy } U &\longleftrightarrow \text{Mass } M \\ dU = TdS + pdV &\longleftrightarrow dM = \tfrac{\kappa}{8\pi} dA + \Omega dJ \end{aligned}$$

By identifying the quantities in the last line (which is just the First Law of Thermodynamics), a Generalized Second Law was constructed by Bekenstein [139], which states that the *generalized entropy* $S + \frac{1}{4}A$ never decreases. Hawking realized that the Generalized Second Law implies that black hole area can decrease (in violation of the classical area theorem), at the expense of emitting particles which contribute to the classical entropy $S$ [140].

The vacuum of quantum field theory is observer-dependent, and observers in an accelerating reference frame see thermal radiation from a simple Minkowski vacuum (the Unruh effect [141, 142, 143]). Since any spacetime can be locally approximated as Minkowski space by a free-falling observer, static observers distant from a black hole will see the spacetime near the black hole as accelerating, and will associate thermal radiation with it. This is Hawking radiation, the spectrum of which is that of a gray body:

$$\langle n_\omega \rangle = \frac{\Gamma(\omega)}{e^{2\pi(\omega-\mu)/\kappa} \pm 1} \tag{3.4}$$

Here $\omega$ is the frequency of the radiation, $\mu$ is the chemical potential (characterizing the tendency of the black hole to preferentially emit particles that reduce its net charge and angular momentum), and $\Gamma(\omega)$ is a graybody factor that accounts for backscattering of particles whose wavelength is greater than the Schwarzschild radius. Heuristically, Hawking radiation can be imagined as the consequence of virtual pairs of particles which lie on either side of the event horizon. The virtual particle on the interior is trapped, but the exterior particle is not and escapes to infinity, where it is interpreted as Hawking radiation. The Hawking temperature of a black hole is given by:

$$T = \frac{\hbar c^3}{8\pi k_B G M} \tag{3.5}$$

As the black hole emits Hawking radiation, it loses mass and becomes hotter, opening up new degrees of freedom for the black hole to evaporate through. The mass loss is approximated by [134]:

$$\frac{dM}{dt} = \frac{-\alpha(M)}{M^2} \tag{3.6}$$

where $\alpha(M)$ parameterizes the number of degrees of freedom available to the black hole, and is approximately $10^{26}\,\mathrm{g^3 s^{-1}}$ for a $T < 100$ MeV black hole. Since an evaporating black hole spends most of its life at low temperatures, the lifetime of a small black hole can be approximated:

$$\Delta t = \frac{M}{dM/dT} = \frac{M^3}{\alpha(M)} \approx \frac{M^3}{10^{26}\,\mathrm{g^3 s^{-1}}} \approx 10^{19}\left(\frac{M}{10^{15}\,\mathrm{g}}\right)^3 \mathrm{s} \tag{3.7}$$

With the current age of the Universe of $4.3 \times 10^{17}$ s, black holes formed in the early Universe with initial mass of $\sim 5 \times 10^{14}$ g (for reference, about 100 times the mass of the Great Pyramid at Giza), would be evaporating now.

In the standard picture, $\alpha(M)$ increases with the temperature of the black hole by about an order of magnitude as $T \to \infty$, which causes evaporation to increase at a rate that smoothly increases. This process continues until the entirety (or at least nearly so [144]) of the black hole has evaporated. The highly nonlinear nature of the evaporation means that around $10^{30}$ ergs of energy (several times the energy contained in all the Earth's fossil fuel reserves [145]) are released in the final second of the black hole's life, and the potential for these explosions to be observed was quickly recognized by Hawking [146] and Page [147]. Some alternative models (e.g. the Hagedorn model [148]) predict an exponential increase in the number of degrees of freedom at a few hundred MeV, which implies an even more energetic explosion takes place, although these models are disfavored.

## 3.3 Primordial Black Holes

Black holes formed via stellar collapse have a minimum mass of approximately $3M_{\odot}$, as neutron stars smaller than this are capable of being supported by neutron degeneracy pressure [134]. The early Universe, on the other hand, was extraordinarily dense, and large fluctuations in the density could have produced overdense regions that collapse into black holes. A number of more exotic formation mechanisms for these *primordial black holes* (PBHs) have also been proposed in the literature, including the collapse of loops of cosmic strings [81, 149], phase transitions [150], and inflationary relics [151]. If PBHs form via the collapse of overdense regions, the PBH mass is characterized by the horizon mass at the time of its formation:

$$M = \rho \frac{4\pi}{3} t^3 = \frac{3H^2}{8\pi G} \frac{4\pi}{3} t^3 \tag{3.8}$$

where Equation 1.7 has been substituted to find $\rho$. In the radiation-dominated Universe, the Hubble parameter is just $H = \frac{1}{2t}$, so the mass is simply (restoring appropriate factors of $c$):

$$M = \frac{c^3}{4G} t = 10^{38} \text{ g s}^{-1} \tag{3.9}$$

PBHs formed at very early times (near the Planck era, $10^{-43}$ s) have masses near the Planck mass of $\sim 10^{-5}$ g, while PBHs formed at late times ($t \sim 1$s) will be supermassive.

Some authors have proposed that the supermassive black holes found in nearly all galaxies are themselves primordial [152].

### 3.3.1 PBHs as DM candidates

Although stellar-collapse black holes are both dark and cold, they cannot themselves be the DM, as DM is known (from BBN and CMB considerations) to have dominated the mass of the Universe long before the first stars were formed [25, 26]. However, primordial black holes that form prior to BBN would behave like particle DM, and it is natural to consider them as DM candidates. The range of possible PBH masses is bounded on the lower end at $5 \times 10^{14}$g, as PBHs below this mass would have completely evaporated by now. At the upper end, PBHs must be less massive than about $10^{38}$ g or $10^{8}$ $M_{\odot}$ so as not to disrupt BBN. A variety of techniques have been employed to constrain the density of PBHs in the intervening mass range:

- *$\gamma$-ray observations*: Very low mass black holes (close to the evaporation mass $5\times10^{14}$g) emit $\gamma$ rays over their life via Hawking radiation, which would contribute to the isotropic $\gamma$-ray background mentioned in Section 2.3.1. Analysis of the *Fermi*-LAT isotropic diffuse spectrum was used to place limits on the cosmological density of low-mass PBHs in 2010 [153] by requiring the integrated emission from PBHs to be below the observed flux.

  Because PBHs, like DM, would cluster in galactic halos, they could potentially exist in the neighborhood of the Earth. It is interesting to consider the typical distance scale from Earth to the nearest PBH:

$$d = \left(\frac{\rho_{DM}}{M_{PBH}}\right)^{-1/3} = 1.2 \times 10^{11}\ \mathrm{m} \approx 0.8\ \mathrm{a.u.} \tag{3.10}$$

with $\rho_{DM} = 0.3$ GeV/cm$^3$[154] and $M_{PBH} = 10^{15}$g. This distance is small enough that the $\gamma$-ray emission from the late stages of evaporation by individual PBHs could potentially be observed directly, instead of observing the integrated $\gamma$-ray emission from a large population of PBHs. As shown in Chapter 4, *Fermi*-LAT is sensitive to an evaporating PBH out to a distance of approximately 0.05 pc $\approx 10^4$ a.u. The non-observation of individual PBHs in the neighborhood of Earth then strongly constrains the PBH contribution to DM, depending on the degree of DM clustering assumed.

In Section 3.2.1, it was noted that the rate of Hawking evaporation is dependent on the number of degrees of freedom available to the BH. This means that light curve of an evaporating PBH is sensitive to *all* particles, even those that are uncharged under any SM interactions. If the DM is composed of electroweak-scale WIMPs, for instance, the observation of an evaporating PBH would provide information about the DM mass, no matter how small the WIMP-SM coupling may be. Therefore a search for individual PBH evaporations is well-motivated, both to constrain PBHs as DM themselves, and to look for clues about particle DM. Chapter 4 describes such a search in detail.

- *Gravitational lensing*: As discussed in Section 1.1, the presence of a massive body will cause light from distant sources to be lensed. For the case of a black hole passing between an observer and a distant light source, the observer will see an increase in the apparent surface brightness of the object. A search conducted with the Subaru Hyper Suprime Cam telescope for microlensing ($t \sim 10$ minutes) of stars in the Andromeda galaxy found only a single lensing candidate event, which strongly constrains the number density of black holes in the mass range $10^{-11} M_{\odot} < M_{PBH} < 10^{-6} M_{\odot}$ [155].

PBHs with smaller masses, $10^{-20}\mathrm{g} < \mathrm{M_{PBH}} < 10^{-17}\mathrm{g}$, have a Schwarszchild radius comparable to or smaller than the wavelength of even $\gamma$ rays, and therefore have a more complicated lensing signature. Instead of an increase in brightness of the lensed object, the PBH introduces an energy-dependent phase shift in the $\gamma$ rays, which leads to interference fringes in the observed spectrum. A search using *Fermi*-GBM data for this spectral modulation (known as femtolensing) in 20 $\gamma$-ray bursts found no candidate events, which sets an upper limit on the PBH density of about 5% of the critical density for PBHs in this mass range [156].

- *Accretion*: PBHs incident on a neutron star can deposit significant energy via tidal forces into acoustic modes of the neutron star, potentially losing enough energy to become gravitationally bound to the neutron star. When the PBH settles in the core, significant tidal disruption takes place and the host is rapidly accreted. Detailed calculations of this process were performed by Pani and Loeb [84], who find the time scale for accretion is shorter than a typical neutron star age of $10^{10}$ years for PBHs heavier than about $10^{16}$ g. The existence of old neutron stars in

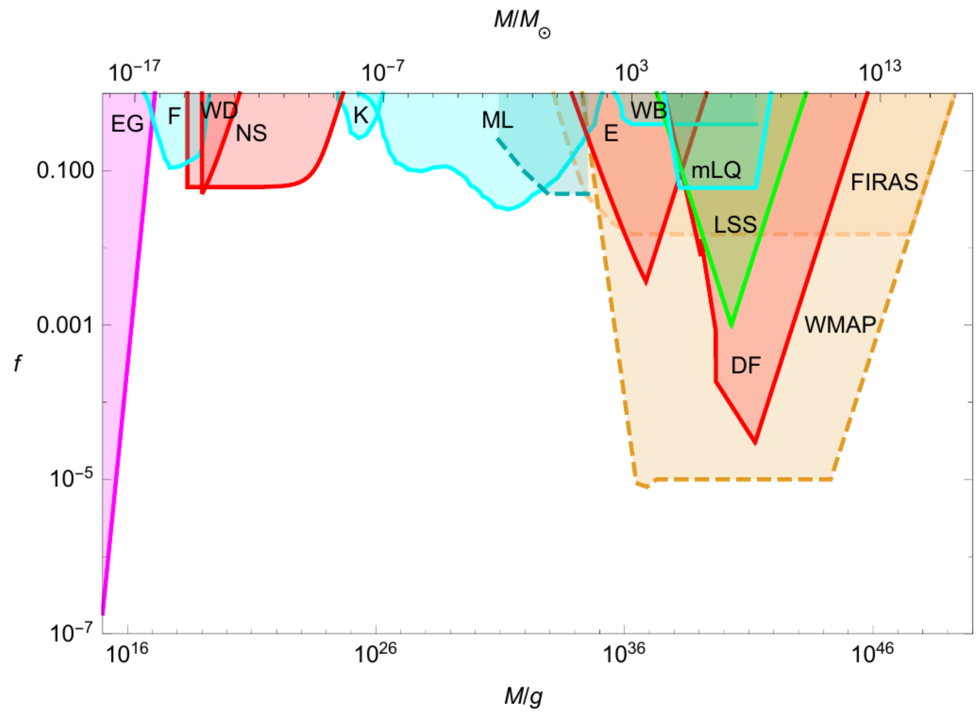


Figure 3.1: Constraints on PBHs as DM, as of 2016. The curves present limits on the fraction $f$ of the DM density that PBHs can contribute to. Limits discussed in the text include Hawking evaporation (EG), femtolensing of GRBs (F), accretion onto neutron stars (NS), microlensing (ML), and disruption of wide binaries (WB). Figure reproduced from (and references available in) [85].

DM-rich areas therefore places strong constraints on the prevalence of PBHs in the mass range $10^{17}\,\mathrm{g} < \mathrm{M_{PBH}} < 10^{24}\,\mathrm{g}$.

An interesting scenario occurs if a PBH is incident on a millisecond pulsar (MSP), whose high angular momentum prevents it from being totally accreted. In this case, a significant fraction of the MSP mass $(0.5-1\mathrm{M}_\odot)$ can be ejected, potentially forming a large fraction of the heavy elements in the Universe [157].

- *Dynamical constraints*: PBHs more massive than $M_\odot$ can exchange significant momentum during gravitational scattering, and can disrupt weakly bound dynamical systems. The observation of wide ($> 100$ AU) binary star systems was used to place limits on heavy PBHs above about $40M_\odot$ [158], although it was argued that the result relied heavily on only a few, potentially spurious, binary systems [159].

A more recent approach utilized the fact that the exchange of energy via gravitational scattering in a many-body system leads to mass segregation, i.e. the heaviest objects become clustered while lighter ones are diffused [160]. The observed density of a star cluster at the center of the ultrafaint dwarf galaxy Eridanus II therefore can strongly constrain black holes more massive than the stars; depending on the assumption of average DM density, velocity dispersion, and age of the dwarf galaxy, PBHs above $5M_\odot$ can be excluded from being the DM [161].

Although signficantly constrained, there remain small windows of mass in which PBHs could still contribute substantially to the DM density. The most intriguing of these windows is the 20-50 $M_\odot$ regime (the so-called "intermediate" mass range), as nearly all of the 22 black holes observed in black hole-black hole mergers during the first and second observing runs of LIGO fall within this range [162]. Some authors have proposed that the measured merger rate, although rather uncertain, is consistent with intermediate mass PBHs being the DM [83]. More data from LIGO and its successors should conclusively rule this scenario in our out as more data is gathered.

Most constraints cited here assume a monochromatic PBH mass function, though some authors have argued that an extended mass function is natural to consider. In any case, monochromatic constraints can be translated into constraints on extended mass functions [85] without great difficulty.

# Chapter 4

# Search for Gamma-Ray Emission from Local Primordial Black Holes with the *Fermi* Large Area Telescope

This chapter (aside from this title page) is a reproduction of a previously published article [1].

Some minor changes to the formatting have been made in order to match the style of the rest of this document, however, no changes to the content have been made. The references in this chapter are displayed in the main Bibliography below, for convenience. The coauthors of this paper have given permission for this material to be reprinted here; their letters of permission are attached.

## Abstract

Black holes with masses below approximately $10^{15}$ g are expected to emit gamma rays with energies above a few tens of MeV, which can be detected by the *Fermi* Large Area Telescope (LAT). Although black holes with these masses cannot be formed as a result of stellar evolution, they may have formed in the early Universe and are therefore called Primordial Black Holes (PBHs). Previous searches for PBHs have focused on either short timescale bursts or the contribution of PBHs to the isotropic gamma-ray emission. We show that, in case of individual PBHs, the *Fermi* LAT is most sensitive to PBHs with temperatures above approximately 16 GeV and masses $6 \times 10^{11}$ g, which it can detect out to a distance of about 0.03 pc. These PBHs have a remaining lifetime of months to years at the start of the *Fermi* mission. They would appear as potentially moving point sources with gamma-ray emission that becomes spectrally harder and brighter with time until the PBH completely evaporates. In this paper, we develop a new algorithm to detect the proper motion of a gamma-ray point sources, and apply it to 318 unassociated point sources at high galactic latitude in the third *Fermi*-LAT source catalog (3FGL). None of unassociated point sources with spectra consistent with PBH evaporation show significant proper motion. Using the non-detection of PBH candidates, we derive a 99% confidence limit on PBH evaporation rate in the vicinity of the Earth $\dot{\rho}_{\mathrm{PBH}} < 7.2 \times 10^3\ \mathrm{pc}^{-3}\mathrm{yr}^{-1}$. This limit is similar to the limits obtained with ground-based gamma-ray observatories.

## 4.1 Introduction

The formation of primordial black holes (PBHs) is a prediction of some models of the early Universe [138, 163]. In this paper, we search for evidence of gamma rays produced by the Hawking radiation of low-mass, high-temperature PBHs in the *Fermi* Large Area Telescope (LAT) data.

In classical general relativity, black holes have zero temperature and do not emit particles. The concept of a black hole temperature was formally introduced as a way to resolve the paradox of information loss for matter falling into the black hole [139, 164]. [140, 146] argued that black holes should emit particles due to pair creation near the horizon with grey body emission spectra with the temperature

$$T_{\rm BH} = \frac{\hbar c^3}{8\pi G M k} \approx 10^{-7} \left(\frac{M}{M_\odot}\right)^{-1} K, \tag{4.1}$$

where $M$ is the black hole mass and $M_\odot$ is the Solar mass. Astrophysical black holes, such as those created in a collapse of a massive star, have masses larger than $M_\odot$. The corresponding temperature is less than $10^{-7}$ K, which is less than the fluctuations in the cosmic microwave background (CMB) radiation; this makes the signal from these BHs extremely difficult to detect. However, PBHs with masses as small as the Planck mass ($\sim 10^{-5}$ g) may have been created in the early Universe [138, 163].

The mass of a PBH created at time $t$ after the Big Bang is proportional to the mass within the particle horizon at time $t$ [for a review see 134, 165, 166],

$$M(t) \approx 10^{15} \left(\frac{t}{10^{-23}{\rm s}}\right) {\rm g}. \tag{4.2}$$

Limits on density of PBHs at mass $M$ constrain the magnitude of density fluctuations (or the equation of state) at time $t$. These constraints are complementary to the constraints obtained from observations of the CMB since they are sensitive to fluctuations on spatial scales much smaller than the scales observed in the CMB [e.g., 167].

Since Hawking radiation is emitted in all available particle species, the total emitted power and therefore the lifetime of a PBH depends on the number of available particle states. For the Standard Model of particles, the lifetime of a PBH can be approximated as [153]

$$\tau \approx 400 \left(\frac{M}{10^{10}\mathrm{g}}\right)^3 \mathrm{s}. \tag{4.3}$$

The PBHs which were formed in the early Universe with a mass around $M_* = 5 \times 10^{14}$ g have a lifetime close to the lifetime of the Universe and reach late stages of evaporation at the present time. The PBHs with the remaining lifetime of months to years will be the subject of the search in this paper. The temperature corresponding to $M_*$ is $T_{\mathrm{BH}} \approx 20$ MeV [153, 168].[1] A limit on the average cosmological density of PBHs can be obtained by integrating the flux from PBHs over the lifetime of the Universe. This flux has to be smaller than the observed extragalactic gamma-ray background [153, 169]. This method is most sensitive to PBHs with initial masses $M \approx M_*$. Since PBHs are expected to be concentrated in galaxies similarly to dark matter, stronger constraints for initial masses slightly larger than $M_*$ can be obtained by searching for diffuse emission from PBHs in the halo of the Milky way galaxy [170]. A comparison of extragalactic and Galactic gamma-ray background constraints with the constraints from the search

[1] Here and in the following we convert temperature to energy units by multiplying with the Boltzmann constant $k$.

for individual PBHs will be presented in Section 4.5.

Constraints on the local PBH evaporation rate have been obtained by looking for bursts of high-energy gamma-ray emission with duration of a fraction of a second to several seconds. In particular, PBHs with a mass of $M \sim 10^9$ g have temperature $T_{\rm BH} \approx (10^{10}\,{\rm g}/M_{\rm BH})\,{\rm TeV} \sim 10\,{\rm TeV}$ [153] and lifetime $\tau \sim 0.4$ sec. A search for such PBHs in the context of the Standard Model has been carried out by searching for high-energy gamma rays ($\approx 100$ GeV $<$ E $<\approx 50$ TeV) with Cherenkov telescopes [e.g., 171, 172, 173]. In the case of the Hagedorn model [148], which was proposed before the Standard Model of particle physics was confirmed, the number of states available for the PBH evaporation increases exponentially when the temperature reaches the Hagedorn transition energy around 160 MeV. This leads to a microsecond burst of gamma rays around a few hundred MeV [147]. A search for such bursts was carried out using EGRET data [174]. One can also expect short radio bursts in this model [175], which can be used to constrain the PBH evaporation rate [e.g., 176, 177].

*Fermi* LAT is a pair conversion telescope which is sensitive to gamma rays from $\approx 20$ MeV to more than 300 GeV. Overviews of the *Fermi*-LAT design and performance can be found in [88] and [99]. PBHs with masses $M \lesssim 10^{15}$ g have temperatures $T \gtrsim 10$ MeV and emit gamma rays [147] that can be detected with the *Fermi* LAT.

In this paper, we search for PBHs in the context of the Standard Model of particles using the *Fermi*-LAT gamma-ray data. In Section 4.2 we estimate that for the differential point source (PS) sensitivity in 4 years of observation the *Fermi* LAT is most sensitive to PBHs with temperature $T_{\rm BH} \sim 16$ GeV(corresponding to a remaining lifetime of $\sim$4 years). The corresponding distance to which such a PBH can be detected is $\lesssim 0.02$ pc. Assuming a random relative velocity of PBHs around the Earth similar to that of particle dark matter velocity dispersion, the displacement of a PBH over 4 years within 0.02 pc is, on average, greater than $1^\circ$. For comparison, the point source (PS) localization radius for a near-threshold source is approximately $0.1^\circ$ [99]. Thus a smoking-gun signature of a PBH in *Fermi*-LAT data is a moving source with a hard spectrum of gamma rays. A search for such sources is a novel feature of our analysis that has not been discussed in the literature related to PBH searches.

In Section 4.3 we search for PBH candidates among the sources of the third *Fermi*-LAT catalog [3FGL, 120]. The majority of sources can be excluded as PBH candidates based on association with known sources or on their spectra, but several sources cannot be excluded based on these criteria alone. For these sources, we analyze the *Fermi*-LAT data near the position of the PBH candidates and find one candidate whose proper motion is inconsistent with zero. We discuss this source in more detail in Section 4.3.2. In Section 4.4 we use Monte Carlo simulations to derive the efficiency of our PBH selection criteria, which we then use to derive an upper limit on the PBH evaporation rate. We find that PBHs can be detected up to a distance of $\sim 0.03$ pc at the expense of a reduction of volume in phase space: the PBHs should be moving preferentially along the line of sight to be detected as a PS. The detectability distance of $\approx$0.03 pc derived with MC simulations and the full PS analysis pipeline is generally consistent with the simple estimate of 0.02 pc, which we obtain for non-moving PBHs using the known differential sensitivity of *Fermi* LAT to point sources. In Section 4.5 we present the conclusions. In Appendix 4.A we discuss some uncertainties on the spectrum of gamma rays emitted by PBHs.

## 4.2 Sensitivity of *Fermi* LAT to Individual Primordial Black Holes

We start our analysis by estimating the sensitivity domain, i.e., the relevant energies and timescales, of the *Fermi* LAT to individual PBHs. One of the main questions is whether the *Fermi* LAT is more sensitive to a population of PBHs with "low" temperature (e.g., $\lesssim$ 10 GeV), hence, smaller intensity of emission but large spatial density, or to a population with "high" temperature (e.g., $\gtrsim$ 10 GeV) but low spatial density.

In this section, we derive the range of masses, temperatures, and distance to the Earth where PBHs are detectable by *Fermi* LAT. In Figure 4.1, we compare the spectra of PBHs with the differential PS sensitivity for 4 years of Pass 7 reprocessed data [99, 105]. The same data sample was used in the derivation of the 3FGL catalog [120], which we use in the next section to search for PBH candidates. To determine the four-year equivalent flux from a PBH, we integrate the PBH spectrum either over the lifetime of the PBH or over four years, whichever is smaller, and divide by four years. The PBH spectra are derived taking into account both primary and secondary (mostly from hadronic showers of quarks and gluons) production of gamma rays by the black holes [178]. Although all Standard Model particles can be emitted by PBHs in principle, the $\gamma$-ray spectrum is dominated by the Quantum chromodynamics (QCD) degrees of freedom [179]. The normalization for each of the curves is chosen such that the PBH flux is equal to the differential PS sensitivity in one of the energy bins.

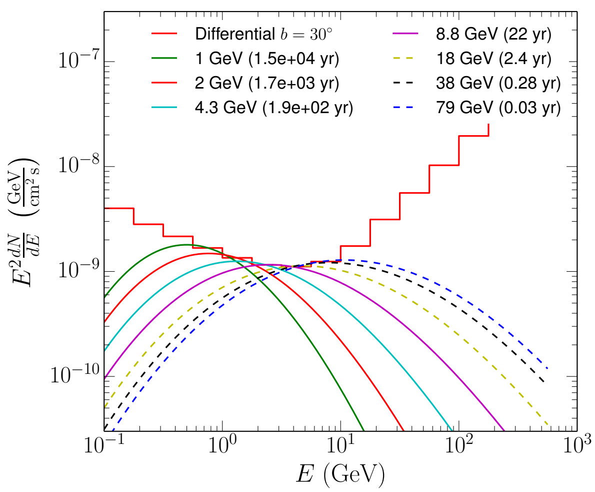


Figure 4.1: Comparison of spectra of PBHs with different initial temperatures and *Fermi*-LAT PS differential sensitivity at $b = 30°$, which is representative for *Fermi*-LAT PS sensitivity away from the Galactic plane. Lines correspond to PBHs with different initial temperatures specified in the labels, with the corresponding lifetimes shown in parentheses. PBHs with lifetimes longer than 4 years are shown as solid lines, while PBHs with lifetime shorter than 4 years are shown as dashed lines. The distance to each PBH is chosen such that the flux from the PBH is equal to the PS sensitivity in one of the energy bins (the corresponding detectability distances are shown as a solid line in Figure 4.2 on the right).

Since the intrinsic luminosity of PBHs for a given temperature is fixed, we can use the condition that the flux should be larger than the PS sensitivity to estimate the maximal distance at which the PBHs can be detected as a function of initial temperature (shown by the solid line in Figure 4.2 right). Typical values near the maximum are $\lesssim 0.02$ pc for initial temperatures between 10 GeV and 40 GeV. The corresponding remaining lifetime is between  20 years and  4 months. Over the age of the Universe, we expect PBHs to virialize in the same manner as dark matter. If we take into account the orbital velocity of the solar system around the GC $v_{\rm rot} \sim 250$ km s$^{-1}$ [180, 181, 182, 183, 184, 185] and add a velocity dispersion similar to the expected dark matter velocity dispersion near the Sun $v_{\rm disp} \sim 270$ km s$^{-1}$ [e.g., 186] then the displacement of a PBH during 3 years at $R = 0.02$ pc from the Earth could be as large as $\alpha = v_{\rm perp} t/R \propto 3^\circ$. Here we estimated the average velocity perpendicular to the line of sight in a random direction on the sky as $v_{\rm perp} = \sqrt{2/3(v_{\rm rot}^2 + v_{\rm disp}^2)} \sim 300$ km s$^{-1}$. Because this displacement is $\sim$ 15 times larger than the *Fermi*-LAT PS localization radius for a threshold source, such a black hole will appear as a linear streak of gamma-ray emission instead of a point source.

Since the large majority of *Fermi*-LAT sources are point-like, linear spatial extension is a powerful criterium for identifying PBHs. One of the difficulties in observing a moving PS is that the flux becomes smeared out into an extended track following the trajectory of the source, but PS catalogs are optimized for sensitivity to point sources as opposed to extended sources. A simple estimate of the *Fermi*-LAT sensitivity to a moving source can be obtained by integrating the flux during the time when the moving source appears as a point-like source, e.g., when the displacement is less than the PS localization radius. The corresponding time is shown by in Figure 4.2, left.[2] Using the

[2]The time for a PBH with an average velocity to appear as a point-like source is smaller than 4 years, which is the observation time for the 3FGL catalog. Better sensitivity to PBHs can be obtained by searching for PS with duration in the range from approximately a month to a year due to lower background for shorter integration time. Such a search of PS with a sliding time window goes beyond the scope of this work, where we restrict the analysis to PS detected in the 3FGL catalog.

reduced integration time, we also derive the corresponding detectability distance (red dash-dotted line in Figure 4.2 on the right). For large temperature (small remaining lifetime) the detectability distance for a moving source is the same as for a stationary one because the expected displacement is smaller than the PS localization radius.

Given the characteristic detection radius for PBHs including the proper motion $R \sim 0.01$ pc for 4 years of observations (Figure 4.2, right panel), we estimate that the *Fermi* LAT is sensitive to a PBH evaporation rate of $\dot{\rho} = 1/Vt \propto 6 \times 10^4\,\mathrm{pc}^{-3}\mathrm{yr}^{-1}$, where $V = 4\pi R^3/3$ is the detectability volume and $t = 4$ yr is the observations time. The main result of this section is that the *Fermi*-LAT sensitivity is potentially competitive with sensitivity to individual PBHs of Cherenkov observatories [171, 172, 173, 187], e.g., $\dot{\rho} = 1.4 \times 10^4\,\mathrm{pc}^{-3}\mathrm{yr}^{-1}$ derived by the H.E.S.S. collaboration [172], but one has to take the proper motion of PBHs into account. In the following sections we use the 3FGL catalog, which employs the full PS sensitivity of the *Fermi* LAT rather than the differential sensitivity. We also treat the proper motion more rigorously. As a result, the derived *Fermi*-LAT sensitivity is a factor of a few better than the simple estimate presented in this section.

## 4.3 A Search for PBH Candidates in *Fermi*-LAT 3FGL Catalog

The *Fermi*-LAT surveys the entire sky approximately every three hours, and has relatively uniform exposure over long time scales (at 1 GeV over 4 years the exposure

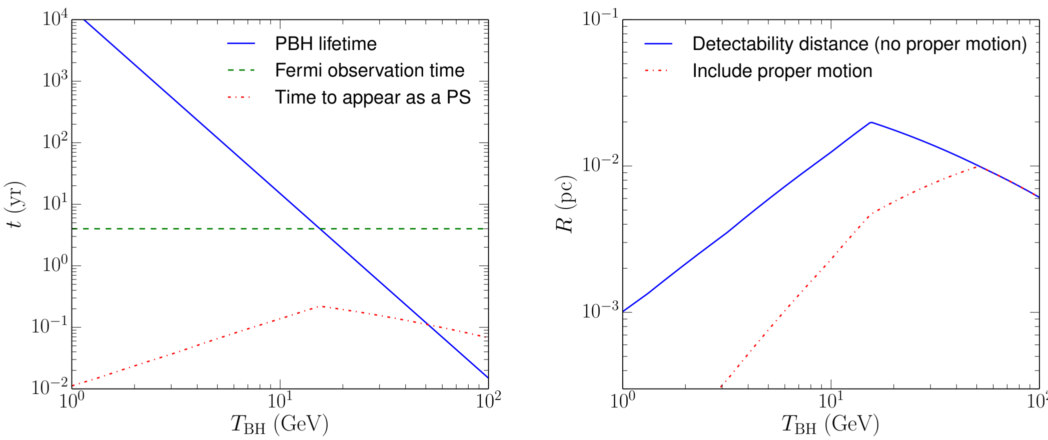


Figure 4.2: Left: solid line - PBH lifetime as a function of initial temperature, dashed line - 4 years, dash-dotted line - time during which the displacement is less than $0.2°$ which is approximately equal to twice the PS localization radius at 10 GeV for Pass 7 reprocessed data assuming relative velocity perpendicular to the line of sight $\sim 300\ \mathrm{km\,s^{-1}}$ and distance represented by the solid line on the right plot. Right: solid line - detectability distance for a PBH as a function of initial temperature $T$ from the *Fermi*-LAT PS differential sensitivity (Figure 4.1); dash-dotted line - detectability distance taking into account relative motion of PBHs due to orbital motion in the Galaxy and dark matter-like velocity dispersion (dash dotted line on the left plot). PBHs with lifetimes of 4 years have a temperature of about 16 GeV; the break at 16 GeV results from lower-temperature PBHs having longer lifetimes than the observation time, i.e., they evaporate only partially, while PBHs with temperatures higher than 16 GeV have a smaller initial mass, i.e., produce smaller total fluxes than PBHs with initial temperature of 16 GeV.

varies by approximately 40% over the entire sky). Combined with a large effective area (approximately 1 $m^2$ between 1 GeV and 1 TeV), this makes it an ideal instrument for detecting a large number of gamma-ray point sources. The most complete catalog of point sources is currently the third *Fermi* point source catalog [3FGL, 120]. It contains sources that are significantly detected above 100 MeV and spans the first 4 years of the *Fermi* mission. We used the 3FGL catalog to search for PBH candidates and to constrain the local PBH evaporation rate.

To find PBH candidates in the 3FGL catalog, we first excluded from further consideration point sources associated with known astrophysical sources (such as blazars). Of 3033 sources in the 3FGL catalog, 1010 are unassociated sources. We also excluded sources that are within $10^\circ$ of the Galactic plane, which removed a further 468 sources. Our analysis was restricted to high-latitude sources because (a) detectable PBHs are expected be distributed isotropically given the detectability distances estimated in Section 4.2 while astrophysical sources are concentrated along the Galactic plane, and (b) association of extragalactic sources such as blazars is easier at high latitude [see, e.g. 188].

To test the remaining unassociated 3FGL sources as PBH candidates, we fit their spectra with the time-integrated gamma-ray spectra emitted by a PBH. For this analysis we used the fluxes of the candidate sources as reported in the 3FGL, which are provided in 5 energy bands ($0.1-0.3$, $0.3-1$, $1-3$, $3-10$, and $10-100$ GeV). The time-integrated PBH spectrum depends on two parameters: initial mass (or temperature) and the distance to the Earth (equivalent to an overall normalization). We varied these two parameters to obtain the best fit to the PS spectrum in the five energy bands. The quality of the spectral fit to the reported spectrum was determined by calculating the value of the $\chi^2$ over the five energy bands:

$$\chi^2 = \sum_{i=1}^{5} \frac{(\Phi_i - \Psi_i)^2}{\sigma_i^2}, \tag{4.4}$$

where $\Phi_i$ is the PBH spectrum integrated over the width of bin $i$ and $\Psi_i$ is the flux in bin $i$ from the 3FGL. Here $\sigma_i$ represents the uncertainty on the flux in bin $i$. In the 3FGL, flux uncertainty is represented by a 68% confidence interval; the value of the uncertainty can then be written as the difference between the best-fit flux and either the upper or lower bound. We set $\sigma_i$ to be the larger of the two in order to be conservative. We require the value of the best-fit $\chi^2$ to be below the critical value of 11.3, which corresponds to 99% exclusion for 5 degrees of freedom and 2 parameters. In other words, sources with a $\chi^2$ value greater than 11.3 have only a 1% chance of being spectrally consistent with a PBH. After the spectral consistency was computed, 318 sources out of the 542 unassociated candidates remained as PBH candidates.

The candidate sources next underwent a check for proper motion. We use the following algorithm to determine the magnitude and significance of proper motion:

1. All source-class photons above 1 GeV within 5° of the source's reported 3FGL location were collected. The time range (August 2008 to July 2012) and data reconstruction (`P7REP_SOURCE_V15`) were consistent with that of the data used to construct the 3FGL. Since the angular resolution of the *Fermi* LAT decreases quickly below 1 GeV, including photons below 1 GeV did not have a significant

impact on the final results.

2. Data covering a longer time range (August 2008 to July 2017) and a more recent event reconstruction (`P8R2_SOURCE_V6`) were held in reserve for validation, and was used to test the PBH hypothesis for any sources that passed the proper motion cut.

3. The expected number of photons $N$ from the source of interest was calculated by multiplying the flux in each energy bin by the *Fermi*-LAT exposure at the bin's midpoint energy, and summing over the three relevant bins (1 – 3 GeV, 3 – 10 GeV, 10 – 100 GeV).

4. In order to estimate the velocity of a PS we compare the maxima of the likelihood function $\mathcal{L}(\vec{x_i}, t_i, \vec{x_0}, \vec{v_0})$ in two cases: fixed $\vec{v_0} = 0$ and free $\vec{v_0}$. We approximate the point spread function of *Fermi* LAT by a Gaussian for simplicity. The likelihood function is given by multiplying over $N$ photons around the initial position of the source:

$$\mathcal{L} = \prod_{i=1}^{N} w_i \times \exp\{\frac{-(\vec{x_i} - \vec{x_0} - \vec{v_0} t_i)^2}{\sigma_i^2}\} \tag{4.5}$$

where $\vec{x_i}$ is the coordinates of the photon, $\vec{v_0}$ is the proper motion of the source, $t_i$ is the photon arrival time, $\vec{x_0}$ is the source location at the beginning of the observation time, and $\sigma_i$ is the 68% angular containment radius for a photon at energy $E_i$, which is $\sim 0\overset{\circ}{.}7$ at 1 GeV [105]. Here $w_i$ is a weight assigned to each photon, the calculation of which is defined in Section 4.3.1.

In practice, we use the natural logarithm of the likelihood:

$$\log \mathcal{L} = \sum_{i=1}^{N} \log w_i - \frac{(\vec{x_i} - \vec{x_0} - \vec{v_0} t_i)^2}{\sigma_i^2} \tag{4.6}$$

The main difficulty is separating the $N$ photons attributed to the source from background photons. Our algorithm chooses a 4-dimensional grid of points around an initial value of $\vec{x_0}$ and $\vec{v_0} = 0$, and for each grid point finds the $N$ photons inside the 5° ROI that have the highest contribution to $\log \mathcal{L}$, i.e. the photons which most likely belong to the source given a particular position and velocity. Therefore the weights $w_i$ do not appear as a prefactor in Eqs 4.5 and 4.6 because the $N$ best-fit photons change given different assumptions of $\vec{x_0}$ and $\vec{v_0}$. The best-fit $\vec{x_0}$ and $\vec{v_0}$ are found by maximizing $\Delta \log \mathcal{L} = \log \mathcal{L} - \log \mathcal{L}(\vec{v_0} = 0)$ on the grid. With the additional degrees of freedom from allowing $\vec{v_0}$ to float, the value of $\Delta \log \mathcal{L}$ is always nonnegative.

We find in MC simulations (described in Section 4.4) that this algorithm tends to underestimate the input velocity by $\approx 25\%$; the best-fit velocity should therefore be considered a lower bound on the true velocity and sufficient for our purpose of separation of moving and stationary sources. The underestimation occurs because source photons that are far away from the average source position have lower weights and so are less often included in the likelihood calculation. In their stead are background photons, whose distribution in time is random, and therefore cause the algorithm to favor a slower overall velocity.

5. The significance of $\Delta \log \mathcal{L}$ for each source was found by assigning random times

$t_i$ drawn from a flat distribution to each photon but fixing the positions $\vec{x_i}$ of all the photons, and reoptimizing $\Delta \log \mathcal{L}$. This process was repeated 50 times for each source, and the original value of $\Delta \log \mathcal{L}$ was compared with the distribution of $\Delta \log \mathcal{L}$ for the data sets scrambled in time to find a local significance $\sigma$:

$$\sigma = \frac{\Delta \log \mathcal{L}_0 - \overline{\Delta \log \mathcal{L}_s}}{\mathrm{std}(\Delta \log \mathcal{L}_s)}, \tag{4.7}$$

where $\Delta \log \mathcal{L}_0$ is the original value of the improvement in likelihood, $\overline{\Delta \log \mathcal{L}_s}$ is the mean of the scrambled likelihood improvements, and $\mathrm{std}(\Delta \log \mathcal{L}_s)$ is the standard deviation of the scrambled likelihood improvements.

6. A cut on the local significance for each source was made at $3.6\sigma$ which corresponds to a global significance of $2\sigma$ for 318 sources.

A single source (3FGL J2310.1−0557, see Section 4.3.2 for a discussion of this source) exceeded this cut on local significance, and the standard deviation of the local significances of the entire set of candidates was 1.03, which is consistent with statistical fluctuations. After examining the data held in reserve for J2310.1−0557 (described in Section 4.3.2), we concluded that no likely PBH candidates exist in the 3FGL catalog.

### 4.3.1 Calculating Photon Weights

The photon weights $w_i$ in equations 4.5 and 4.6 are defined as the probability that a given photon originated from the candidate PS, and are calculated by performing a standard likelihood optimization with the *Fermi* Science Tool `gtlike`[3]. The model

[3]Science Tools version v10r0p5, available at `http://fermi.gsfc.nasa.gov/ssc/data/analysis/software`

used includes all 3FGL PS within 5° of the candidate source, as well as the standard Pass 7 models for Galactic and isotropic diffuse emission. The candidate source is modeled as an extended source with a radial Gaussian profile with $\sigma = 0.25°$ instead of a PS, in order to account for the possibility of proper motion. The data were binned into three logarithmically spaced energy bands between 1 GeV and 100 GeV and in $0.1° \times 0.1°$ spatial pixels. After the model was optimized by `gtlike`, weights were assigned to each photon (described its coordinates $x$, $y$, and energy $E$) by calculating the fraction of the flux belonging to the candidate source in each pixel:

$$w_{x,y,E} = \frac{\Phi'(x, y, E)}{\sum_i \Phi_i(x, y, E)} \tag{4.8}$$

where $\Phi'(x, y, E)$ is the predicted flux from the candidate source in the pixel and $\Phi_i(x, y, E)$ are the fluxes from all the sources in the model. In addition, the 3FGL PS were masked by assigning a weight of zero to all the photons which fell in a pixel more than 1° from the candidate source position where the summed contribution of the non-candidate PS fluxes exceeded 10% of the total flux in that pixel. This meant that all the photons in the calculation had a high probability of originating either from the candidate source or the diffuse background.

The weighting has little impact on the reconstruction of proper motion because individual photon weights do not change as the likelihood maximization from step 4 optimizes $\vec{x_0}$ and $\vec{v_0}$. However, weighting the photons in this way prevents the algorithm from interpreting photons from nearby sources as originating from the candidate source. Without weighting, we found that flaring nearby sources could mimic a moving source and therefore lead to false positive results.

### 4.3.2 J2310.1−0557

The source J2310.1−0557 passed the proper motion cut with a significance of $4.2\sigma$, and was therefore investigated further. Approximately 9 years (August 2008 to July 2017) of Pass 8 (`P8_SOURCE_V6`) data above 1 GeV in an ROI of 5° around the source location were collected. The increased statistics and improved angular resolution of the Pass 8 data set clearly indicated that J2310.1−0557 lies approximately 1° away from a separate, highly variable source of gamma rays which is not in the 3FGL catalog. This source flared brightly (approximately 150 photons) on 2011 March 7, near the end of the 3FGL time period but was quiet for the remainder of the period. We found that the position of the source was consistent with the Sun, which flared brightly on the same date [189]. gamma-ray emission from the Sun and Moon not included in our models of the ROI. The effect of the solar flare near a candidate PBH was to mimic a moving source, which explains why the proper motion algorithm returned a positive result. Because the sources in the Monte Carlo simulation described in Section 4.4 are placed at random points on the sky, we expect that similar false positives will occur in the simulations. Therefore, we report the upper limit on PBH evaporation rate as if one source passed our criteria, even though J2310.1−0557 is not a good PBH candidate. Incidentally after the publication of the 3FGL source list, J2310.1−0557 was found to be a millisecond pulsar[4].

[4] See https://confluence.slac.stanford.edu/display/SCIGRPS/LAT+Pulsations+from+PSR+J2310-0555

## 4.4 *Fermi*-LAT limits on PBHs

We used Monte Carlo (MC) simulations to derive the efficiency for detecting PBHs, and used the efficiency to place upper limits on the local PBH evaporation rate. We generated a sample of PBHs within 0.08 pc of the Earth with uniform spatial density and random velocities with an average speed of $250\,\mathrm{km\,s^{-1}}$, which is close to an upper bound on orbital velocity of the Sun around the Galactic center [180, 181, 182, 183, 184, 185], and 3-dimensional velocity dispersion equal to the local velocity dispersion of dark matter, $270\,\mathrm{km\,s^{-1}}$ [186]. At the end of this section, we also derive the limits for different assumptions about the PBH distribution, such as the relative velocity and velocity dispersion, to estimate the corresponding systematic uncertainty.

We assume the PBH population has a constant rate of PBH evaporations, $\dot{\rho}_{\mathrm{PBH}} = const$. We also assume a uniform PBH density distribution in the vicinity of the Earth. A constant rate of evaporation implies that the derivative of the PBH density is related to the PBH temperature as:

$$\frac{d\rho_{\mathrm{PBH}}}{dT} \propto T^{-4}. \tag{4.9}$$

The following steps were performed in the derivation of the PBH evaporation rate limit:

1. A sample of PBHs $(T_i, \vec{x}_i, \vec{v}_i)$ was simulated with temperatures $T_i > 5$ GeV and $T_i < 60$ GeV distributed according to Equation (4.9), and distances $R_i$ within $R < 0.08$ pc around the Earth. The velocities $v_i$ of the sample PBHs were distributed with mean equal to the orbital velocity of the Sun, $v_{\mathrm{rot}} = 250\ \mathrm{km\,s^{-1}}$,

and dispersion $v_{\rm disp} = 270$ km s$^{-1}$.

2. For each PBH, we simulated the detection of the photons emitted over the 4 year 3FGL time period, consistent with the PBH evolution. The energies were distributed according to the instantaneous PBH spectrum of the appropriate temperature, and the positions of the photons were smeared according to the *Fermi*-LAT point-spread function (modeled as a Gaussian distribution). The emission spectra of PBHs $\Phi(E,t)$ are discussed in Appendix 4.A. We used a time step of $\Delta t = 1$ day in modeling the evolution of the PBH position and temperature, and the number of photons detected by the *Fermi* LAT each day was given by a Poisson random value with a mean of

$$\overline{N(t)} = \frac{\Delta t}{4\pi R^2} \int_{\rm E=100\ MeV}^{\rm E=500\ GeV} \Phi(E,t) A(E) dE, \tag{4.10}$$

where $A$ is defined as the average *Fermi*-LAT exposure per unit time at the position of the simulated PBH, and $R$ is the distance from the Earth. The energy of each photon was found by random sampling of $\Phi(E,t) \times A(E)$. *Fermi* LAT has relatively uniform exposure on time periods longer than 1 day.

3. The list of simulated PBH photons was concatenated to the real photons present within 5° of the final location of the PBH, with the same data selection as the 3FGL. A likelihood fit using the *Fermi* Science Tool `gtlike` was performed in a 7° × 7° ROI centered at the same location, using a model of the sky which included all 3FGL sources within 5° of the ROI center, as well as models of the

isotropic diffuse and Galactic diffuse emission[5]. The PBH was modeled as a source with a LogParabola spectrum, with fitting parameters restricted to the ranges $1.2 < \alpha < 3.0$ and $0.0 < \beta < 1.0$. Once the likelihood maximization was complete, the PBH was considered detected if its TS value was greater than 25, which is consistent with the 3FGL cutoff.

4. If the PBH source was detected, the results from the likelihood fit were used to find the source flux in the five energy bins reported in the 3FGL catalog. The spectral consistency with a PBH spectrum was then calculated in the same way as described in Section 4.3.

5. If the source was found to be spectrally consistent with a PBH, the significance of any proper motion was evaluated by the algorithm described in Section 4.3. The combined efficiency of steps 3−5 is displayed in Figure 4.3. We smoothed the results by convolving the detectability map with a 3×3 matrix of ones, which had a minor (≈ 8%) impact on the resulting limit. The impact of fluctuations was quantified by observing the change in the limit as the number of simulations increased; we found that an increase of the number of simulations by 100% had less than a 20% change in the resulting limit.

6. To derive an upper limit on the number of PBH evaporations in our search region, we begin with the number of expected detections:

$$N = \rho \epsilon V, \tag{4.11}$$

[5]The models used were the standard Pass 7 (for consistency with the 3FGL) diffuse emission models available from `https://fermi.gsfc.nasa.gov/ssc/data/access/lat/BackgroundModels.html`

where $\rho$ is the true density of PBHs and $V$ is the volume searched. $\epsilon$ is the average PBH detection efficiency in time $t = 4$ yr and within the search volume $V$ (a sphere with radius 0.08 pc, with the wedge corresponding to $|b| < 10^\circ$ removed); it is calculated by taking the mean over the pixels in Figure 4.3 with the weight $R^2T^{-4}$:

$$\epsilon = \frac{\iint \epsilon(R,T)\frac{R^2}{T^4}\,dR\,dT}{\iint \frac{R^2}{T^4}\,dR\,dT}, \tag{4.12}$$

where the integrals run over the space of parameters described in step 1. Equation 4.11 can be inverted to find the PBH density $\rho$ as a function of the number of detections $N$, or the upper limit on $\rho$ given an upper limit on $N$. Given that one PBH candidate passed the selection criteria described in Section 4.3, we set an upper limit $N < 6.64$, which is the 99% confidence upper limit on the mean of a Poisson distribution with 1 observed event.

7. We convert the upper limit on $\rho$ to an upper limit on $\dot{\rho}$ by finding the fraction $f$ of PBHs that would have evaporated during the search time $t$. Given a time of observation of 4 years, we find that all PBHs with initial temperature above 16.4 GeV would evaporate. Therefore,

$$f = \frac{\int_{16.4\ \mathrm{GeV}}^{60\ \mathrm{GeV}} T^{-4}\,dT}{\int_{5\ \mathrm{GeV}}^{60\ \mathrm{GeV}} T^{-4}\,dT}. \tag{4.13}$$

We calculate the 99% upper limit on $\dot{\rho}_{\mathrm{PBH}}$ to be:

$$\dot{\rho}_{\mathrm{PBH}} < f\frac{6.64}{\epsilon V t} = 7.2 \times 10^3\ \mathrm{pc}^{-3}\ \mathrm{year}^{-1}. \tag{4.14}$$

8. We estimated the systematic uncertainties arising from the uncertaintes in the PBH spectrum by varying the overall normalization of the PBH spectrum (see

Appendix 4.A) and varying the velocity distributions of the Milky Way disk and DM halo. We consider two scenarios ("aggressive" and "conservative") which give the best and worst sensitivity, respectively. Steps 1−7 are then repeated to find the resulting limit. The parameters of the aggressive and conservative models, as well as the resulting limits, are listed in Table 4.1.

| Model | Spectrum Normalization | Orbital Velocity ($km\,s^{-1}$) | DM Halo Velocity ($km\,s^{-1}$) | Limit |
|---|---|---|---|---|
| Aggressive | $\frac{0.45}{0.35}$ | 100 | 150 | $4.8 \times 10^3$ $pc^{-3}yr^{-1}$ |
| Conservative | $\frac{0.25}{0.35}$ | 300 | 350 | $15.3 \times 10^3$ $pc^{-3}$ $yr^{-1}$ |

Table 4.1: Parameters used in estimation of systematic uncertainty. To be more conservative in the estimates of the systematic uncertainties, we have tested the ranges of orbital velocities and the DM dispersion velocities which are larger than most of the values reported in the literature [180, 181, 182, 183, 184, 185].

The limit including the systematic uncertainties is

$$\dot{\rho}_{\rm PBH} < (7.2^{+8.1}_{-2.4}) \times 10^{3}\ \rm{pc}^{-3}\ \rm{yr}^{-1}. \tag{4.15}$$

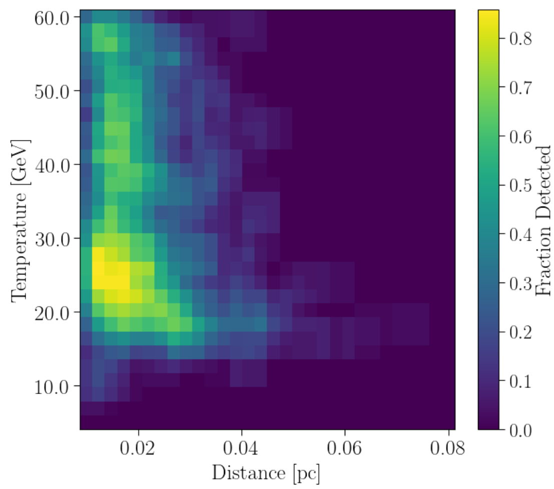


Figure 4.3: Fraction of simulated PBHs which are detected as a point source with a spectrum compatible with a PBH evaporation spectrum and with significant proper motion. The detectability peaks for PBHs with initial temperatures above 16.4 GeV because the lifetime of a 16.4 GeV PBH is 4 years, which is the same as the observation period of the 3FGL. Few PBHs are detected past a distance of 0.05 pc or below 10 GeV.

## 4.5 Discussion and Conclusions

The potential existence of PBHs that emit detectable Hawking radiation is one of the most intriguing features of some theories of cosmological evolution. In addition to providing evidence for these theories, the possibility for direct observation of Hawking radiation (which would be a major discovery in its own right) was our main motivation for the search of PBHs with the *Fermi* LAT.

In this paper we searched for individual PBHs among 3FGL catalog sources.

We performed calculations showing that the characteristic distance to a detectable PBH is of order $\sim 0.03$ pc, in which case the proper motion of the PBH must be taken into account. We developed a new algorithm which can detect the proper motion of a point source in the presence of a known background. We found several 3FGL sources that have spectra consistent with PBHs, but none of these sources exhibit proper motion which would be the smoking-gun signature of a PBH in the *Fermi*-LAT sensitivity domain. As a result, we derived upper limits on the local PBH evaporation rate.

To derive the efficiency of a PBH passing our selection criteria, we developed a Monte Carlo that simulates PBHs with realistic velocity distribution and initial temperature distribution expected for the steady-state evaporation rate of the PBHs. The efficiency was then used to find the upper limits on the local PBH evaporation rate. The inferred systematic uncertainties are related to the uncertainties in the PBH gamma-ray spectrum as well as the uncertainties in the Galactic rotational velocity and the DM velocity dispersion. We calculated upper limits in scenarios for which these parameters covered a wide range of reasonable values.

In Figure 4.4, we compare the *Fermi*-LAT upper limit on the rate of PBH evaporations with the limits from Cherenkov telescopes and observe that they are similar. Although ground-based gamma-ray observatories are sensitive to timescales of a minute or less, and *Fermi* LAT is sensitive to timescales of months to years, both the Cherenkov telescopes and the *Fermi* LAT are probing the same quasi-stationary population of PBHs.

The local evaporation rate can be related to the local mass density (relative

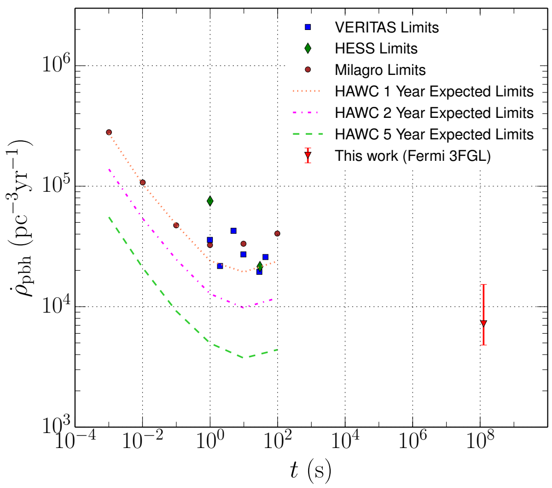


Figure 4.4: Comparison of the *Fermi*-LAT 99% confidence upper limit with the limits from VERITAS [190], H.E.S.S. [172], Milagro [173], and the expected limits from HAWC [173]. The error bars around the *Fermi*-LAT limit correspond to the systematic uncertainty described in the text.

to the critical density $\rho_{\mathrm{c}}$) as [134]

$$\Omega_{\mathrm{pbh}}^{\mathrm{loc}} = \frac{M_*}{(\alpha - 2)} \frac{\tau_0}{\rho_{\mathrm{c}}} \dot{\rho}_{\mathrm{pbh}}, \tag{4.16}$$

where $\alpha$ is the index of the initial distribution of PBH masses, $dn/dM \sim M^{-\alpha}$, and $M_*$ is the mass of a PBH with the lifetime equal to the age of the Universe. In the following, we will assume $\alpha = 2.5$, which corresponds to PBHs formed in the radiation-dominated era [134]. The local density of PBHs corresponding to the evaporation rate in Equation (4.15) is $\Omega_{\mathrm{pbh}}^{\mathrm{loc}} \leq (3.6^{+4.1}_{-1.2}) \times 10^2$. In general, the distribution of the PBH masses does not need to follow a power-law function. If there is a short period of low-pressure dustlike equation of state or a phase transition (see, e.g., the discussion in [153] and references therein), then the PBH masses will be distributed around the mass in Equation 4.1, where $t$ is the time of the PBH formation. In order for the PBHs to be evaporating now we need $M \sim 10^{15}$ g which corresponds to the formation time $t \sim 10^{-23}$ s after the Big Bang [153]. Thus, in general, limits on local PBH evaporation can constrain models where PBHs are formed with lifetimes close to the lifetime of the Universe, i.e., the PBHs which are close to evaporation now. This requires certain "fine-tuning" of the time when the PBHs are formed. If, for example, the PBHs are formed close to the QCD phase transition with $t_Q \sim 10^{-4}$ s and $T_Q \sim 100$ MeV, then the PBH masses are $M \gtrsim 5M_\odot \approx 10^{34}$ g [191]. These PBHs have a temperature much smaller than $10^{-7}$ K and lifetime much longer than the lifetime of the Universe, i.e., they cannot be detected by the *Fermi* LAT.

The local density of PBHs is expected to be enhanced compared to the average density in the Universe in a similar way that the density of DM in the Galaxy is larger than the average density of DM in the Universe. The enhancement factor for DM near the Sun [154] compared to the average DM density [192] is $k \sim 2.2 \times 10^5$. With this enhancement, the limit on the average PBH density is $\Omega_{\rm pbh} \leq (1.5^{+1.7}_{-0.5}) \times 10^{-3}$. This limit is several orders of magnitude less constraining than the limits obtained from extragalactic and Galactic gamma-ray backgrounds $\Omega_{\rm pbh} \leq 10^{-8} - 5 \times 10^{-10}$ [153, 169, 170]. The latter limits are calculated either by integrating the PBH evaporations inside the visible Universe or inside the halo of our Galaxy, i.e., they are derived on kpc to Gpc scales, while the limit in this paper is derived for distances less than a fraction of a pc.

The limit on the average current density of PBHs can be translated to a limit on the density of PBHs at the time of formation, $\beta \sim 10^{-18}\Omega_{\rm pbh}\sqrt{M/10^{15}{\rm g}}$ [153, 165]. This limit, in turn, can be used to constrain the spectrum of density fluctuations in the early Universe [167, 193, 194]. In some cases, non-observation of PBHs provides the only way to limit theories of inflation, especially the theories that predict large fluctuations of density at small distances [e.g., 167].

The *Fermi*-LAT Collaboration acknowledges generous ongoing support from a number of agencies and institutes that have supported both the development and the operation of the LAT as well as scientific data analysis. These include the National Aeronautics and Space Administration and the Department of Energy in the United States, the Commissariat à l'Energie Atomique and the Centre National de la Recherche Scientifique / Institut National de Physique Nucléaire et de Physique des Particules in France, the Agenzia Spaziale Italiana and the Istituto Nazionale di Fisica Nucleare in Italy, the Ministry of Education, Culture, Sports, Science and Technology (MEXT), High Energy Accelerator Research Organization (KEK) and Japan Aerospace Exploration Agency (JAXA) in Japan, and the K. A. Wallenberg Foundation, the Swedish Research Council and the Swedish National Space Board in Sweden.

Additional support for science analysis during the operations phase is gratefully acknowledged from the Istituto Nazionale di Astrofisica in Italy and the Centre National d'Études Spatiales in France. This work performed in part under DOE Contract DE-AC02-76SF00515.

The authors would like to thank Jane MacGibbon for numerous helpful discussions.

*Facility: Fermi.*

*Software:*Astropy [`http://www.astropy.org`, 195], matplotlib [196].

## 4.A Spectrum of Gamma Rays from Primordial Black Holes

One of the most important factors in the systematic uncertainty of the limit on PBH evaporation is the spectrum of emitted gamma rays. The spectrum of fundamental particles emitted by the black hole was computed by [140]. Quarks and gluons emitted by PBHs hadronize into mesons and baryons, which subsequently decay into stable particles. The spectra of the stable particles emitted by PBHs at high temperatures were computed by [197].

To obtain the spectra of gamma-ray emission from PBHs we use the values given in [197] for $T_{\rm PBH} = 0.3, 1, 10, 50, 100$ GeV and interpolate for different values of PBH temperatures. To cross-check numerical calculations, we use two different interpolation methods:

- We use an analytic approximation by fitting the PBH emission rate $\dot{N}_\gamma(E, T)$ with a cubic log polynomial

  $$\log \dot{N} = c_0(T) + c_1(T) \log x + c_2(T)(\log x)^2 + c_3(T)(\log x)^3,$$

  where $x = E/T$ and interpolate the fit coefficients $c_i(T)$ (we use this appriximation in Section 4.2).

- We create a table for a set of $E$ and $T$ values and use a 2-dimensional interpolation directly from the results in [197] (this approximation is used in Sections 4.3 and

4.4).

We compare the first interpolation with other parametrizations available in the literature [134, 198] in Figure 4.5 left. There seems to be a rather significant discrepancy in the total energy emitted in gamma rays. For instance, [197] found that 24 – 25% of the energy is emitted in gamma rays for a large range of initial temperatures, while analytical integration of the parametrization [199, 200]

$$\frac{dN_\gamma}{dE_\gamma} = 9 \times 10^{35} \begin{cases} \left(\frac{1\,\mathrm{GeV}}{T_\tau}\right)^{3/2} \left(\frac{1\,\mathrm{GeV}}{E_\gamma}\right)^{3/2} \mathrm{GeV}^{-1} & E_\gamma < T_\tau; \\ \left(\frac{1\,\mathrm{GeV}}{E_\gamma}\right)^{3} \mathrm{GeV}^{-1} & E_\gamma \geq T_\tau \end{cases} \tag{4.17}$$

gives about 47% of the energy in gamma rays. A more-recent parametrization of the gamma-ray spectra at temperatures $\gtrsim 1$ TeV [Figure 11 of 187] gives about 35% of the energy in gamma rays.

For our baseline model, we take the spectrum of [197] rescaled to give 35% of energy in gamma rays to match the more-recent calculation in [187]. For the calculations, we use the interpolation presented in Figure 4.5 (right). At low temperatures, the "Interpolation" curve is calculated by taking instantaneous PBH spectrum from [197] rescaled to 35% energy going to gamma rays times 4 years. At temperatures above the temperature of a PBH with the 4 years lifetime, the "Interpolation" curve is the [199] parametrization rescaled by 0.45. There is a good agreement between the integrated spectra of [197] (rescaled to 35% efficiency) and the "Interpolation" curve.

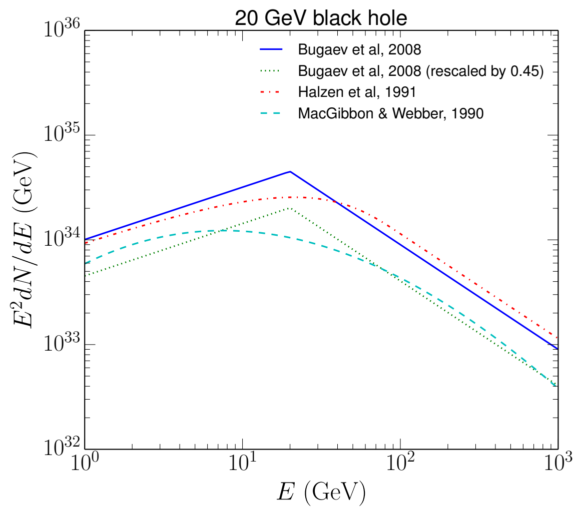


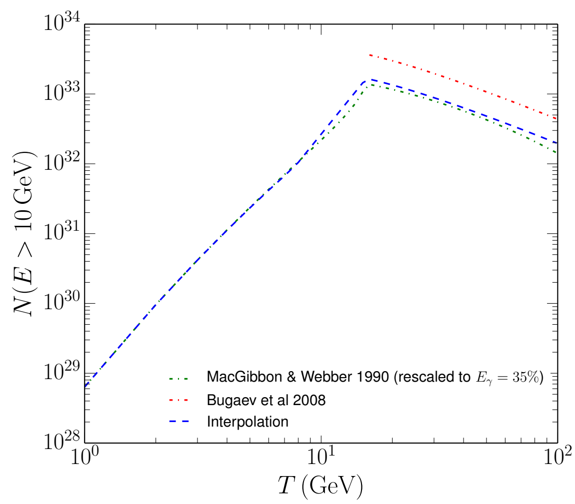


Figure 4.5: Left: spectrum of a PBH with initial temperature $T = 20$ GeV integrated over its lifetime of 2.1 years. Right: total number of photons emitted above 10 GeV during 4 years as a function of initial PBH temperature. See text for the description of the "Interpolation" curve.

# Chapter 5

# $p$-wave DM Annihilation

The purpose of this chapter is motivate and describe the phenomenology of the DM model searched for in Chapter 6.

Unlike the DM models typically considered by indirect DM searches, the model described here (the *hidden sector axion portal* or HSAP model) does not make the broad assumption of an annihilation cross-section that is independent of velocity; instead, the HSAP model has an annihilation cross-section that depends on the square of the relative velocity of the incoming DM particles. This fact allows the DM to evade detection by traditional indirect searches, as well as by collider and direct detection experiments.

Section 5.1 introduces the class of models ("secluded DM") of which the HSAP model is a representative example, while Sections 5.2 and 5.3 derive the spatial and spectral phenomenology, respectively, of the potential $\gamma$-ray signal from the HSAP model.

## 5.1 Secluded DM

Section 1.1.4 introduced the idea of weakly interacting massive particles (WIMPs) as well-motivated DM candidates. In that section, it was shown that if WIMPs were produced thermally in the early Universe, a straightforward calculation of their relic abundance via freeze-out reproduces the observed DM density, given a weak-scale annihilation cross-section (the so-called 'WIMP miracle'). Typical WIMP models assume a thermally averaged annihilation cross-section that is velocity-independent, and has a canonical value of $\langle\sigma v\rangle = 3 \times 10^{-26}\,\mathrm{cm}^3\,\mathrm{s}^{-1}$.

Given their proximity and DM richness, certain regions, such as the Galactic center and dwarf spheroidal galaxies, are excellent targets for WIMP annihilation searches with indirect detection. Unfortunately, the most straightforward WIMP models (those assuming the canonical thermal relic cross-section) have been ruled out for WIMP masses below a few hundred GeV (see Figure 1.8). This lack of experimental evidence has motivated recent work on so-called "secluded" or "nightmare" DM, a class of models which can still successfully reproduce the appropriate relic DM abundance, but are difficult to detect experimentally. Generically, secluded DM posits a WIMP ($\chi$), along with a dark mediator ($a$) which mixes with the SM [201]. If the WIMP mass ($m_\chi$) is smaller than the mediator mass ($m_a$), any mixing between the dark sector and the SM relies on virtual mediators (see the left panel of Figure 5.1), and strong constraints on the coupling can be placed with accelerator and direct detection probes. Therefore, in secluded DM models, the WIMP mass is taken to be larger than that of the mediator,

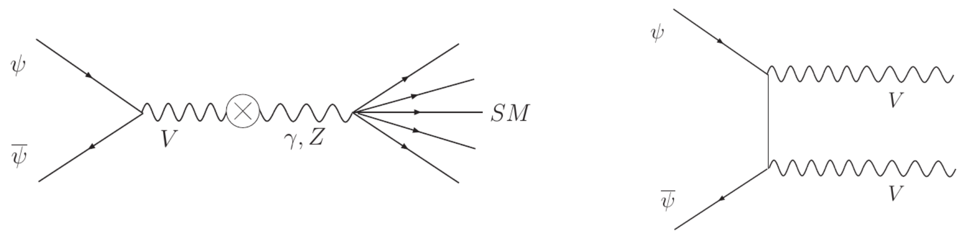


Figure 5.1: *Left panel*: $s$-channel annihilation (i.e. annihilation through a single intermediate state) of DM particle $\psi$ into SM final states, via a virtual mediator $V$ which mixes with the SM. *Right panel*: $t$-channel annihilation (i.e. annihilation via scattering by $\psi$) into metastable mediators $V$. The coupling between $\psi$ and $V$ need only be small enough to produce the correct relic abundance. *Note:* The notation here is different from in the text: $\psi$ corresponds to the WIMP $\chi$, and $V$ corresponds to the mediator $a$. Figure reproduced from [201].

meaning the mediator will be on-shell in an annihilation (right panel of Figure 5.1). In this case, the mediator $a$ can be fairly long-lived (the only constraints on the coupling of $a$ to the SM are placed by requiring $a$ to decay before BBN at a time of around 1s after the Big Bang). With such a small coupling to the SM, it is extremely unlikely for accelerators to produce $\chi$, and the cross-section for $\chi$ scattering off SM particles in a direct detection experiment will be very small.

Indirect detection methods, however, are capable of probing this class of model: even a mediator with the smallest possible SM coupling (i.e. the longest lifetime), given the constraints from BBN, must decay in less than about 1s. The mediator therefore can travel at most about 1 light-second from the annihilation location before decaying, which is a small distance on Galactic or cosmological scales. The indirect detection signal then remains tied directly to the WIMP density, while the direct detection and collider signals are negligible.

A representative example of such a model is the *hidden sector axion portal* (HSAP) model of Shelton, Shapiro, and Fields [202]. The HSAP model posits a Majorana DM particle $\chi$ that annihilates to pairs of dark pseudoscalars $a$ that in turn decay to pairs of photons (See Figure 5.2). The HSAP Lagrangian contains the terms:

$$\mathcal{L} \supset -\frac{m_\chi}{2}(\chi\chi + \text{h.c.}) - \frac{i}{2} y a(\chi\chi - \text{h.c.}) - \frac{m_a^2}{2}a^2 \tag{5.1}$$

describing a spin-$\frac{1}{2}$ Majorana WIMP $\chi$ with mass $m_\chi$, and a pseudoscalar $a$ with mass $m_a$. Here h.c. refers to the Hermitian conjugate of $\chi\chi$, and is included because $\chi$ is a Majorana fermion (that is, $\chi$ is its own antiparticle). The interaction between $\chi$ and $a$ is given by the second term, with the dimensionless Yukawa coupling $y$. The coupling of $a$ to photons occurs via a dimensionful coupling $1/\Lambda$, where $\Lambda$ is assumed to be much larger than $m_a$. In the HSAP model, the coupling of $a$ to gluons is assumed to be zero, meaning that the branching ratio for $a \to \gamma\gamma$ is O(1).

In addition to being difficult to detect via direct detection or collider probes (due to the small coupling $1/\Lambda$), the HSAP evades most current constraints from indirect detection due to the fact that its annihilation cross-section is velocity-suppressed. DM today is presumed to be nonrelativistic ($\beta \sim 10^{-3}$), but the WIMP freezes out at the much higher temperature of (recalling the results of Section 1.1.4.1):

$$x = \frac{m_\chi c^2}{kT} = 20 \to kT = \frac{m_\chi c^2}{20} \tag{5.2}$$

where $k$ is the Boltzmann constant, and factors of $c$ have been restored for clarity. The most probable velocity in a Maxwell-Boltzmann distribution is $v_p = \sqrt{\frac{2kT}{m}}$, which at

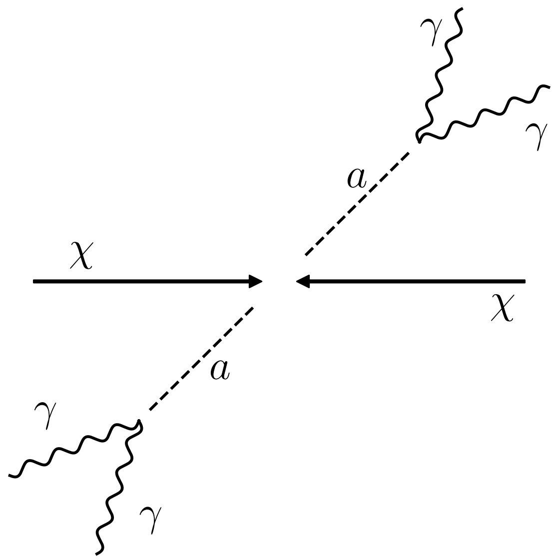


Figure 5.2: Cartoon diagram of the process described in the text: two WIMPs $\chi$ annihilate to a pair of dark pseudoscalars $a$, which in turn decay to pairs of photons $\gamma$.

freeze-out is:

$$v_p = \sqrt{\frac{2m_\chi c^2}{20m_\chi}} = \frac{c}{\sqrt{10}} \approx 0.3c \tag{5.3}$$

The next section derives the (leading order) velocity dependence of the HSAP annihilation cross-section to be a term proportional to $v^2$. Annihilation today will therefore be suppressed by about 5 orders of magnitude compared to the early Universe—truly a nightmare scenario!

### 5.1.1 Velocity dependence of $\langle \sigma v \rangle$

The expansion of a DM annihilation cross-section $\langle \sigma v \rangle$ in powers of $v^2$ is related to the partial wave expansion of solutions of the nonrelativistic Schrödinger equation.

In nonrelativistic quantum mechanics, the probability of scattering via a potential $V(r)$ can be expressed through the nontrivial part of the scattering matrix $S = 1+iT$ , which relates the initial and final states [203]:

$$T_{i,f} = \langle f|V|i\rangle = \int \psi_f V(r)\psi_i du \tag{5.4}$$

where the initial and final scattering states $|i\rangle$ and $|f\rangle$ have been replaced with position-space wavefunctions $\psi_i(\vec{x}) = \langle \vec{x}|i\rangle$ and $\psi_f(\vec{x}) = \langle \vec{x}|f\rangle$. Generally, the potential $V(r)$ is assumed to be small in magnitude and localized to a volume $u$, in which case $T$ can be found via perturbative methods. Although $|i\rangle$ and $|f\rangle$ can in principle be any function of time and space, it is convenient to characterize the problem in terms of eigenstates of momentum. Expanding these incoming and outgoing states (with momentum labeled by $k$) in partial waves gives:

$$\psi_k = \sum_{l,m} A_{l,m}\psi_{k,l,m} = \sum_{l,m} A_{l,m}Y_{l,m}(\theta,\phi)R_{k,l}(r) \tag{5.5}$$

where the $Y_{l,m}(\theta, \phi)$ are the spherical harmonics, and $R_{k,l}(r)$ solves the 1-dimensional radial Schrödinger equation. The expansion coefficients $A_{l,m}$ and the $Y_{l,m}(\theta, \phi)$ can be ignored for the purposes of this derivation because they do not contain any information about the momentum $k$. Instead, all of the $k$ dependence is carried by $R_{k,l}(r)$, which is given by:

$$R_{k,l}(r) = \sin(\delta_l)j_l(kr) + \cos(\delta_l)n_l(kr) \tag{5.6}$$

where $\delta_l$ is a phase shift between the incoming and outgoing waves. The Neumann functions $n_l(kr)$ are neglected because they are undefined at $r = 0$, and the Bessel functions $j_l(kr)$ can be approximated at low momentum ($kr << 1$) by:

$$j_l(kr) \approx \frac{(kr)^l}{(2l+1)!!} \tag{5.7}$$

Then, since $k \approx mv$ for nonrelativistic particles:

$$\psi_{i,f}(r) \propto \sum_{l=0}^{\infty} R_l(r) \propto \sum_{l=0}^{\infty} v_{i,f}^l \tag{5.8}$$

And, from Equation 5.4:

$$T_{i,f} \propto \sum_{l=0}^{\infty} \int v_i^l v_f^l du \tag{5.9}$$

The probability of interaction is given by the cross-section, which is proportional to $T^2$ [87]:

$$d\sigma = \frac{1}{4E_1E_2|\vec{v}_1 - \vec{v}_2|}|T|^2 d\Pi_{LIPS} \tag{5.10}$$

where the $E_n$ are the energies of the incident particles, $v_n$ are their respective velocities, and $d\Pi_{LIPS}$ is the Lorentz-invariant phase space, which depends on the properties of the particles in the final state. Multiplying each side by $v \equiv |\vec{v}_1 - \vec{v}_2|$, the total cross-section (now integrated over $d\Pi_{LIPS}$) can be written as a sum over initial $l$ states. Because the differential cross-section $d\sigma$ depends on the norm of the transfer matrix $T$, two powers of velocity $v$ end up on the right hand side of the equation:

$$\sigma v = \sum_l c_l v^{2l} = A + Bv^2 + Cv^4... \tag{5.11}$$

where $A$ corresponds to $l = 0$, $B$ corresponds to $l = 1$ and so on.

In a theory that conserves parity (P) [1], the $l = 0$ ($s$-wave) contribution to the annihilation cross-section is zero for Majorana fermions annihilating to a spin-0, P-even final state, and the dominant contribution comes from the $l = 1$ ($p$-wave) term. This can be seen by considering each of the following two possibilities, recalling that both helicity (the normalized projection of a particle's spin onto its momentum) and angular momentum must be conserved:

1. In the center-of-mass (COM) frame, if the net spin angular momentum is zero, the DM particles must both be right-handed (helicity $\frac{m_s}{s} = +1$) or left-handed ($\frac{m_s}{s} = -1$), in which case the total helicity is $\pm 2$. The final state contains two scalar particles with zero helicity, so this annihilation does not conserve helicity.

2. If the DM particles have opposite helicity in the COM frame, their spins must be aligned with one another, in which case the total angular momentum of the system is $\pm\hbar$. Again, the final state only contains spin-0 particles, so angular momentum is not conserved.

If orbital angular momentum exists ($l > 0$) in the system, however, the second interaction can proceed as the spin angular momentum and orbital angular momentum can cancel one another.

Since $\langle \sigma v \rangle \propto v^2$, a mechanism must be invoked to increase the DM velocity dispersion, if one hopes to see signals of annihilating DM of this type today (when DM is cold). Such a mechanism is discussed next.

[1] A parity transformation is defined as $P(t, \vec{x}) \rightarrow (t, -\vec{x})$. Under such a transformation, a state $\psi$ can be either even ($P\psi = \psi$) or odd ($P\psi = -\psi$). Conservation of parity implies that helicity is also conserved.

## 5.2 Black Hole Spikes

The DM halo density profile remains a mystery, due to the unknown nature of any interactions that the DM might have with itself or with baryonic matter. High resolution simulations, however, do provide clues about what the profile might look like. A canonical result comes from Navarro, Frenk, and White (NFW) [204], who performed simulations in 1997 that showed the density of dark matter $\rho_{DM}(r)$ is reasonably well-described by the following profile under a wide variety of cosmologies, and across several orders of magnitude in halo mass:

$$\rho(r) = \frac{\rho_0}{\frac{r}{r_S}(1 + \frac{r}{r_S})^2} \tag{5.12}$$

which has two free parameters: a normalization density $\rho_0$, and a distance scale $r_S$. In the NFW model, the density increases as $r^{-1}$ near the center of the halo ($r \ll r_S$), and smoothly transitions to $r^{-3}$ as $r$ increases.

Other simulations tend to confirm that the density profile follows a power law $r^{-\gamma_c}$ at small $r$ , though the reported values of $\gamma_c$ range anywhere from $\gamma_c = 0$ (a core) [205], to $\gamma_c \sim 1.5$ (the Moore profile) [206]. Typical values of $\gamma_c$ are between 0.9 and 1.2 [207, 208]. In any case, the gravitational field of a supermassive black hole (SMBH) will concentrate the DM into an even steeper power law (a black hole "spike") in its region of influence. Since the DM annihilation rate is proportional to the square of the DM density, the exact nature of this density spike has important implications for the possibility of observing annihilation products.

If the DM is capable of annihilation, a power-law density profile cannot exist all the way to $r = 0$, because annihilation will remove DM at high densities. Some authors have therefore suggested [209] the presence of an annihilation plateau, a radius within which the density is constant:

$$\rho_{\text{ann}} = \frac{m_\chi}{\langle \sigma v \rangle T} \tag{5.13}$$

where $T$ is the age of the galaxy. More recent work [210], however, has pointed out that the derivation of such a plateau relies on the assumption that the DM moves only in circular orbits, and the presence of highly elliptical orbits around the SMBH will restore a weak cusp: a region in which the density increases as $r^{-\frac{1}{2}}$. The derivation of $\rho_\chi(r) \propto r^{-\frac{1}{2}}$ assumes that any DM particle trapped within the particular radius $r_{\text{ann}}$ (corresponding to the edge of the annihilation plateau, Equation 5.13) will annihilate in time $T$, while DM in elliptical orbits that spend time outside $r_{\text{ann}}$ will survive [211].

In a real galaxy, the situation will be more complex due to the presence of baryonic matter, which may either steepen the DM profile by adiabatic contraction [212], or soften it via dynamical friction or supernova feedback [205]. Furthermore, DM whose annihilation cross-section is velocity-dependent is expected to have a somewhat flatter density profile than $s$-wave annihilating DM, because the DM velocity dispersion (and therefore annihilation rate) depends inversely on the distance from the SMBH [211]. Various DM density profiles in the vicinity of an SMBH for a given annihilation cross-section, and allowing for the capture of DM by the SMBH, are shown in Figure 5.3.

To support the increase in density, the velocity dispersion within the weak

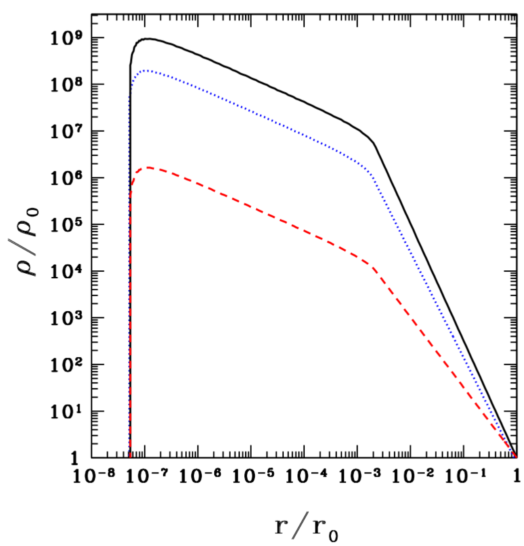


Figure 5.3: DM density profile near a SMBH, under three powerlaw assumptions for the density profile outside the annihilation radius $r_{\rm ann}/r_0 = 2.2\times10^{-3}$: $\gamma_{\rm sp} = 2.5$ (black line), $\gamma_{\rm sp} = 2.25$ (blue dotted line), and $\gamma_{\rm sp} = 1.5$ (red line). Here $r_0$ is the fiducial outer edge of the density spike (i.e. where the DM profile is matched to the NFW profile) and can be estimated as $r_0 \approx GM/v_0^2$, where $v_0$ is the DM velocity dispersion in the halo. The capture radius of the SMBH is located at $r_{\rm ann}/r_0 = 5\times10^{-8}$. Figure reproduced from [211].

cusp must also increase. Solving the Jeans equation in the vicinity of the SMBH and matching the solution to a constant velocity dispersion in the halo, Shelton et al. find a velocity spike that extends out to about 1.7 pc from the SMBH [202]. At the Earth, 8 kpc away, the angular size of the velocity spike is about 0.012°, well below the *Fermi*-LAT PSF at all energies. In other words, the $\gamma$-ray signal from $p$-wave annihilating DM is restored, though its spatial morphology is radically different from the $s$-wave case, and would look instead like a point source spatially coincident with Sgr $A^*$.

## 5.3 Annihilation spectrum

The main purpose of this section is to derive the $\gamma$-ray spectrum of annihilating DM, given the HSHP model of Equation 5.1. In the HSHP model, DM particles $\chi$ annihilate into two dark scalars $a$, which in turn each decay to two photons (see Figure 5.2). The branching ratio $a \rightarrow \gamma\gamma$ is assumed to be 100% (see Section 5.1) here and in Chapter 6. Assuming the DM particles are nonrelativistic, the dark scalars are each produced with total relativistic energy $m_\chi$ ($c \equiv 1$). Because the scalar $a$ is lighter than $\chi$, the COM frame of each scalar is boosted compared to the Galactic frame.

The Lorentz factor $\gamma$ can be found beginning with the four-momentum of the dark scalar[2]:

$$p = (E, \vec{\mathbf{p}}) = (m_\chi, \vec{\mathbf{p}}) \tag{5.14}$$

[2]Indices on four-vectors have been suppressed in this section, as the meaning should be clear without them

The relativistic energy of $a$ is given by $E_a = \gamma m_a$, so $\gamma$ can be immediately read off as:

$$\gamma = \frac{m_\chi}{m_a} \tag{5.15}$$

Because $\gamma = \frac{1}{\sqrt{1-\beta^2}}$, where $\beta = |\vec{\mathbf{v}}|$, $\beta$ can also be easily derived:

$$\beta = \sqrt{1-\gamma^{-2}} = \sqrt{1-\frac{m_a^2}{m_\chi^2}} \tag{5.16}$$

In the COM frame of the dark scalar, the photons (which follow the relation $E = |\mathbf{p}|$) are emitted back-to-back with energy $m_a$, and therefore each have four-momentum:

$$p = (E, \vec{\mathbf{p}}) = (\frac{m_a}{2}, \vec{\mathbf{p}}) \tag{5.17}$$

If the coordinate systems of the Galactic and COM frames are defined such that they are aligned along the $x$-axis, the energy of the photon in the Galactic frame can be calculated by boosting the photon four-momentum via the Lorentz boost matrix:

$$\Lambda = \begin{pmatrix} \gamma & -\gamma\beta & 0 & 0 \\ -\gamma\beta & \gamma & 0 & 0 \\ 0 & 0 & 1 & 0 \\ 0 & 0 & 0 & 1 \end{pmatrix} \tag{5.18}$$

The boosted photon four-momentum is then[3]:

$$p' = (\gamma\frac{m_a}{2} - p_x\gamma\beta, \vec{\mathbf{p}}') \tag{5.19}$$

[3]Here and below, the prime symbol ($'$) refers to the Galactic frame, while un-primed variables are understood to be in the COM frame of the dark scalar

Substituting the values of $\gamma$ and $\beta$ from above, and noting that $p_x = |\mathbf{p}|\cos(\theta)$ (where $\theta$ is measured in the COM frame, and ranges from 0 to $\pi$), the energy of the photons in the Galactic frame are given by the $0^{\text{th}}$ component of $p'$:

$$E_{\gamma}' = \frac{m_\chi}{2}\left(1 - \sqrt{1 - \frac{m_a^2}{m_\chi^2}}\cos(\theta)\right) \tag{5.20}$$

Since $a$ is a scalar, the photons it decays into are emitted isotropically in the COM frame. Therefore the angular distribution of $\theta$ is:

$$f(\theta)d\theta = \frac{1}{2}\sin(\theta)d\theta \tag{5.21}$$

The energy distribution of the boosted photons in the Galactic frame is:

$$f(E')dE' = f(\theta)\frac{d\theta}{dE'}dE' = \frac{f(\theta)}{\frac{dE'}{d\theta}}dE' \tag{5.22}$$

Differentiating Equation 5.20 with respect to $\theta$ yields:

$$\frac{dE'}{d\theta} = \gamma\frac{m_a}{2}\beta\sin(\theta) \tag{5.23}$$

Substituting Equation 5.23 into Equation 5.22 gives a flat distribution:

$$f(E')dE' = \frac{\frac{1}{2}\sin(\theta)}{\gamma\frac{m_s}{2}\beta\sin(\theta)}dE' = \frac{dE'}{\sqrt{m_\chi^2 - m_a^2}} \tag{5.24}$$

The expected $\gamma$-ray spectrum is therefore bounded at $E' = \frac{m_\chi}{2}\left(1 \pm \sqrt{1 - \frac{m_a^2}{m_\chi^2}}\right)$, corresponding to emission of the photons along $\theta = 0$ and $\theta = \pi$, and flat in between—a box shape. The box is centered at $\langle E' \rangle = \frac{m_\chi}{2}$ as expected, since each dark matter particle $\chi$ leads to two photons in the final state, and has a width determined by the ratio of the dark particle masses. In Chapter 6, two different representative values of the parameter $\zeta \equiv \frac{m_a^2}{m_\chi^2}$ are used in a search of *Fermi*-LAT data for $p$-wave annihilating DM.

# Chapter 6

# Search for Gamma-ray Emission from p-wave Dark Matter Annihilation in the Galactic Center

This chapter (aside from this title page) is a reproduction of the previously published article: *Search for Gamma-ray Emission from p-wave Dark Matter Annihilation in the Galactic Center*, submitted to Physical Review D, February 2019

Some minor changes to the formatting have been made in order to match the style of the rest of this document, however, no changes to the content have been made. The references in this chapter are displayed in the main Bibliography below, for convenience. The coauthors of this paper have given permission for this material to be reprinted here; their letters of permission are attached.

# Search for Gamma-ray Emission from p-wave Dark Matter Annihilation in the Galactic Center

C. Johnson[1], R. Caputo[2], C. Karwin[3], S. Murgia[3], and S. Ritz[1]

(*Fermi*-LAT Collaboration)

J. Shelton[4]

[1] *Santa Cruz Institute for Particle Physics, Department of Physics and Department of Astronomy of Astrophysics, University of California at Santa Cruz, Santa Cruz, CA 95064, USA*

[2] *Center for Research and Exploration in Space Science and Technology (CRESST) and NASA Goddard Space Flight Center, Greenbelt, MD 20771, USA*

[3] *Physics Department, University of California at Irvine, Irvine, CA 92657, USA*

[4] *Department of Physics, University of Illinois at Urbana-Champaign, Urbana, IL 61801, USA*

## Abstract

Indirect searches for dark matter through Standard Model products of its annihilation products generally assume a cross-section which is dominated by a term independent of velocity ($s$-wave annihilation). However, in many DM models an $s$-wave annihilation cross-section is absent or helicity suppressed. To reproduce the correct DM relic density in these models, the leading term in the cross section is proportional to the DM velocity $v^2$ ($p$-wave annihilation). Indirect detection of such $p$-wave DM is difficult because the average velocities of DM in galaxies today are orders of magnitude slower than the DM velocity at the time of decoupling from the primordial thermal plasma, thus suppressing the annihilation cross-section today by some five orders of magnitude relative to its value at freeze out. Thus $p$-wave DM is out of reach of traditional searches for DM annihilations in the Galactic halo. Near the region of influence of a central supermassive black hole, such as Sgr A*, however, DM can form a localized over-density known as a "spike". In such spikes the DM is predicted to be both concentrated in space and accelerated to higher velocities, thereby allowing the $\gamma$-ray signature from its annihilations to potentially be detectable above the background. We use the *Fermi* Large Area Telescope to search for the $\gamma$-ray signature of $p$-wave annihilating DM from a spike around Sgr A* in the energy range 10 GeV-600 GeV. Such a signal would appear as a point source and would have a sharp line or box-like spectral features difficult to mimic with standard astrophysical processes, indicating a DM origin. We find no significant excess of gamma rays in this range, and we place upper limits on the flux in $\gamma$-ray boxes originating from the Galactic Center. This result, the first of its kind, is interpreted in the context of different models of the DM density near Sgr A*.

## 6.1 Introduction

There are strong indications that a significant component of matter in the universe is not described by the Standard Model (SM). Observational evidence for this new, *dark* form of matter comes from its gravitational influence on visible matter in measurements ranging from the early Universe to the present day [213, 214, 215, 216]. The particle properties of dark matter (DM), however, remain elusive.

One of the most straightforward mechanisms to produce DM in the early universe is thermal freezeout. In this scenario, DM has interactions with other fields, possibly but not necessarily SM particles, that ensure DM is part of the thermal radiation bath that fills the early universe. As the universe cools, the DM annihilation rate drops below the Hubble rate and annihilations freeze out, leaving a thermal relic abundance of DM. The DM annihilation cross-section is thus directly related to its cosmic abundance, and yields predictions for the residual DM annihilation rate in galaxy halos today. Generically, the leading contribution to the thermally-averaged DM annihilation cross-section $\langle \sigma v \rangle$ will be from velocity-independent $s$-wave processes, so that the present-day annihilation cross-section is the same as its value during thermal freeze out [217]. Such $s$-wave thermal cross-sections generally produce $\gamma$-ray and cosmic-ray signals at interesting (and potentially observable) rates. The *Fermi* Large Area Telescope (*Fermi*-LAT), for instance, is capable of probing the $s$-wave thermal cross-section for DM masses up to a few hundred GeV across a variety of annihilation channels [218]. The latest generation of cosmic-ray detectors (e.g. AMS-02, PAMELA) is similarly sensitive; an observed excess of high-energy antiprotons can be interpreted as the annihilation signal of DM with a thermal cross-section [219, 220].

In many models, however, symmetries forbid the $s$-wave contribution to the annihilation cross-section, and the leading contribution to DM annihilations occurs in the $p$-wave, $\langle \sigma v \rangle \propto v^2$. For instance, charged scalar DM annihilating to the SM through an $s$-channel gauge boson has its leading contribution in the $p$-wave as a consequence of angular momentum conservation [221]. Another example is provided by fermionic Higgs portal DM [222, 223]; here $CP$ (charge and parity) conservation enforces the vanishing of the $s$-wave annihilation cross-section. $CP$ conservation also ensures $p$-wave annihilation cross-sections in a broad and natural class of secluded DM models [201, 202, 224, 225]. In these models, fermionic DM freezes out via annihilations to light (e.g. pseudo-Nambu-Goldstone) bosons $\phi$, $\chi\chi \to \phi\phi$, with $\phi$ subsequently decaying to the SM. Despite their simplicity, these models present an extraordinarily challenging scenario for detection, leading to the moniker "nightmare" DM. DM velocities even in galaxy clusters today are a tiny fraction of what they were at thermal freeze out. In the Milky Way, typical DM velocities are $v_{gal} \sim 10^{-3}c$, while at thermal freeze out $v_{fo} \sim 1/3$c. Thus the annihilation rates for $p$-wave DM in the Galactic halo today are suppressed by a factor of $\sim 10^{-5}$ relative to the expectation for $s$-wave DM, making astrophysical detection of $p$-wave DM annihilations largely out of reach: constraints from light element abundances, Cosmic Microwave Background (CMB) observations, radio data, and $\gamma$-ray Galactic diffuse emission are orders of magnitude away from sensitivity to thermal $p$-wave annihilations [226, 227, 228]. For secluded nightmare models, the lack of detectable signals in conventional indirect detection searches is especially concerning, as the coupling between $\phi$ and the SM will generically be parametrically small, easily placing both collider and direct detection signals out of reach [201] [1]. Given the

[1] In the limited regions of parameter space where nightmare DM interacts sufficiently strongly with itself to form bound states, the $s$-wave signals from bound state decay can provide an indirect detection signature in the CMB [229].

dismaying ease with which nightmare models evade all traditional searches for DM, it is of high interest to consider other avenues to discover or constrain $p$-wave DM.

Unique opportunities for detecting $p$-wave DM may be offered by the DM density spikes that can form around supermassive black holes (SMBHs). Depending on the formation history of the black hole (BH) and its astrophysical environment, such spikes can yield extraordinarily dense concentrations of DM, and thus bright, localized signals, particularly in models of annihilating DM [209, 230, 231, 232, 233]. Critically, the DM velocity dispersion increases inside the spike, $v^2(r) \propto M_{BH}/r$, with $r$ the distance from the BH, to support the power-law increase in density. In other words, supermassive black holes act as mild DM accelerators, opening a window onto the physics of thermal freeze out and thereby potentially enabling the observation of processes that were active in the early universe but are otherwise inaccessible in the present day [202, 234, 235, 236]. DM annihilation (or decay) within SMBH-induced density spikes would appear as a point source to $\gamma$-ray telescopes, with the main component of the $\gamma$-ray spectrum arising from DM annihilations. $p$-wave DM annihilation within such spikes can thus give rise to potentially observable kinematic features in the $\gamma$-ray energy spectrum with a point-source-like spatial morphology, even in the absence of a corresponding signal from the halo [202]. This probe of $p$-wave DM annihilation in the $\gamma$-ray spectrum offers a discovery tool for models of DM that could otherwise elude detection entirely.

With this motivation in mind, the $\gamma$-ray data set compiled by *Fermi*-LAT is of great interest [88]. The *Fermi*-LAT is one of the most sensitive instruments to DM with weak-scale mass and cross section annihilating into $\gamma$ rays. Analysis of the *Fermi*-LAT $\gamma$-

ray data can place strong limits on, or discover, DM annihilation with cross sections near the canonical thermal value into a wide variety of SM particles. However, most recent searches by the *Fermi*-LAT Collaboration, including both searches for a continuum excess and spectral features, have assumed $s$-wave annihilation processes [75, 237, 238], mainly because the velocity suppression makes searches for $p$-wave annihilation processes insensitive to thermal relic DM.

A handful of authors (e.g. [239]) have searched for velocity-dependent DM annihilation in dwarf galaxies, but as far as we are aware, a detailed study of velocity-dependent annihilation at the Galactic Center (GC) has not yet been undertaken. Meanwhile a growing body of work (for instance [211, 232, 234]) suggests that the GC with its SMBH Sgr $A^*$ may be the best location to search for $p$-wave DM annihilation.

In the *Fermi*-LAT energy spectrum, the spikes would contain sharp spectral features such as $\gamma$-ray lines [240] or boxes (a flat distribution of photon flux between two energy endpoints) [241], allowing such a spike signal to be distinguished from known astrophysical sources[2]. A search for sharp spectral features in a point-like source is distinct from the search for line emission in the Galactic halo performed in Ref. [237]. Basic searches for box-like spectral features at the GC have been performed previously [241], but generally assume a different phenomenology (i.e. a velocity-independent annihilation cross section, and therefore a different spatial morphology) than what is considered here.

In this paper, we consider the $\gamma$-ray emission from the GC, which is host to the

[2]The sharp spectral features may be subdominant

SMBH Sgr A$^*$. Specifically, we focus on the core of Sgr A$^*$, where the flux from $p$-wave DM annihilation is expected to come from, and search for both narrow line-like boxes and wide boxes. Because the $\gamma$-ray spectrum is a falling powerlaw, the sensitivity to wide boxes is driven almost entirely by the sharp feature provided by its upper endpoint. Therefore, results obtained for a particular wide box may be reliably applied to boxes of intermediate widths as well.

In Section 6.2, we describe the DM distribution in the GC and how it relates to searches for indirect signals of DM annihilation. In Section 6.3, we discuss the *Fermi*-LAT instrument, the method of modeling the GC as a $\gamma$-ray source, and the data set and background models used for the DM analysis. The analysis techniques and the resulting bounds are shown in Sections 6.4 and 6.5, and we conclude in Section 6.6.

## 6.2 Dark matter models

A black hole (BH) at the center of a DM halo contracts the matter within its zone of influence into a power-law overdensity or "spike", $\rho_{DM}(r) \propto r^{-\gamma_{sp}}$ [209, 242, 243, 244]. The steepness of this spike depends on the properties of the DM halo as well as the formation history of the BH, yielding power-laws as shallow as $\gamma_{sp} = 1/2$ in the case of BHs that are not at the dynamical center of their surrounding halo [243, 244], and as steep as $\gamma_{sp} = 2.75$ for BHs growing adiabatically at the center of an NFW-like halo [209]. Gravitational scattering from baryonic matter can be important in determining the steepness of the final spike if the stellar distribution within the gravitational zone of influence of the BH is sufficiently dense and cuspy, as may be the case for the SMBH at the center of the Milky Way[230, 245, 246]. In this case, the limiting power law for the DM spike is $\gamma_{sp} = 1.5$, attained when the system has reached equilibrium. If the system is still in the process of equilibrating, then non-equilibrium spikes, characterized by intermediate values of $\gamma_{sp}$, are possible. Meanwhile strong DM self-interactions would lead to yet other intermediate values of $\gamma_{sp}$ [247]. For the Milky Way's central SMBH, there are thus a wide range of possible density spikes, depending on the detailed history of the GC and the nature of DM.

The combination of the high DM densities and the increased DM velocities within a SMBH-induced density spike can make thermal $p$-wave DM annihilations observable around the Milky Way's SMBH across a wide range of assumptions for the DM distribution in the GC [202]. For $p-$wave DM, the point-like source from the BH density spike is the only observable cosmic-ray signal of DM annihilations; there is no corresponding detectable signal from the halo.

Especially in the absence of a crosscheck from a halo signal, to ascribe a DM origin to a point-like $\gamma$-ray source in the busy environment of the GC, it is critical to search for sharp kinematic features in the energy spectrum such as $\gamma$-ray lines and boxes. This section will firstly define a general, parametric model of DM spikes in the GC, and secondly describe a reference model of $p$-wave DM and its $\gamma$-ray signatures.

### 6.2.1 DM distribution in the GC

We adopt a fiducial model for the DM distribution in the GC following [202, 232]. We take the halo to be described by a generalized NFW halo, which in the inner Galaxy takes a power-law form, $\rho(r) = \rho(r_0)(r_0/r)^{\gamma_c}$. Typical values of the cusp exponent $\gamma_c$ predicted by DM-only simulations are in the range $0.9 \lesssim \gamma_c \lesssim 1.2$ [207, 208]. Larger values of $\gamma_c$ can arise through the adiabatic contraction of the central halo following the dissipative collapse of baryons into the disk [212, 248, 249], though such large values are somewhat disfavored by recent observations [250]. We treat $\gamma_c$ as a free parameter. We take the solar system to lie at $r_\odot = 8.46$ kpc from the GC [126], and the local density of DM to be $\rho_\odot = 0.3\,\mathrm{GeV/cm^3}$ [154]. Here and below, our adoption of specific values for galactic parameters should be viewed as a fiducial choice, in the same spirit as the adoption of specific fiducial halo models in more traditional searches for DM annihilation products in the halo.

The DM spike begins growing inside the region $r_b \approx 0.2 r_h$ (where $r_h = GM/v_0^2$ is the radius of gravitational influence of the black hole) [245, 251], and is well-described as a power law, $\rho_{sp}(r) = \rho_{sp}(r_b)(r_b/r)^{\gamma_{sp}}$. Here G and M are Newtonian gravitational constant and the black hole mass, respectively. As discussed above, different formation histories of the SMBH and the inner Galaxy yield a wide range of possible values for $\gamma_{sp}$, and we here consider $\gamma_{sp}$ to be a free parameter. The spike grows following this power law until it becomes dense enough that annihilations become important over the lifetime of the spike $\tau \approx 10^{10}$ years, $\rho_{ann} = m_\chi/(\langle\sigma v\rangle\tau)$. Within the corresponding radius, $r_{in}$, annihilations deplete the spike and limit the spike's growth to a very mild power law, $\rho_{in}(r) = \rho_{ann}(r_{in})(r_{in}/r)^{\gamma_{in}}$. The inner power law is $\gamma_{in} = 1/2$ for $s$-wave annihilations [210]. The increasing importance of $p$-wave annihilations with decreasing radius further flattens the inner power law relative to the $s$-wave case; we here adopt the numerical result $\gamma_{sp} = 0.34$ of Ref. [211]. Finally, the inner boundary of the spike is located at $r_{in} = 4GM$ [252].

The DM density in the spike and inner halo is thus modeled as [202, 211, 232],

$$\begin{aligned}
\rho(r) &= 0, \quad r < 4GM \quad \text{(capture region)}, \\
&= \frac{\rho_{\rm sp}(r)\rho_{\rm in}(t,r)}{\rho_{\rm sp}(r) + \rho_{\rm in}(t,r)}, \; 4GM < r < r_b \quad \text{(spike)}, \\
&= \rho_b (r_b/r)^{\gamma_c}, \qquad r_b < r < r_H \quad \text{(inner halo)}
\end{aligned} \tag{6.1}$$

We take $M = 4 \times 10^6 M_\odot$ [253, 254] and adopt as our reference inner halo dispersion $v_0 = 105 \pm 20$ km s$^{-1}$ [255], which together determine the radius $r_b$ at which the spike begins to grow. Our fiducial value of the halo dispersion velocity is about 5% higher than the value found in [255]; higher halo velocity dispersion leads to a smaller detectable flux [232], so this value is slightly conservative.

To support the power-law increase in density, the velocity dispersion inside the spike must also increase. We take the velocity dispersion as isotropic, and model it by matching a piece-wise continuous approximate solution of the Jeans equation within the spike onto a constant in the inner halo, giving

$$\begin{aligned} v^2(r) &= \frac{GM}{r}\frac{1}{1+\gamma_{in}}\left[1+\frac{r}{r_{\rm in}}\left(\frac{\gamma_{in}-\gamma_{sp}}{1+\gamma_{sp}}\right)\right], \\ &\qquad 4GM \le r < r_{\rm in} \quad \text{(inner spike)}, \\ &= \frac{GM}{r}\frac{1}{1+\gamma_{sp}}, \quad r_{\rm in} \le r < \frac{r_h}{1+\gamma_{sp}} \quad \text{(outer spike)}, \\ &= v_0^2 = \text{const}, \quad \frac{r_h}{1+\gamma_{sp}} \le r \quad \text{(cusp)}. \end{aligned} \tag{6.2}$$

The dominant contribution to the emission from DM annihilations within the spike occurs at $r_{in} \sim 10^{-3} - 10^{-5}$ pc for thermal dark matter. At this radius, the DM velocity is still non-relativistic, $v \sim 0.1c$.

The $\gamma$-ray flux per unit energy from (self-conjugate) DM annihilating within the spike is given by

$$\frac{d\Phi_\gamma}{dE_\gamma} = \frac{1}{4\pi R_\odot^2}\frac{1}{2m_\chi^2}\frac{dN_\gamma}{dE_\gamma}\int_{4GM}^{r_b} 4\pi r^2 dr\, \rho^2(r)\langle\sigma v(r)\rangle, \tag{6.3}$$

where $dN_\gamma/dE_\gamma$ is the $\gamma$-ray energy spectrum produced in a single annihilation. As the density profile of the spike $\rho(r)$ itself depends on the DM annihilation cross-section through $r_{in}$, the $\gamma$-ray flux from the spike does not depend linearly on the annihilation cross-section. For a $p$-wave spike, the flux depends on the annihilation cross-section as $\Phi_{sp} \propto (\langle\sigma v\rangle)^{(3-\gamma_{sp})/(1+\gamma_{sp})}$ [202]. Thus spike signals depend more weakly on the annihilation cross-section than do traditional halo searches. The results are moderately sensitive to other parameters in the model (the black hole mass and halo velocity distribution); for an estimate of the sensitivity, see Figure 2 of [232].

### 6.2.2 A reference $p$-wave DM model

As a reference model of thermal $p$-wave DM, we adopt here a specific realization of nightmare DM, the "Hidden Sector Axion Portal (HSAP)" model of [202]. In this model DM is a Majorana fermion $\chi$ that annihilates to pairs of pseudo-scalars $\phi$, which subsequently decay to SM gauge bosons. The Lagrangian describing the interactions of the DM and the pseudo-scalar is given by

$$\mathcal{L} = \bar{\chi}(i\gamma \cdot \partial)\chi - m_\chi \bar{\chi}\chi + \frac{1}{2}(\partial\phi)^2 - \frac{1}{2}m_\phi^2\phi^2 - iy\phi\,\bar{\chi}\gamma^5\chi, \tag{6.4}$$

where $m_\chi$, $m_\phi$ are the masses of $\chi$, $\phi$, and $y$ is the Yukawa coupling that will govern the annihilation cross-section. $CP$ conservation in this model ensures that the leading contribution to the DM annihilation cross section occurs in the $p$-wave. If the spectrum additionally contains a $CP$-even scalar $s$ with $m_S < 2m_\chi - m_\phi$, then DM annihilation can proceed through the $s$-wave $\chi\chi \to s\phi$ channel [241, 256], but $s$ may easily be too heavy to participate in DM annihilation, or indeed entirely absent. In this case $CP$ forbids the $s$-wave contribution.

We use this HSAP model to determine the annihilation cross-section $\langle\sigma v\rangle_{thermal}$ that yields the observed DM relic abundance as a function of $m_\chi$ and $\zeta \equiv m_\phi^2/m_\chi^2$. In terms of the Yukawa coupling $y$ between $\chi$ and $\phi$, the DM annihilation cross-section is

$$\langle\sigma v\rangle = \langle v^2\rangle \frac{y^4}{24\pi m_\chi^2}\sqrt{1-\zeta}\,\frac{(1-\zeta)^2}{(2-\zeta)^4} \tag{6.5}$$

in the non-relativistic limit [3]. The value of $y^4$ needed to obtain the observed DM relic abundance is shown in Fig. 6.1.

[3] For $\zeta \gtrsim 1 - \langle v^2\rangle/8$, the velocity dependence in the phase space factor $\sqrt{1-\zeta+\mathcal{O}(v^2)}$ in Eq. 6.5 must be retained. For spikes around the Milky Way's SMBH, $\langle v^2(r_{in})\rangle \sim 0.01$, and thus the DM

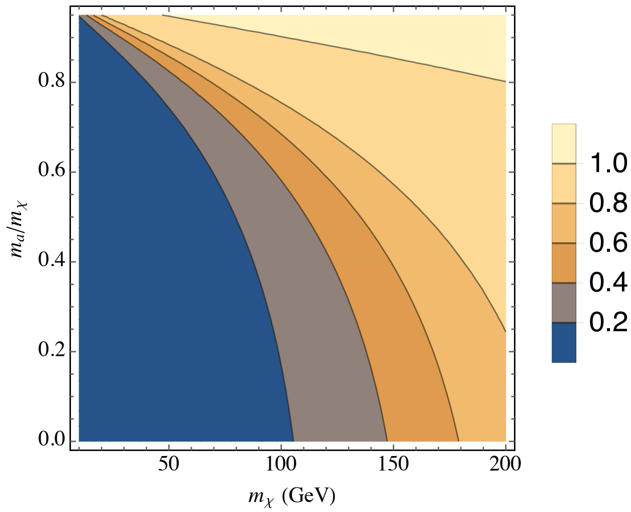


Figure 6.1: Value (represented by the color map) of the coupling $y^4$ required to obtain the observed DM abundance in the HSAP model (Eq. 6.5), as a function of $m_\chi$ and $\zeta = (m_a/m_\chi)^2$. Results in this plot are obtained using an approximate analytic solution to the Boltzmann equation [50] and are accurate to $\lesssim 10\%$; for calculations elsewhere in this paper the Boltzmann equation is solved exactly.

The analogue of the "smoking gun" DM line in this nightmare model is a DM *box*, i.e., a constant photon flux within the energy range $\left(1 - \sqrt{1 - m_\phi^2/m_\chi^2},\ 1 + \sqrt{1 - m_\phi^2/m_\chi^2}\right) \times m_\chi/2$ [241]. This feature is the result of the decay $\phi \to \gamma\gamma$, boosted in the Galactic rest frame according to the kinematics of the annihilation. Sufficiently narrow boxes appear line-like, while for wide boxes, the upper edge provides a sharp spectral feature that can allow the box to be cleanly identified above falling continuum backgrounds. As the dominant contribution to the DM annihilation signal inside the spike comes from regions where the DM is still highly

annihilation cross-section is still consistently $\propto \langle v^2 \rangle$ even for $\zeta = 0.99$. However for $\zeta \gtrsim 0.96$ the velocity dependence in the phase space factor is important for the larger velocity dispersions realized during thermal freezeout, and is retained in our full calculations, where we implement an exact thermal average in a numerical solution of the Boltzmann equation.

non-relativistic, kinematic broadening of the box feature is negligible in comparison to the *Fermi*-LAT energy resolution.

The branching fraction for the decay $\phi \to \gamma\gamma$ controls the normalization of the box signature and depends on the couplings of $\phi$ with the SM. If $\phi$ couples to the SM through axion-like couplings to electroweak gauge bosons, then its branching ratio to $\gamma\gamma$ (and, if kinematically allowed, $\gamma Z$) is $\mathcal{O}(1)$, and the $\gamma$-ray box is the leading signature of DM annihilation. In other models, for instance where $\phi$ decays to the SM through a mixing with the Higgs, the $\gamma\gamma$ branching ratio is suppressed, $\sim 10^{-2} - 10^{-3}$, and, while the box feature is still present, the $\gamma$-ray continuum emission arising from other $\phi$ decay modes will typically yield stronger constraints [202]. For simplicity, in this work we take the branching ratio $Br(\phi \to \gamma\gamma) = 1$, i.e., all of the annihilation flux appears in a $\gamma$-ray box.

Our implementation of the HSAP model should be understood as a convenient reference model in which one may interpret the results of a search for $\gamma$-ray boxes. As noted above, gauge invariance generally requires $\phi$ to also decay to $Z\gamma$ and $ZZ$ final states when these modes are kinematically accessible, which reduces the $\gamma\gamma$ branching ratio while adding new box and continuum contributions to the $\gamma$-ray energy spectrum [257, 258, 259, 260, 261]. We therefore caution the reader to interpret the results carefully above $m_Z$, as we only consider the case $Br(\phi \to \gamma\gamma) = 1$. Moreover, if $m_\chi > \frac{3}{2} m_\phi$, DM annihilations in the spike are actually dominated by the higher-order $s$-wave process $\chi\chi \to 3\phi$. Thus the widest box that is realized by the hidden sector axion portal model, considered literally, is realized for $\zeta = 4/9$. We emphasize that the experimental sensitivity to wide boxes is dominated by the upper end point, and thus limits on a wide box of a given $\zeta$ can reliably be re-interpreted to limit a wide box with different $\zeta$.

Meanwhile, once the width of the narrow box signal becomes smaller than the experimental resolution, the signal becomes line-like. While the search presented here is not optimized for line signals, a narrow box search will have sensitivity to $\gamma$-ray lines as well. Such $\gamma$-ray lines are predicted by models of $p$-wave DM where DM annihilates directly to SM final states, such as Higgs portal DM [222, 223]. However in most such models, direct annihilations into diphotons are highly suppressed, and for Higgs portal DM occur in fewer than $\lesssim 10^{-3}$ of events. For models where the continuum $\gamma$-ray signal dominates to this degree, requiring that DM annihilations within any SMBH density spike not outshine the observed point sources near the GC will typically lead to a more restrictive constraint than a line or box search [202].

## 6.3 Fermi-LAT observations of the Galactic center

*Fermi*-LAT is an all-sky pair-conversion telescope which has been successfully observing the $\gamma$-ray sky between a few tens of MeV to more than a TeV for ten years. Incoming $\gamma$ rays pass through an anti-coincidence detector and convert in a tracker to $e^+/e^-$ pairs. Energy is deposited by the $e^+/e^-$ pairs in a calorimeter. The charged particle direction is reconstructed using the information in the tracker, and the energy is estimated from depositions in the calorimeter. Detailed descriptions of the *Fermi*-LAT and its performance can be found in dedicated papers [88, 102]. In the data selection for the present work, *Fermi*-LAT has an integrated exposure of approximately $4.5 \times 10^{11}$ $\text{cm}^2\text{s}$ in the direction of Sgr A*.

### 6.3.1 Data Selection

For this analysis, we used nine years of *Fermi*-LAT data (2008 August 4 to 2018 July 26) selecting `Pass 8` SOURCE-class events in the energy range from 6 GeV to 800 GeV, binned in 50 logarithmically-spaced energy bins and 0.04° angular pixelization. The energy range was chosen to avoid the well-known [e.g. 123] complexities of modeling the GC at energies of a few GeV. In addition, the *Fermi*-LAT point-spread function (PSF) improves by nearly an order of magnitude between 1 GeV and 10 GeV, which improves its sensitivity to a signal that is localized as a point-like source. Our analysis considers $\gamma$-ray boxes with upper edges above 10 GeV; we include data between 6 and 10 GeV to avoid possible edge effects.

Our region of interest (ROI) was $2^\circ \times 2^\circ$ and centered at Sgr A*. The small ROI was chosen for two reasons: a) our putative DM signal is a point source spatially coincident with Sgr A*, and the *Fermi* 95% containment radius at 10 GeV is less than 1°, so our ROI should contain virtually all of the signal, and b) our analysis relies mostly on searching for sharp spectral features, so contamination of unmodeled nearby point sources was not a particular concern. We found the farthest point source from Sgr A* in our ROI, 3FHL J1747.2-2959, had negligible correlation with the parameters of the GC source. In any case, the resulting model showed no indications that our ROI had any appreciable contamination from sources beyond 1° from Sgr A*.

We modeled the performance of the *Fermi*-LAT using the P8R2_SOURCE_V6 Instrument Response Functions (IRFs). The data processing and exposure calculations were performed using the *Fermi* Science Tools version 11r5p3[4]. A summary of the parameters of our data selection is available in Table 6.1, and a counts map of the data is shown in the left panel of Figure 6.2.

[4]http://fermi.gsfc.nasa.gov/ssc/data/analysis/software

| Selection | Criteria |
|---|---|
| Mission Elapsed Time (s)[5] | 239557417 to 554321025 |
| Instrument Response Functions | P8R2_SOURCE_V6 |
| Energy Range (GeV) | 6-800 |
| Fit Region | $2^\circ \times 2^\circ$, centered on (RA, DEC)=(266.417, -29.0079) |
| Zenith Range | $\theta_z < 100^\circ$ |
| Data Quality Cut with the *gtmktime* Science Tool[6] | Yes |

Table 6.1: Data selection used by this paper's analysis

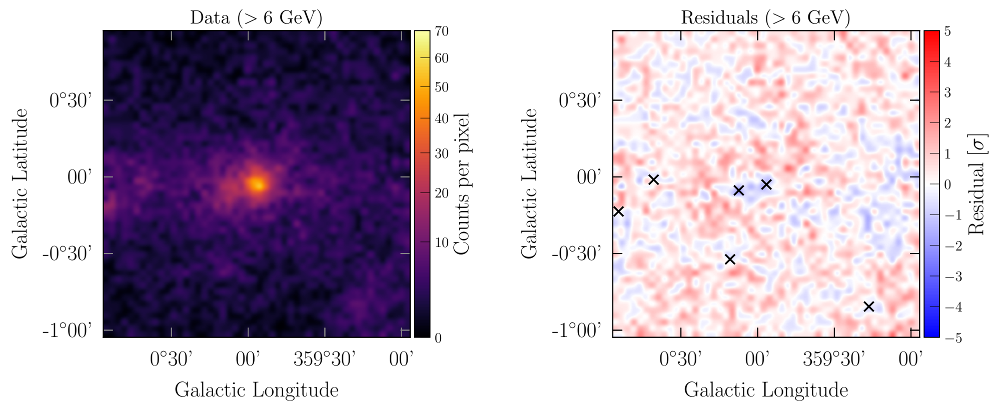


Figure 6.2: *Left panel:* Total photon counts in the ROI used in the analysis. The GC source is prominently seen near the center of the image, while the Galactic diffuse emission is responsible for the majority of the photons outside the GC. *Right panel:* Residuals (data-model) in units of $\sigma$ after fitting with `gtlike` (see Section 6.3.2). The location of each 3FHL point source in the model is marked with a black (X). No significant excesses or deficits are observed in the data. In both maps, the pixel size is 0.04° and a Gaussian smoothing (width of 0.04°) has been applied.

### 6.3.2 Modeling the GC

In order to search for a DM signal via the maximum-likelihood analysis described next, in Section 6.4, we required a model of the ROI. Our model was built from diffuse components and objects listed in the Third Catalog of Hard *Fermi*-LAT Sources (3FHL) [124].

#### 6.3.2.1 Diffuse Components and Extended Sources

The GC is the most complicated region of the $\gamma$-ray sky, and as a result the parameters of the point source associated with Sgr A$^*$ are dependent on the model of Galactic diffuse emission. Although custom interstellar emission models (IEM) have been successfully used to model the GC in past works [123], generating a similar custom IEM with the data reconstruction used here was deemed to be outside the scope of this paper, for which we needed only an empirical model against which we can test our DM hypothesis.

The diffuse components used in this analysis were the standard Pass 8 models taken from the Fermi Science Support Center[7]. After an initial fit to the data we found that the contribution by the isotropic component of our model was negligible; we decided not to include an isotropic component in the final model for this reason. We do not expect its omission to have an impact on the results.

The 3FHL catalog comprises sources detected at energies above 10 GeV over the first 7 years of *Fermi*-LAT data, and contains 1556 sources. Six of these sources fall within our ROI, and all have spectra well-described by a power law. Furthermore, none of the sources in the ROI were found to be extended in the 3FHL catalog. A summary of all the sources used in the model is shown in Table 6.2, and the residuals of the data after optimizing the model are shown in the right panel of Figure 6.2. With six point sources and one diffuse component, and two free parameters for each source (the prefactor and spectral index of the power-law), the background-only model contained a total of 14 free parameters.

As a check of our systematic uncertainty, we also performed the following analysis using a separate dataset and model covering 4 years of data with Pass 7 data reconstruction. The model of the ROI contained a different set of point sources (from

[7] The diffuse background models are available at: `http://fermi.gsfc.nasa.gov/ssc/data/access/lat/BackgroundModels.html` as `is_P8R2_SOURCE_V6_v06.txt` and `gll_iem_v06.fits`.

| 3FHL Source Description | $N_\gamma$ | RA | DEC |
|---|---|---|---|
| Galactic diffuse emission | 4397 | - | - |
| J1745.6-2900 | 1253 | 266.42 | -29.01 |
| J1746.2-2852 | 510 | 266.56 | -28.88 |
| J1747.2-2959 | 172 | 266.80 | -30.00 |
| J1747.2-2822 | 137 | 266.82 | -28.37 |
| J1748.1-2903 | 96 | 267.04 | -29.06 |
| J1748.6-2816 | 126 | 267.16 | -28.28 |

Table 6.2: List of sources used in modeling the ROI. $N_\gamma$ is the integral number of photons expected from the source, after optimization by `gtlike`.

the 3FGL catalog [120]), and diffuse models were taken from the custom IEM of [123]. The resulting flux upper limits were found to be consistent with the main analysis presented below; for simplicity we present only our standard analysis.

## 6.4 Analysis

### 6.4.1 Fitting Method

As discussed in Section 6.2, the phenomenology of our reference model p-wave DM signal is that of a point source located at the location of Sgr A$^*$, with a photon flux that is flat between two endpoints (a 'box' shape). For this analysis, we considered two representative versions of the box: the 'wide' box has a value of $\zeta = 0.44$, while the 'narrow' box has a value of $\zeta = 0.9999$. Implications from the two types of searches for mass splittings in intermediate cases are discussed in Section 6.6.

We searched for $\gamma$-ray boxes which had an upper-edge energy equal to the boundaries of the energy bins between 10 and 658 GeV in our data selection, corresponding to 42 different DM hypotheses. In order to prevent potential edge effects from impacting the results, boxes with upper edges outside of this range were not considered.

The likelihood $\mathcal{L}(n, \theta)$ of a particular model is given by:

$$\mathcal{L}(n, \theta) = \prod_{i=0}^{N} \frac{\mu_i^{n_i}}{n_i!} e^{-\mu_i} \tag{6.6}$$

where the index $i$ runs over the angular and energy bins, and $\mu_i$ and $n_i$ are the predicted and actual photons, repsectively, in bin $i$. We varied the model parameters $\theta$ until the likelihood is maximized; in practice we used the logarithm of the likelihood. The likelihood computation and maximization was performed by the *Fermi* Science Tool gtlike, which in turn used the MINUIT [262] optimization routine.

The significance of each DM hypothesis was evaluated using the test statistic (TS) defined as:

$$\mathrm{TS} = 2 \ln \frac{\mathcal{L}(\mu, \theta | \mathcal{D})}{\mathcal{L}_{\mathrm{null}}(\theta | \mathcal{D})} \tag{6.7}$$

Where $\mu$ is the signal strength, $\theta$ is the array of parameters describing the DM hypothesis (in this case, the energy and width of the $\gamma$-ray box, and $\mathcal{D}$ represents the binned data. $\mathcal{L}_{\mathrm{null}}$ is the value of the likelihood in the absence of any signal. The likelihood values $\mathcal{L}$ are computed from Equation 6.6.

The TS value was then used to calculate a level of significance $Z$ via:

$$Z = \Phi^{-1}\left(1 - \int_{\text{TS}}^{\infty} \chi^2(x,k)dx\right) \tag{6.8}$$

Where $\Phi^{-1}$ is the inverse quantile function; the integral in this expression is the $p$-value. Simulations (described below) confirmed that the TS values were distributed roughly following a $\chi^2$ distribution with 1 degree of freedom (the total flux contained in the 'box' signal)—see the left panel of Figure 6.3. As the number of trials per bin decreases, the $\chi^2$ distribution moderately over-predicts the number of high TS trials observed in simulated data. An example DM signal with $\zeta = 0.44$ (spatially integrated over the ROI), along with the background, is shown in the left panel of Figure 6.4.

The procedure for finding the TS of a given DM hypothesis and upper limit on the total flux of a $\gamma$-ray box with an upper edge at a particular bin energy was as follows:

1. The parameters of the model described in Section 6.3.2 allowed to vary to maximize the likelihood function $\mathcal{L}$, giving the null likelihood. This step was performed once for each dataset under investigation (either the true data or the Monte Carlo simulations described below).

2. The expected spectrum of the DM signal is calculated by convolving a ideal box spectrum with a Gaussian distribution representing with the *Fermi*-LAT energy resolution, which is between 5% and 10% in the energy range considered.

3. A point-source with the convolved DM spectrum is added to the model at the location of Sgr A$^*$, with a single overall normalization parameter $N$.

4. All parameters in the model except for the normalization of the central GC source are fixed. A study of the correlation coefficients (see Section 6.4.2) showed that the signal was correlated with this source (especially of DM hypotheses with upper edge below 100 GeV) , but had negligible correlation with other parameters in the model. Fixing the other parameters also had the benefit of decreasing the computation time and preventing numerical instabilities when fitting a system with a large number of degrees of freedom.

5. The normalization $N$ of the DM source is increased from a value of 0 until the TS exceeds 2.77, which corresponds to the 95% confidence upper limit on $N$, or a $Z$ value of approximately 2. The value of this TS was computed empirically from the results of the Monte Carlo simulations (see Section 6.4.3. This value is approximately the value of the critical $\chi^2$ of 2.71 for a $p$-value of 0.1 with 1 degree of freedom, which is consistent with a one-sided upper limit at 95% confidence. The complete likelihood profiles for each DM hypothesis are also stored.

### 6.4.2 Correlations Between Background and Signal Components

In order to understand the relationship between a potential signal and the background sources, we calculated the correlation coefficients between the signal source and the GC source. As expected, both $\zeta = 0.9999$ and $\zeta = 0.44$ hypotheses are negatively correlated with the normalization of the GC background source. We found that the signal became less correlated as the right edge of the box increases in energy, since the likelihood fit is strongly driven by the higher statistics at low energy. We also found that the $\zeta = 0.44$ hypothesis had a stronger correlation to the background when compared to the $\zeta = 0.9999$ case, which is expected because the $\zeta = 0.44$ signal contributes over a broader energy range. A plot of the correlation coefficients in both cases as a function of the energy of the right edge of the box is shown in the right panel of Figure 6.3 below.

We investigated further the degeneracy between the signal and background by recomputing the upper limit on the signal flux with the parameters of all background sources fixed at the value obtained from step 1. We cannot say *a priori* that the data does not contain any signal, so the solid curves in Figure 6.5 is the main, conservative result. However, if we were to assume that there was no observed signal, then the dashed curve in Figure 6.5 is the most optimistic limit attainable.

The prefactor and index describing the power-law spectral shape of the GC source were found to be almost perfectly anticorrelated. We found that the correlation coefficients of the signal to the parameters of other sources in the model were negligible.

### 6.4.3 Monte Carlo Simulations

We performed a Monte Carlo study in order to understand the impact that statistical fluctuations have on the analysis, and to evaluate the distribution of TS values of the signal. Each instance of the Monte Carlo began by optimizing the background-only model, and generating Poissonian fluctuations around the model. We then used the Poisson data as the input to the protocol defined in Section 6.4.1, and stored the likelihood profiles for each DM hypothesis. Only MC instances in which the fitting

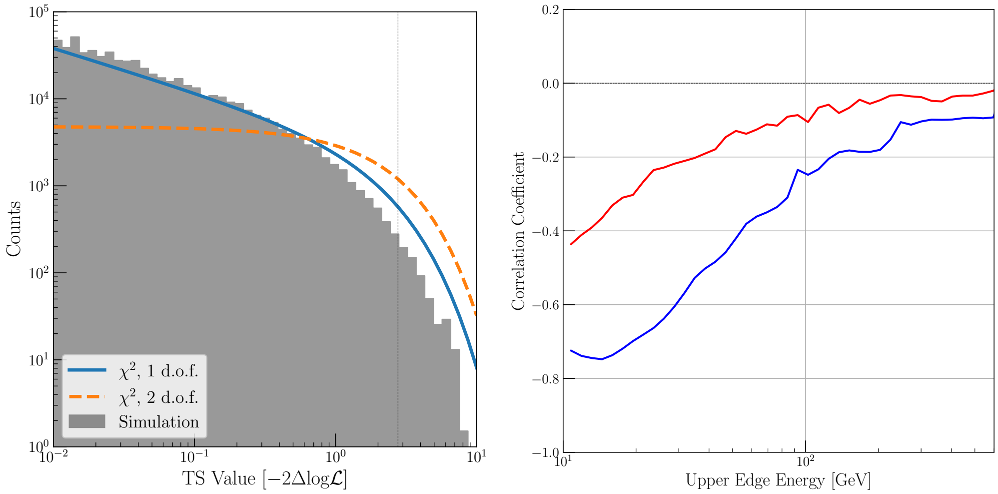


Figure 6.3: *Left Panel*: Histogram of TS values for all DM signal hypotheses from the Monte Carlo study for a $\zeta = 0.44$ signal. The shape of the TS distribution is well-described by a $\chi^2$ distribution with only one degree of freedom, although the $\chi^2$ distribution slightly overpredicts the Monte Carlo distribution at high TS and underpredicts at low TS. The critical value of 2.77, is shown as a vertical dashed line. *Right Panel*: Correlation coefficients ($\zeta = 0.44$ in solid blue and $\zeta = 0.9999$ in dashed red) between the total flux of the DM signal hypotheses and the normalization $N$ of the GC source (modeled as a power law, i.e. $\frac{dN}{dE} = Ne^{-\alpha E}$. We evaluate the correlation as a function of the upper edge of the DM signal box, and find that the correlation is negligible for high-energy boxes but is becomes significant at lower energies because of the increased statistics in the data at lower energies. Because the two sources are spatially coincident, the sources are expected to be anticorrelated.

procedure converged with no errors were used in performing the calculations. Because Step 1 above fits the parameters of the background model, this technique probes the effects of statistical uncertainty on both the signal and the background.

From the sample of MC instances, we found the distribution of TS values that corresponded to the best-fit fluxes of the DM signal. The distribution is approximately distributed as a $\chi^2$ with one degree of freedom, which is consistent with the result expected from Wilk's theorem (see the left panel of Figure 6.3). The critical TS of 2.77

is shown in the figure as a dashed vertical line.

We performed $O(10^3)$ simulations, and calculated the upper limit curves from each instance. The family of curves was used to generate 68% and 95% containment bands for the cases of $\zeta = 0.44$ and $\zeta = 0.9999$. The results are displayed in Figure 6.5.

### 6.4.4 Reconstruction of Injected Signal

To confirm that the upper limit calculation was sensitive to the presence of a DM signal, and to understand how a signal would appear in our analysis, we injected a DM signal into the data and repeated the analysis procedure from Section 6.4.1. The injected DM signal for this test was defined to have $\zeta = 0.44$ and a total flux of $1.5{\times}10^{-10}$ph cm$^{-2}$s$^{-1}$, with an upper energy endpoint of 100 GeV. At 100 GeV, the ratio of the injected signal flux to the total flux in the ROI was about 30%. We performed the same Monte Carlo study on the injected-signal dataset to produce containment bands for the limit.

The results of the analysis are in good agreement with the known injected signal. The best-fit DM hypothesis was found to have an upper edge energy of 102 GeV, and the reconstructed flux of the signal was $1.61 \times 10^{-10}$ ph cm$^{-2}$s$^{-1}$. The upper limit curve was found to contain a prominent bump near 100 GeV which noticeably exceeded the 68% and 95% containment bands from the Monte Carlo study, as seen in Figure 6.4.

We concluded that the analysis procedure defined in Section 6.4.1 is sensitive to the presence of a realistic DM signal, and can accurately reconstruct its parameters.

For illustration, the spectrum of a best-fit box with total flux $3.0 \times 10^{-10}$ph cm$^{-2}$s$^{-1}$ (double that of the injected box test) is shown in the left panel of Figure 6.4.

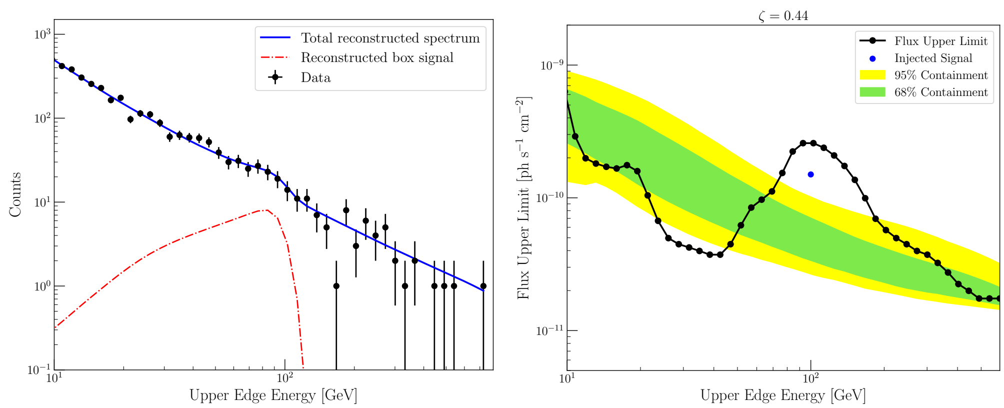


Figure 6.4: *Left Panel*: Energy spectrum of the data + injected signal. The injected 'box' DM signal appears in the data as a small bump near its upper endpoint. *Right Panel*: The DM signal upper limit (in black) in the presence of an injected box with upper endpoint 100 GeV and total flux $1.5 \times 10^{-11}$ ph cm$^{-2}$s$^{-1}$. The blue dot shows the position of the injected signal. The 68% and 95% containment bands are constructed from performing the analysis on Poisson-fluctuated datasets about the best-fit background model. Our injected DM signal is not excluded by the analysis.

## 6.5 Results

No significant signal from a p-wave DM signal was seen in either the case of the wide or narrow box. The flux upper limits are shown in Figure 6.5 for both the wide box (left panel) and the narrow box (right panel) scenarios. The strongest signal came in the case of $\zeta = 0.44$ at an upper-edge energy 125 GeV; the empirical local significance (found from comparison to the MC TS distribution of Figure 6.3) was found to be $1.83\sigma$. For the case of $\zeta = 0.9999$, the strongest signal came from a box with an upper-edge energy of 84 GeV; the local significance was $1.7\sigma$. These do not take into account trials factors, so their global significance is reduced further.

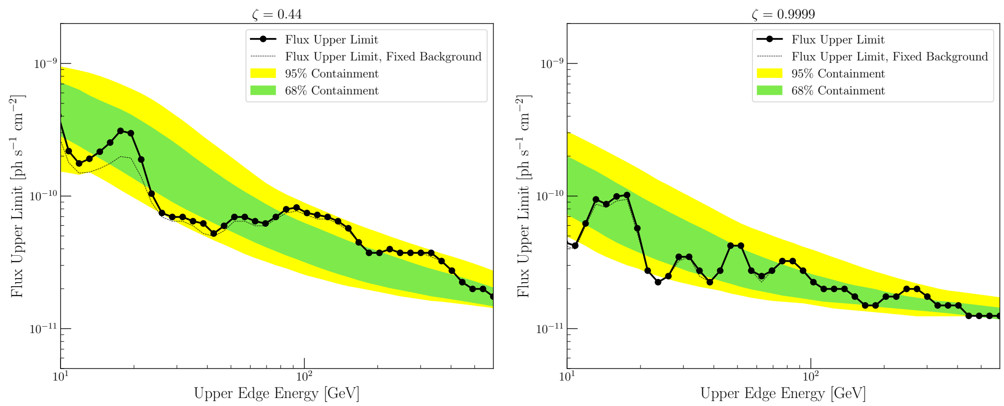


Figure 6.5: *Left Panel:* 95% confidence flux upper limit on a $\gamma$-ray box point source at the GC with $\zeta = 0.44$. The thin dashed line is the corresponding limit when all background sources are fixed. As expected, fixing the background sources improves the limit at lower energies, though only by a factor of 2 at the most. *Right Panel:* The same plot, but for the case of $\zeta = 0.9999$. In both figures, the 68% and 95% containment bands come from a Monte Carlo simulation of the data described in Section 6.4.3.

The predicted flux from $p$-wave DM annihilation depends on the DM mass $m_{DM}$ as well as on the power laws of the DM halo ($\gamma_c$) and spike ($\gamma_{sp}$) in our fiducial model. In Figure 6.6 we fix the DM mass, and show how the upper limits on narrow and wide boxes constrain the allowed DM distribution in the GC. We can observe in particular that adiabatic spikes are excluded for even very shallow cusps $\gamma_c = 0.8$. In this parameter space, nightmare DM models yielding narrow boxes are less constrained than DM models yielding wide boxes, despite the stronger flux limits; this occurs because the limited phase space available for the narrow box annihilation process further suppresses the annihilation.

In Figure 6.7 we consider fixed sample choices of $\gamma_c$ and $\gamma_{sp}$ and show the

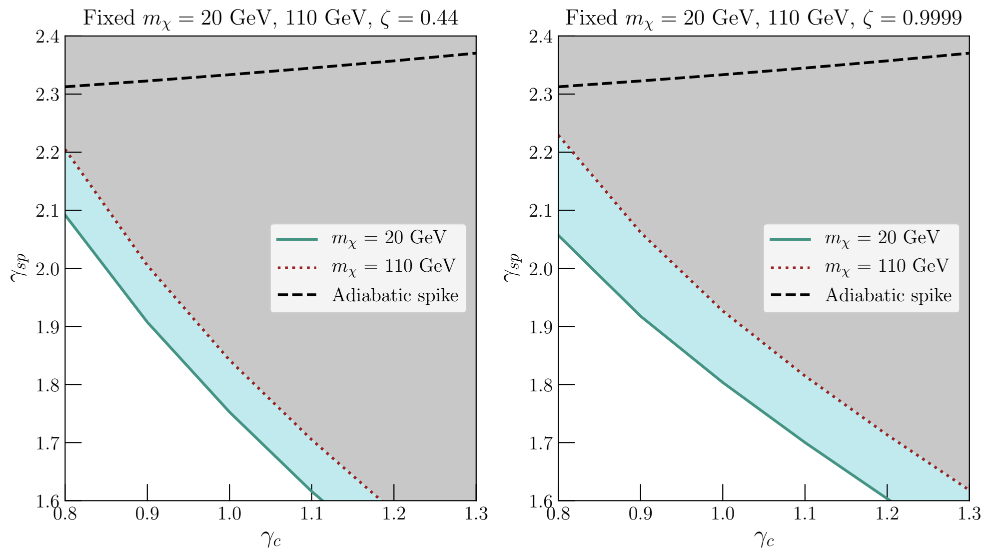


Figure 6.6: Shaded regions above each curve show the excluded DM distributions in the GC with thermal relic $p$-wave DM in the hidden sector axion portal model. Two representative choices of DM mass $m_\chi = 20$ GeV, 110 GeV for narrow boxes (left, $\zeta = 0.99$) and wide boxes (right, $\zeta = 0.44$) are shown. The limits shown here and in Figure 6.7 rely on the assumptions made in Section 6.2 about the mass of Sgr A*, the halo velocity dispersion, and the $\gamma\gamma$ branching ratio.

resulting limits on our reference hidden sector axion portal $p$-wave DM model as a function of DM mass. For clarity we plot the ratio of the excluded cross-section $\langle\sigma v\rangle$ to the value of the cross-section that yields the correct relic abundance, $\langle\sigma v\rangle_{\rm thermal}$. We comment that exclusions for the narrow box scenario in this reference model should not be considered literally at high masses as the model becomes non-perturbative above $m_\chi \sim 300$ GeV. The need for such large couplings arises to compensate for the phase space suppression that follows when $m_\chi \approx m_\phi$, and no such issue arises in the wide box scenario.

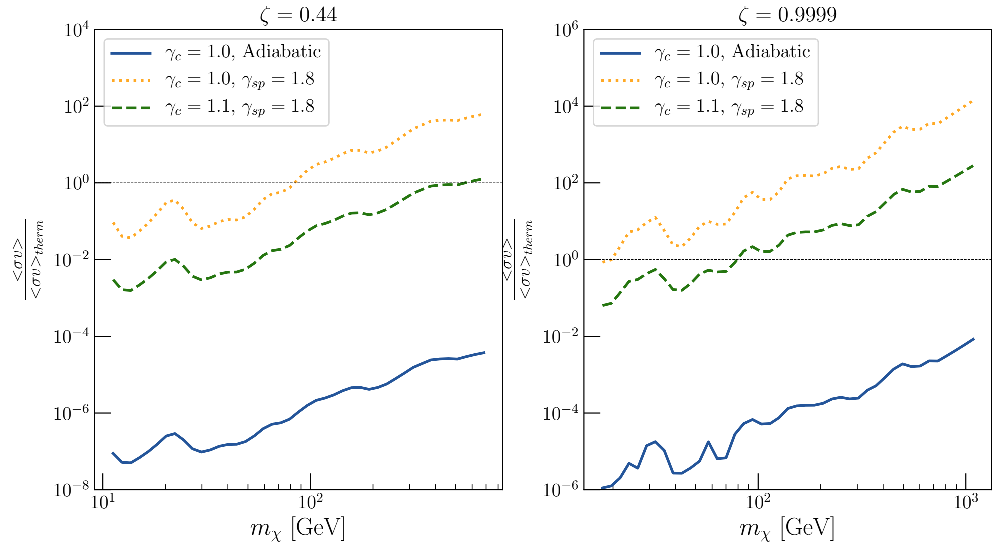


Figure 6.7: 95% confidence upper limits on DM annihilation cross-section as a function of DM mass for fixed values of $\gamma_c$, $\gamma_{sp}$. For clarity we plot the velocity-independent ratio of the excluded cross-section to the value that yields the correct relic abundance. From top to bottom, the three curves correspond to $\gamma_c = 1.0, \gamma_{sp} = 1.8$ (orange); $\gamma_c = 1.1, \gamma_{sp} = 1.8$ (green); and $\gamma_c = 1, \gamma_{sp} = 2.33$ (adiabatic spike, blue).

## 6.6 Discussion and Conclusions

In this paper we present the results of a search for the $\gamma$-ray signature of DM annihilating through a $p$-wave channel. Although most indirect detection searches to date have focused on $s$-wave annihilation, it is necessary to consider other paradigms in which this channel is suppressed. As many models of thermal DM have parametrically suppressed couplings to SM particles, and thus no accessible direct detection or collider signals, it is critical to perform astrophysical searches for such models. *Fermi*-LAT is an ideally suited instrument to perform this search due to its large exposure in the direction of the Galactic center and good energy resolution. We searched the *Fermi*-LAT data for the $\gamma$-ray signature of $p$-wave annihilating particle DM at the Galactic center in the energy range 6-800 GeV. Two spectral models (corresponding to the upper and lower extrema of mediator masses) were tested by comparing the maximum likelihood $\mathcal{L}$ in the presence and absence of a signal. We found no evidence of a DM signal, and placed an upper limit on the total $\gamma$-ray flux from $p$-wave annihilation at the center of the Milky Way.

The flux limits presented here are independent of the parameters of the DM spike (i.e. the $J$-factor). Interpreting these limits further requires making assumptions about the mass of Sgr A*, the halo velocity dispersion, and the branching ratio $Br(\phi \to \gamma\gamma)$ as described Section 6.2, If one assumes a thermal-relic cross section for the annihilation, they can be used to constrain these parameters. Alternatively, one can use a fixed model of the DM spike to put limits on the annihilation cross section; we found that the annihilation cross section can be constrained to be below the canonical thermal relic cross section given some models of the spike parameters $\gamma_c$ and $\gamma_{sp}$. Given the two models of mediator masses considered here, it is also possible to use the results in the context of other models of $p$-wave annihilation with intermediate mediator masses.

# Chapter 7

# Conclusions

The identity of dark matter continues to elude physicists, and remains one of the most vexing problems facing the community today. Although well-motivated models (such as WIMPs) have been developed, no definitive signal of DM interaction with the Standard Model has been seen in any direct, indirect, or production channels at the time of publication. Nevertheless, evidence and constraints from experiment remain invaluable in guiding DM theory.

Because the most straightforward experiments have failed to identify the DM, novel methods are of great value in experimental DM searches. Ideally, searches for particle DM would be sensitive even towards "sterile" DM—that is, DM that is decoupled from all other fields in the SM. An evaporating black hole is a unique laboratory for probing this type of DM, as all species of particles, regardless of their interactions, should be emitted as Hawking radiation. The observation of black hole evaporation would therefore be a stunning discovery, not only for the confirmation of Hawking radiation (one of the most important discoveries of twentieth-century physics), but because it would open up a new window into new high-energy processes. Because Hawking radiation is virtually undetectable for stellar-mass black holes, an evaporating black hole today would almost certainly be primordial, and therefore a detection could also yield clues about primordial density fluctuations. A search for such black holes was carried out in Chapter 4, with no PBH candidates detected, and a rigorous upper limit on their local density was placed.

As *Fermi*-LAT collects more data and more accurate background models are built, its sensitivity to evaporating PBHs will increase. A forthcoming general purpose *Fermi*-LAT catalog covering 8 years of data (the 4FGL[1]) with Pass 8 reconstruction could be used in place of the 3FGL in an analysis similar to the one presented in Chapter 4. With the new dataset, the proper motion algorithm introduced in Chapter 4 would likely need modifications, especially to account more robustly for PBHs that evaporate within the observation time. With improvements to the data and algorithms, it is not unreasonable to estimate that the constraints on the local PBH evaporation could be reduced by an order of magnitude. Future $\gamma$-ray instruments (like the proposed AMEGO[2] or e-ASTROGAM [263] satellites) may also prove useful in the search for Hawking radiation, as they will be most sensitive in the energy range for which the PBH $\gamma$-ray flux is highest.

In the absence of such a model-independent way of detecting particle DM, it is

[1]At the time of publication, the 4FGL had not been released, although there is a candidate source list available at `https://fermi.gsfc.nasa.gov/ssc/data/access/lat/fl8y/`

[2]see `https://pcos.gsfc.nasa.gov/physpag/probe/AMEGO_probe.pdf`

important to reconsider the assumptions of previous DM searches for DM models that may yet prove to be correct. One of the most basic assumptions in the indirect WIMP detection paradigm is that the WIMP annihilation cross-section is velocity-independent, which implies best locations to search are those that are richest in DM density. However, as pointed out in Chapter 5, it is quite natural to model WIMPs with an annihilation cross-section that depends on the square of the speed of the incoming WIMP particles. In this case, the brightest annihilation signal will come from locations that are high in both DM density and velocity dispersion, such as the neighborhood of a supermassive black hole.

A search for the $\gamma$-ray signature of annihilating WIMPs near the supermassive black hole at Sgr A* was carried out in Chapter 6. An empirical model of the $\gamma$-ray sky at energies above 6 GeV was built from the *Fermi*-LAT 3FHL catalog, and was found to fit the data well. No statistically significant excess of $\gamma$-rays near the Galactic center was seen for two representative DM models, and the DM annihilation cross-section was strongly constrained for several models of the DM spike around Sgr $A^*$.

Due to the presence of numerous $\gamma$-ray sources at the Galactic center that act as backgrounds, it is interesting to consider whether stellar-mass black holes in lower-background regions might also be suitable targets for such a search. The nearest known black hole to Earth, in the binary X-ray transient A0620-00, lies at a distance of approximately 1 kpc, with a mass of 6.6 $M_{\odot}$ [264]. Since the volume of influence of black hole is proportional to the cube of the black hole mass, an upper bound on the WIMP annihilation flux $\Phi$ from the black hole in A0620-00 can be estimated to be far smaller than the flux from Sgr A*: $\frac{\Phi}{\Phi_{\text{Sgr A*}}} \sim \left(\frac{M}{M_{\text{Sgr A*}}}\right)^3 \left(\frac{d_{\text{Sgr A*}}}{d}\right)^2 \approx (10^{-6})^3(8)^2 = 6.4\times10^{-17}$, where $d$ is the distance to the black hole. Moreover, the DM density in the neighborhood of A0620-00 is lower than at the Galactic center, so this value is somewhat conservative.

More interesting targets may be other SMBHs that are otherwise $\gamma$-ray quiet, such as M87, M81, or perhaps an ensemble of nearby AGNs. It is conceivable that the combination of reduced backgrounds and larger annihilation volumes may be sufficient to overcome the inverse square penalty for increased distance, potentially leading to even stronger constraints on this class of DM model.

The search for DM will continue for the forseeable future, but techniques will necessarily evolve as we enter the era of Big Data. Upgrades to the LHC, for example, will increase its luminosity by more than an order of magnitude [265], allowing for the exploration of previously inaccessible DM models. Vast amounts of data will also be collected by the upcoming Large Synoptic Survey Telescope [266], and will be used for precision tests of the ΛCDM cosmological model. As datasets become ever-larger, the use of modern statistical methods (i.e. machine learning) will increasingly supplant the traditional frameworks described here. But increased statistical power alone is only part of the solution: novel analyses, informed by continually revisiting our assumptions about DM, will continue to be vital as well.

# Bibliography


[1] M. Ackermann, W. B. Atwood, L. Baldini, et al. *Search for Gamma-Ray Emission from Local Primordial Black Holes with the Fermi Large Area Telescope.* The Astrophysical Journal, 857 (1): 49, **2018**. ISSN 0004-637X. doi: 10.3847/1538-4357/aaac7b.

[2] S. L. Glashow. *Partial-symmetries of weak interactions.* Nuclear Physics, 22 (4): 579–588, **1961**. ISSN 0029-5582. doi: 10.1016/0029-5582(61)90469-2.

[3] S. Weinberg. *A Model of Leptons.* Physical Review Letters, 19 (21): 1264–1266, **1967**. doi: 10.1103/PhysRevLett.19.1264.

[4] A. Salam. *Weak and Electromagnetic Interactions.* Conf.Proc., C680519: 367–377, **1968**.

[5] G. 't Hooft. *Renormalization of massless Yang-Mills fields.* Nuclear Physics B, 33 (1): 173–199, **1971**. ISSN 0550-3213. doi: 10.1016/0550-3213(71)90395-6.

[6] G. 't Hooft. *Renormalizable Lagrangians for massive Yang-Mills fields.* Nuclear

Physics B, 35 (1): 167–188, **1971**. ISSN 0550-3213. doi: 10.1016/0550-3213(71) 90139-8.

[7] The ATLAS Collaboration. *Observation of a new particle in the search for the Standard Model Higgs boson with the ATLAS detector at the LHC*. Physics Letters B, 716 (1): 1–29, **2012**. ISSN 03702693. doi: 10.1016/j.physletb.2012.08.020. ArXiv: 1207.7214.

[8] CMS Collaboration. *Observation of a new boson at a mass of 125 GeV with the CMS experiment at the LHC*. Physics Letters B, 716 (1): 30–61, **2012**. ISSN 03702693. doi: 10.1016/j.physletb.2012.08.021. ArXiv: 1207.7235.

[9] ATLAS and C. M. S. Collaborations. *Measurements of the Higgs boson production and decay rates and constraints on its couplings from a combined ATLAS and CMS analysis of the LHC pp collision data at $\sqrt{s} = 7$ and 8 TeV*. Journal of High Energy Physics, 2016 (8), **2016**. ISSN 1029-8479. doi: 10.1007/JHEP08(2016)045. ArXiv: 1606.02266.

[10] LIGO Scientific Collaboration and Virgo Collaboration, B. Abbott, R. Abbott, et al. *Observation of Gravitational Waves from a Binary Black Hole Merger*. Physical Review Letters, 116 (6): 061,102, **2016**. doi: 10.1103/PhysRevLett.116.061102.

[11] F. Zwicky. *On the Masses of Nebulae and of Clusters of Nebulae*. The Astrophysical Journal, 86: 217, **1937**. ISSN 0004-637X. doi: 10.1086/143864.

[12] F. D. Kahn and L. Woltjer. *Intergalactic Matter and the Galaxy.* The Astrophysical Journal, 130: 705, **1959**. ISSN 0004-637X. doi: 10.1086/146762.

[13] V. C. Rubin and W. K. Ford. *Rotation of the Andromeda Nebula from a Spectroscopic Survey of Emission Regions.* The Astrophysical Journal, 159: 379, **1970**. ISSN 0004-637X. doi: 10.1086/150317.

[14] M. S. Roberts and A. H. Rots. *Comparison of Rotation Curves of Different Galaxy Types.* Astronomy and Astrophysics, 26: 483–485, **1973**. ISSN 0004-6361.

[15] V. C. Rubin, W. K. Ford, and N. Thonnard. *Extended rotation curves of high-luminosity spiral galaxies. IV - Systematic dynamical properties, SA through SC.* The Astrophysical Journal, 225: L107–L111, **1978**. ISSN 0004-637X. doi: 10.1086/182804.

[16] J. F. Navarro, C. S. Frenk, and S. D. M. White. *The Structure of Cold Dark Matter Halos.* The Astrophysical Journal, 462: 563, **1996**. ISSN 0004-637X. doi: 10.1086/177173.

[17] M. Milgrom. *A modification of the Newtonian dynamics as a possible alternative to the hidden mass hypothesis.* The Astrophysical Journal, 270: 365–370, **1983**. ISSN 0004-637X. doi: 10.1086/161130.

[18] S. S. McGaugh. *The Baryonic Tully-Fisher Relation of Galaxies with Extended Rotation Curves and the Stellar Mass of Rotating Galaxies.* The Astrophysical

Journal, 632 (2): 859–871, **2005**. ISSN 0004-637X, 1538-4357. doi: 10.1086/432968. ArXiv: astro-ph/0506750.

[19] M. Bartelmann and P. Schneider. *Weak Gravitational Lensing.* Physics Reports, 340 (4-5): 291–472, **2001**. ISSN 03701573. doi: 10.1016/S0370-1573(00)00082-X. ArXiv: astro-ph/9912508.

[20] R. Mandelbaum. *Weak lensing for precision cosmology.* Annual Review of Astronomy and Astrophysics, 56 (1): 393–433, **2018**. ISSN 0066-4146, 1545-4282. doi: 10.1146/annurev-astro-081817-051928. ArXiv: 1710.03235.

[21] G. Soucail, Y. Mellier, B. Fort, et al. *Further data on the blue ring-like structure in A 370.* Astronomy and Astrophysics, 184: L7, **1987**. ISSN 0004-6361.

[22] G. Soucail, Y. Mellier, B. Fort, et al. *The giant arc in A 370 - Spectroscopic evidence for gravitational lensing from a source at Z = 0.724.* Astronomy and Astrophysics, 191: L19–L21, **1988**. ISSN 0004-6361.

[23] D. Clowe, M. Brada, A. H. Gonzalez, et al. *A Direct Empirical Proof of the Existence of Dark Matter.* The Astrophysical Journal Letters, 648 (2): L109, **2006**. ISSN 1538-4357. doi: 10.1086/508162.

[24] Particle Data Group, M. Tanabashi, K. Hagiwara, et al. *Review of Particle Physics.* Physical Review D, 98 (3): 030,001, **2018**. doi: 10.1103/PhysRevD.98.030001.

[25] D. N. Schramm and M. S. Turner. *Big-bang nucleosynthesis enters the precision*

*era*. Reviews of Modern Physics, 70 (1): 303–318, **1998**. ISSN 0034-6861, 1539-0756. doi: 10.1103/RevModPhys.70.303.

[26] Planck Collaboration, Y. Akrami, F. Arroja, et al. *Planck 2018 results. I. Overview and the cosmological legacy of Planck*. arXiv:1807.06205 [astro-ph], **2018**. ArXiv: 1807.06205.

[27] J. Einasto. *Dark Matter*. arXiv:0901.0632 [astro-ph], **2009**. ArXiv: 0901.0632.

[28] M. Kuhlen, M. Vogelsberger, and R. Angulo. *Numerical Simulations of the Dark Universe: State of the Art and the Next Decade*. arXiv:1209.5745 [astro-ph, physics:hep-ph], **2012**. ArXiv: 1209.5745.

[29] G. R. Blumenthal, S. M. Faber, J. R. Primack, et al. *Formation of galaxies and large-scale structure with cold dark matter*. Nature, 311 (5986): 517–525, **1984**. ISSN 1476-4687. doi: 10.1038/311517a0.

[30] P. van Dokkum, S. Danieli, Y. Cohen, et al. *A galaxy lacking dark matter*. Nature, 555 (7698): 629–632, **2018**. ISSN 1476-4687. doi: 10.1038/nature25767.

[31] J. L. Feng. *Dark Matter Candidates from Particle Physics and Methods of Detection*. Annual Review of Astronomy and Astrophysics, 48 (1): 495–545, **2010**. ISSN 0066-4146, 1545-4282. doi: 10.1146/annurev-astro-082708-101659. ArXiv: 1003.0904.

[32] G. 't Hooft. *Symmetry Breaking through Bell-Jackiw Anomalies*. Physical Review Letters, 37 (1): 8–11, **1976**. ISSN 0031-9007. doi: 10.1103/PhysRevLett.37.8.

[33] C. A. Baker, D. D. Doyle, P. Geltenbort, et al. *An Improved Experimental Limit on the Electric Dipole Moment of the Neutron.* Physical Review Letters, 97 (13), **2006**. ISSN 0031-9007, 1079-7114. doi: 10.1103/PhysRevLett.97.131801. ArXiv: hep-ex/0602020.

[34] J. E. Kim and G. Carosi. *Axions and the strong C P problem.* Reviews of Modern Physics, 82 (1): 557–601, **2010**. ISSN 0034-6861, 1539-0756. doi: 10.1103/RevModPhys.82.557.

[35] R. D. Peccei and H. R. Quinn. CP *Conservation in the Presence of Pseudoparticles.* Physical Review Letters, 38 (25): 1440–1443, **1977**. doi: 10.1103/PhysRevLett.38.1440.

[36] F. Wilczek. *Problem of Strong P and T Invariance in the Presence of Instantons.* Physical Review Letters, 40 (5): 279–282, **1978**. doi: 10.1103/PhysRevLett.40.279.

[37] S. Weinberg. *A New Light Boson?* Physical Review Letters, 40 (4): 223–226, **1978**. doi: 10.1103/PhysRevLett.40.223.

[38] M. Dine, W. Fischler, and M. Srednicki. *A simple solution to the strong CP problem with a harmless axion.* Physics Letters B, 104 (3): 199–202, **1981**. ISSN 0370-2693. doi: 10.1016/0370-2693(81)90590-6.

[39] D. Grosnick, S. C. Wright, R. D. Bolton, et al. *Search for the rare decay + e*

+ . Physical Review Letters, 57 (26): 3241–3244, **1986**. ISSN 0031-9007. doi: 10.1103/PhysRevLett.57.3241.

[40] G. G. Raffelt. *Astrophysical Axion Bounds.* arXiv:hep-ph/0611350, 741: 51–71, **2008**. doi: 10.1007/978-3-540-73518-2_3. ArXiv: hep-ph/0611350.

[41] G. Bertone. *Particle Dark Matter: Observations, Models and Searches.* Cambridge University Press, **2010**. doi: 10.1017/CBO9780511770739.

[42] E. Berkowitz, M. I. Buchoff, and E. Rinaldi. *Lattice QCD input for axion cosmology.* Physical Review D, 92 (3), **2015**. ISSN 1550-7998, 1550-2368. doi: 10.1103/PhysRevD.92.034507.

[43] M. Dine, P. Draper, L. Stephenson-Haskins, et al. *Axions, instantons, and the lattice.* Physical Review D, 96 (9): 095,001, **2017**. doi: 10.1103/PhysRevD.96.095001.

[44] A. J. Benson, A. Farahi, S. Cole, et al. *Dark Matter Halo Merger Histories Beyond Cold Dark Matter: I - Methods and Application to Warm Dark Matter.* Monthly Notices of the Royal Astronomical Society, 428 (2): 1774–1789, **2013**. ISSN 1365-2966, 0035-8711. doi: 10.1093/mnras/sts159. ArXiv: 1209.3018.

[45] ADMX Collaboration, N. Du, N. Force, et al. *Search for Invisible Axion Dark Matter with the Axion Dark Matter Experiment.* Physical Review Letters, 120 (15): 151,301, **2018**. doi: 10.1103/PhysRevLett.120.151301.

[46] P. Sikivie. *Experimental Tests of the "Invisible" Axion*. Physical Review Letters, 51 (16): 1415–1417, **1983**. doi: 10.1103/PhysRevLett.51.1415.

[47] D. J. H. Chung, P. Crotty, E. W. Kolb, et al. *On the gravitational production of superheavy dark matter*. Physical Review D, 64 (4), **2001**. ISSN 0556-2821, 1089-4918. doi: 10.1103/PhysRevD.64.043503. ArXiv: hep-ph/0104100.

[48] D. J. H. Chung, E. W. Kolb, and A. Riotto. *Nonthermal Supermassive Dark Matter*. Physical Review Letters, 81 (19): 4048–4051, **1998**. ISSN 0031-9007, 1079-7114. doi: 10.1103/PhysRevLett.81.4048. ArXiv: hep-ph/9805473.

[49] F. Tanedo. *Defense Against the Dark Arts*. page 81.

[50] M. S. T. Kolb, Edward W. *The Early Universe*. Number 69 in Frontiers in Physics. Addison-Wesley, **1990**.

[51] M. Hindmarsh and O. Philipsen. *WIMP Dark Matter and the QCD Equation of State*. Physical Review D, 71 (8), **2005**. ISSN 1550-7998, 1550-2368. doi: 10.1103/PhysRevD.71.087302. ArXiv: hep-ph/0501232.

[52] J. A. R. Cembranos, J. L. Feng, A. Rajaraman, et al. *Superweakly Interacting Massive Particle Solutions to Small Scale Structure Problems*. Physical Review Letters, 95 (18): 181,301, **2005**. doi: 10.1103/PhysRevLett.95.181301.

[53] J. L. Feng, S. Su, and F. Takayama. *Lower Limit on Dark Matter Production at the Large Hadron Collider*. Physical Review Letters, 96 (15), **2006**. ISSN 0031-9007, 1079-7114. doi: 10.1103/PhysRevLett.96.151802. ArXiv: hep-ph/0503117.

[54] CMS Collaboration. *Search for invisible decays of a Higgs boson produced through vector boson fusion in proton-proton collisions at $\sqrt{s} = 13$ TeV.* arXiv:1809.05937 [hep-ex], **2018**. ArXiv: 1809.05937.

[55] M. Felcini. *Searches for Dark Matter Particles at the LHC.* arXiv:1809.06341 [hep-ex, physics:hep-ph], **2018**. ArXiv: 1809.06341.

[56] CMS Collaboration. *Combined search for electroweak production of charginos and neutralinos in proton-proton collisions at $\sqrt{s} = 13$ TeV.* Journal of High Energy Physics, 2018 (3), **2018**. ISSN 1029-8479. doi: 10.1007/JHEP03(2018)160. ArXiv: 1801.03957.

[57] T. Behnke, J. E. Brau, B. Foster, et al. *The International Linear Collider Technical Design Report - Volume 1: Executive Summary.* arXiv:1306.6327 [hep-ph, physics:physics], **2013**. ArXiv: 1306.6327.

[58] H. Baer, T. Barklow, K. Fujii, et al. *The International Linear Collider Technical Design Report - Volume 2: Physics.* arXiv:1306.6352 [hep-ph], **2013**. ArXiv: 1306.6352.

[59] R. Bernabei, P. Belli, A. Bussolotti, et al. *First model independent results from DAMA/LIBRA-phase2.* arXiv:1805.10486 [astro-ph, physics:hep-ex, physics:physics], 19 (4), **2018**. doi: 10.15407/jnpae2018.04.307. ArXiv: 1805.10486.

[60] S. Baum, K. Freese, and C. Kelso. *Dark Matter implications of DAMA/LIBRA-*

*phase2 results*. Physics Letters B, 789: 262–269, **2019**. ISSN 0370-2693. doi: 10.1016/j.physletb.2018.12.036.

[61] B. W. Lee and S. Weinberg. *Cosmological Lower Bound on Heavy-Neutrino Masses*. Physical Review Letters, 39 (4): 165–168, **1977**. doi: 10.1103/PhysRevLett.39.165.

[62] E. Aprile, J. Aalbers, F. Agostini, et al. *Dark Matter Search Results from a One Tonne×Year Exposure of XENON1t*. Physical Review Letters, 121 (11), **2018**. ISSN 0031-9007, 1079-7114. doi: 10.1103/PhysRevLett.121.111302. ArXiv: 1805.12562.

[63] LUX Collaboration, D. Akerib, S. Alsum, et al. *Results from a Search for Dark Matter in the Complete LUX Exposure*. Physical Review Letters, 118 (2): 021,303, **2017**. doi: 10.1103/PhysRevLett.118.021303.

[64] PandaX-II Collaboration, X. Cui, A. Abdukerim, et al. *Dark Matter Results from 54-Ton-Day Exposure of PandaX-II Experiment*. Physical Review Letters, 119 (18): 181,302, **2017**. doi: 10.1103/PhysRevLett.119.181302.

[65] J. D. Vergados and H. Ejiri. *Can Solar Neutrinos be a Serious Background in Direct Dark Matter Searches?* Nuclear Physics B, 804 (1-2): 144–159, **2008**. ISSN 05503213. doi: 10.1016/j.nuclphysb.2008.06.004. ArXiv: 0805.2583.

[66] T. F.-L. Collaboration. *The Fermi Galactic Center GeV Excess and Implications*

*for Dark Matter.* The Astrophysical Journal, 840 (1): 43, **2017**. ISSN 1538-4357. doi: 10.3847/1538-4357/aa6cab. ArXiv: 1704.03910.

[67] IceCube Collaboration, M. G. Aartsen, M. Ackermann, et al. *Search for neutrinos from decaying dark matter with IceCube.* The European Physical Journal C, 78 (10), **2018**. ISSN 1434-6044, 1434-6052. doi: 10.1140/epjc/s10052-018-6273-3. ArXiv: 1804.03848.

[68] IceCube Collaboration, M. G. Aartsen, M. Ackermann, et al. *Search for Neutrinos from Dark Matter Self-Annihilations in the center of the Milky Way with 3 years of IceCube/DeepCore.* The European Physical Journal C, 77 (9), **2017**. ISSN 1434-6044, 1434-6052. doi: 10.1140/epjc/s10052-017-5213-y. ArXiv: 1705.08103.

[69] M. Aguilar, D. Aisa, B. Alpat, et al. *Precision Measurement of the ($e^+ + e^-$) Flux in Primary Cosmic Rays from 0.5 GeV to 1 TeV with the Alpha Magnetic Spectrometer on the International Space Station.* Physical Review Letters, 113 (22), **2014**. ISSN 0031-9007, 1079-7114. doi: 10.1103/PhysRevLett.113.221102.

[70] A. Ibarra, A. S. Lamperstorfer, and J. Silk. *Dark matter annihilations and decays after the AMS-02 positron measurements.* Physical Review D, 89 (6), **2014**. ISSN 1550-7998, 1550-2368. doi: 10.1103/PhysRevD.89.063539.

[71] J. Kopp. *Constraints on dark matter annihilation from AMS-02 results.* Physical Review D, 88 (7), **2013**. ISSN 1550-7998, 1550-2368. doi: 10.1103/PhysRevD.88.076013.

[72] T. Daylan, D. P. Finkbeiner, D. Hooper, et al. *The Characterization of the Gamma-Ray Signal from the Central Milky Way: A Compelling Case for Annihilating Dark Matter*. Physics of the Dark Universe, 12: 1–23, **2016**. ISSN 22126864. doi: 10.1016/j.dark.2015.12.005. ArXiv: 1402.6703.

[73] F. Calore, I. Cholis, and C. Weniger. *Background model systematics for the Fermi GeV excess*. Journal of Cosmology and Astroparticle Physics, 2015 (03): 038–038, **2015**. ISSN 1475-7516. doi: 10.1088/1475-7516/2015/03/038. ArXiv: 1409.0042.

[74] K. N. Abazajian, N. Canac, S. Horiuchi, et al. *Astrophysical and dark matter interpretations of extended gamma-ray emission from the Galactic Center*. Physical Review D, 90 (2): 023,526, **2014**. doi: 10.1103/PhysRevD.90.023526.

[75] F.-L. Collaboration. *Searching for Dark Matter Annihilation from Milky Way Dwarf Spheroidal Galaxies with Six Years of Fermi-LAT Data*. Physical Review Letters, 115 (23), **2015**. ISSN 0031-9007, 1079-7114. doi: 10.1103/PhysRevLett.115.231301. ArXiv: 1503.02641.

[76] E. Carlson, T. Linden, and S. Profumo. *Improved Cosmic-Ray Injection Models and the Galactic Center Gamma-Ray Excess*. Physical Review D, 94 (6), **2016**. ISSN 2470-0010, 2470-0029. doi: 10.1103/PhysRevD.94.063504. ArXiv: 1603.06584.

[77] R. Bartels, S. Krishnamurthy, and C. Weniger. *Strong Support for the Millisec-*

*ond Pulsar Origin of the Galactic Center GeV Excess*. Physical Review Letters, 116 (5): 051,102, **2016**. doi: 10.1103/PhysRevLett.116.051102.

[78] T. Sjöstrand, S. Mrenna, and P. Skands. *A Brief Introduction to PYTHIA 8.1*. Computer Physics Communications, 178 (11): 852–867, **2008**. ISSN 00104655. doi: 10.1016/j.cpc.2008.01.036. ArXiv: 0710.3820.

[79] T. E. Jeltema and S. Profumo. *Fitting the Gamma-Ray Spectrum from Dark Matter with DMFIT: GLAST and the Galactic Center Region*. Journal of Cosmology and Astroparticle Physics, 2008 (11): 003, **2008**. ISSN 1475-7516. doi: 10.1088/1475-7516/2008/11/003. ArXiv: 0808.2641.

[80] S. Hawking. *Gravitationally collapsed objects of very low mass*. Monthly Notices of the Royal Astronomical Society, 152: 75, **1971**. ISSN 0035-8711. doi: 10.1093/mnras/152.1.75.

[81] A. Polnarev and R. Zembowicz. *Formation of primordial black holes by cosmic strings*. Physical Review D, 43 (4): 1106–1109, **1991**. doi: 10.1103/PhysRevD.43.1106.

[82] K. Jedamzik and J. C. Niemeyer. *Primordial Black Hole Formation during First-Order Phase Transitions*. Physical Review D, 59 (12), **1999**. ISSN 0556-2821, 1089-4918. doi: 10.1103/PhysRevD.59.124014. ArXiv: astro-ph/9901293.

[83] S. Bird, I. Cholis, J. B. Muoz, et al. *Did LIGO detect dark matter?* Physi-

cal Review Letters, 116 (20), **2016**. ISSN 0031-9007, 1079-7114. doi: 10.1103/PhysRevLett.116.201301. ArXiv: 1603.00464.

[84] P. Pani and A. Loeb. *Tidal capture of a primordial black hole by a neutron star: implications for constraints on dark matter.* Journal of Cosmology and Astroparticle Physics, 2014 (06): 026–026, **2014**. ISSN 1475-7516. doi: 10.1088/1475-7516/2014/06/026. ArXiv: 1401.3025.

[85] B. Carr, F. Kuhnel, and M. Sandstad. *Primordial Black Holes as Dark Matter.* Physical Review D, 94 (8), **2016**. ISSN 2470-0010, 2470-0029. doi: 10.1103/PhysRevD.94.083504. ArXiv: 1607.06077.

[86] R. M. Wald. *General Rleativity.* The University of Chicago Press, **1984**. ISBN 978-0-226-87033-5.

[87] M. Schwartz. *Quantum Field Theory and the Standard Model.* Cambridge University Press, **2014**. ISBN 978-1-107-03473-0.

[88] F. Collaboration and W. B. Atwood. *The Large Area Telescope on the Fermi Gamma-ray Space Telescope Mission.* The Astrophysical Journal, 697 (2): 1071–1102, **2009**. ISSN 0004-637X, 1538-4357. doi: 10.1088/0004-637X/697/2/1071. ArXiv: 0902.1089.

[89] P. Morrison. *On gamma-ray astronomy.* Il Nuovo Cimento, 7: 858–865, **1958**. doi: 10.1007/BF02745590.

[90] R. Hillier. *Gamma ray astronomy.* Clarendon Press, Oxford, **1984**.

[91] W. L. Kraushaar, G. W. Clark, G. P. Garmire, et al. *High-Energy Cosmic Gamma-Ray Observations from the OSO-3 Satellite*. The Astrophysical Journal, 177: 341, **1972**. ISSN 0004-637X. doi: 10.1086/151713.

[92] C. E. Fichtel, R. C. Hartman, D. A. Kniffen, et al. *High-energy gamma-ray results from the second small astronomy satellite*. The Astrophysical Journal, 198: 163–182, **1975**. ISSN 0004-637X. doi: 10.1086/153590.

[93] W. Hermsen. *Gamma-ray sources observed by COS-B*. Space Science Reviews, 36: 61–92, **1983**. ISSN 0038-6308. doi: 10.1007/BF00171902.

[94] G. Kanbach, D. L. Bertsch, C. E. Fichtel, et al. *The project EGRET (Energetic Gamma-Ray Experiment Telescope) on NASA's Gamma-Ray Observatory (GRO)*. Space Science Reviews, 49: 69–84, **1988**. ISSN 0038-6308.

[95] M. Tavani. *The AGILE Mission*. Astronomy & Astrophysics, 502 (3): 995–1013, **2009**. ISSN 0004-6361, 1432-0746. doi: 10.1051/0004-6361/200810527. ArXiv: 0807.4254.

[96] W. Atwood. *Gamma Large Area Silicon Telescope (GLAST) applying silicon strip detector technology to the detection of gamma rays in space*. Nuclear Instruments and Methods in Physics Research Section A: Accelerators, Spectrometers, Detectors and Associated Equipment, 342 (1): 302–307, **1994**. ISSN 01689002. doi: 10.1016/0168-9002(94)91444-3.

[97] C. Meegan, G. Lichti, P. N. Bhat, et al. *The Fermi Gamma-Ray Burst Monitor*.

The Astrophysical Journal, 702 (1): 791–804, **2009**. ISSN 0004-637X, 1538-4357. doi: 10.1088/0004-637X/702/1/791. ArXiv: 0908.0450.

[98] M. Takahashi, R. Caputo, D. Paneque, et al. *Calorimeter-only analysis of the Fermi Large Area Telescope*. arXiv:1503.01364 [astro-ph], **2015**. ArXiv: 1503.01364.

[99] Fermi-LAT Collaboration. *The Fermi Large Area Telescope On Orbit: Event Classification, Instrument Response Functions, and Calibration*. The Astrophysical Journal Supplement Series, 203 (1): 4, **2012**. ISSN 0067-0049, 1538-4365. doi: 10.1088/0067-0049/203/1/4. ArXiv: 1206.1896.

[100] R. D. Evans. *The Atomic Nucleus*. McGraw-Hill, **1955**.

[101] G. R. Lynch and O. I. Dahl. *Approximations to multiple Coulomb scattering*. Nuclear Instruments and Methods in Physics Research Section B: Beam Interactions with Materials and Atoms, 58 (1): 6–10, **1991**. ISSN 0168-583X. doi: 10.1016/0168-583X(91)95671-Y.

[102] J. E. Grove and Fermi LAT Collaboration. *Pass 8: Transforming the Scientific Performance of the Fermi Large Area Telescope*. volume 223, page 256.03. **2014**.

[103] `https://www.slac.stanford.edu/exp/glast/groups/canda/lat_Performance.htm`.

[104] R. Rando and f. t. F. L. Collaboration. *Post-launch performance of the Fermi Large Area Telescope*. arXiv:0907.0626 [astro-ph], **2009**. ArXiv: 0907.0626.

[105] J. Bregeon, E. Charles, and M. W. f. t. F.-L. Collaboration. *Fermi-LAT data reprocessed with updated calibration constants*. **2013**.

[106] W. Hillebrandt and J. C. Niemeyer. *Type Ia Supernova Explosion Models*. Annual Review of Astronomy and Astrophysics, 38 (1): 191–230, **2000**. ISSN 0066-4146, 1545-4282. doi: 10.1146/annurev.astro.38.1.191. ArXiv: astro-ph/0006305.

[107] M.-H. Ulrich, L. Maraschi, and C. M. Urry. *Variability of Active Galactic Nuclei*. Annual Review of Astronomy and Astrophysics, 35: 445–502, **1997**. ISSN 0066-4146. doi: 10.1146/annurev.astro.35.1.445.

[108] M. Ackermann, M. Ajello, A. Albert, et al. *Multiwavelength Evidence for Quasi-periodic Modulation in the Gamma-Ray Blazar PG 1553+113*. The Astrophysical Journal Letters, 813 (2): L41, **2015**. ISSN 2041-8205. doi: 10.1088/2041-8205/813/2/L41.

[109] R. E. Lingenfelter. *Cosmic Ray Origin and Propagation*. International Cosmic Ray Conference, 14: 135, **1979**.

[110] A. R. Bell. *The acceleration of cosmic rays in shock fronts  I*. Monthly Notices of the Royal Astronomical Society, 182 (2): 147–156, **1978**. ISSN 0035-8711. doi: 10.1093/mnras/182.2.147.

[111] F. Acero, M. Ackermann, M. Ajello, et al. *Development of the Model of Galactic Interstellar Emission for Standard Point-Source Analysis of \Fermi Large Area*

*Telescope Data.* The Astrophysical Journal Supplement Series, 223 (2): 26, **2016**. ISSN 1538-4365. doi: 10.3847/0067-0049/223/2/26.

[112] A. Loeb and E. Waxman. *Cosmic -ray background from structure formation in the intergalactic medium.* Nature, 405 (6783): 156–158, **2000**. ISSN 1476-4687. doi: 10.1038/35012018.

[113] A. A. Abdo, M. Ackermann, M. Ajello, et al. *Spectrum of the Isotropic Diffuse Gamma-Ray Emission Derived from First-Year Fermi Large Area Telescope Data.* Phys. Rev. Lett., 104 (10): 101,101, **2010**. doi: 10.1103/PhysRevLett.104.101101.

[114] R. Blandford, D. Meier, and A. Readhead. *Relativistic Jets in Active Galactic Nuclei.* arXiv:1812.06025 [astro-ph], **2018**. ArXiv: 1812.06025.

[115] R. D. Blandford and R. L. Znajek. *Electromagnetic extraction of energy from Kerr black holes.* Monthly Notices of the Royal Astronomical Society, 179: 433–456, **1977**. ISSN 0035-8711. doi: 10.1093/mnras/179.3.433.

[116] D. Bhakta, J. S. Deneva, D. A. Frail, et al. *Searching for pulsars associated with the Fermi GeV excess.* Monthly Notices of the Royal Astronomical Society, 468 (3): 2526–2531, **2017**. ISSN 0035-8711, 1365-2966. doi: 10.1093/mnras/stx656.

[117] C. van Eldik. *Gamma rays from the Galactic Centre region: A review.* Astroparticle Physics, 71: 45–70, **2015**. ISSN 0927-6505. doi: 10.1016/j.astropartphys.2015.05.002.

[118] M. Morris and E. Serabyn. *The Galactic Center Environment.* Annual Review

of Astronomy and Astrophysics, 34 (1): 645–701, **1996**. doi: 10.1146/annurev.astro.34.1.645.

[119] S. S. Wilks. *The Large-Sample Distribution of the Likelihood Ratio for Testing Composite Hypotheses.* The Annals of Mathematical Statistics, 9 (1): 60–62, **1938**. ISSN 0003-4851, 2168-8990. doi: 10.1214/aoms/1177732360.

[120] F. Acero, M. Ackermann, M. Ajello, et al. *Fermi Large Area Telescope Third Source Catalog.* The Astrophysical Journal Supplement Series, 218: 23, **2015**. ISSN 0067-0049. doi: 10.1088/0067-0049/218/2/23.

[121] D. Schoonenberg, J. Gaskins, G. Bertone, et al. *Dark matter subhalos and unidentified sources in the Fermi 3fgl source catalog.* Journal of Cosmology and Astroparticle Physics, 2016 (05): 028–028, **2016**. ISSN 1475-7516. doi: 10.1088/1475-7516/2016/05/028. ArXiv: 1601.06781.

[122] K. M. Gorski, E. Hivon, A. J. Banday, et al. *HEALPix: A Framework for High-Resolution Discretization and Fast Analysis of Data Distributed on the Sphere.* The Astrophysical Journal, 622: 759–771, **2005**. doi: 10.1086/427976.

[123] M. Ajello. *Fermi-LAT Observations of High-Energy Gamma-Ray Emission Toward the Galactic Center.* The Astrophysical Journal, 819 (1): 44, **2016**.

[124] LAT Collaboration. *3fhl: The Third Catalog of Hard Fermi-LAT Sources.* **2017**. doi: 10.3847/1538-4365/aa8221.

[125] J. Michell. *On the means of discovering the distance, magnitude, &c. of the*

*fixed stars, in consequence of the diminution of the velocity of their light, in case such a diminution should be found to take place in any of them, and such other data should be procured from observations, as would be farther necessary for that purpose.* Philosophical Transactions of the Royal Society of London, 74, **1784**. doi: 10.1098/rstl.1784.0008.

[126] T. Do, G. D. Martinez, S. Yelda, et al. *3d stellar kinematics at the Galactic center: measuring the nuclear star cluster spatial density profile, black hole mass, and distance.* The Astrophysical Journal, 779 (1): L6, **2013**. ISSN 2041-8205, 2041-8213. doi: 10.1088/2041-8205/779/1/L6. ArXiv: 1311.0886.

[127] A. Einstein. *The Field Equations of Gravitation.* Sitzungsber. Preuss. Akad. Wiss. Berlin (Math. Phys.), 1915: 844–847, **1915**.

[128] K. Schwarzschild. *On the Gravitational Field of a Point-Mass, According to Einsteins Theory.* 1: 11, **1916**.

[129] A. Einstein. *On a Stationary System With Spherical Symmetry Consisting of Many Gravitating Masses.* Annals of Mathematics, 40 (4): 922–936, **1939**. ISSN 0003-486X. doi: 10.2307/1968902.

[130] S. Chandrasekhar. *The Maximum Mass of Ideal White Dwarfs.* The Astrophysical Journal, 74: 81, **1931**. ISSN 0004-637X. doi: 10.1086/143324.

[131] B. L. Webster and P. Murdin. *Cygnus X-1a Spectroscopic Binary with a Heavy*

*Companion ?* Nature, 235 (5332): 37–38, **1972**. ISSN 1476-4687. doi: 10.1038/235037a0.

[132] D. R. Gies and C. T. Bolton. *The optical spectrum of HDE 226868 = Cygnus X-1. II Spectrophotometry and mass estimates.* The Astrophysical Journal, 304: 371–393, **1986**. ISSN 0004-637X. doi: 10.1086/164171.

[133] T. Shahbaz, F. A. Ringwald, J. C. Bunn, et al. *The mass of the black hole in V404 Cygni.* Monthly Notices of the Royal Astronomical Society, 271 (1): L10–L14, **1994**. ISSN 0035-8711. doi: 10.1093/mnras/271.1.L10.

[134] F. Halzen, E. Zas, J. H. MacGibbon, et al. *Gamma rays and energetic particles from primordial black holes.* Nature, 353 (6347): 807–815, **1991**. ISSN 1476-4687. doi: 10.1038/353807a0.

[135] R. Genzel, N. Thatte, A. Krabbe, et al. *The Dark Mass Concentration in the Central Parsec of the Milky Way.* The Astrophysical Journal, 472 (1): 153, **1996**. ISSN 0004-637X. doi: 10.1086/178051.

[136] A. M. Ghez, B. L. Klein, M. Morris, et al. *High Proper-Motion Stars in the Vicinity of Sagittarius A*: Evidence for a Supermassive Black Hole at the Center of Our Galaxy.* The Astrophysical Journal, 509 (2): 678, **1998**. ISSN 0004-637X. doi: 10.1086/306528.

[137] R.-S. Lu, F. Roelofs, V. L. Fish, et al. *Imaging an Event Horizon: Mitigation*

*of Source Variability of Sagittarius A*.* The Astrophysical Journal, 817 (2): 173, **2016**. ISSN 1538-4357. doi: 10.3847/0004-637X/817/2/173.

[138] S. W. Hawking. *Gravitational Radiation from Colliding Black Holes.* Physical Review Letters, 26 (21): 1344–1346, **1971**. doi: 10.1103/PhysRevLett.26.1344.

[139] J. D. Bekenstein. *Black Holes and Entropy.* Physical Review D, 7: 2333–2346, **1973**. ISSN 1550-7998. doi: 10.1103/PhysRevD.7.2333.

[140] S. W. Hawking. *Particle creation by black holes.* Communications in Mathematical Physics, 43: 199–220, **1975**. doi: 10.1007/BF02345020.

[141] S. A. Fulling. *Nonuniqueness of Canonical Field Quantization in Riemannian Space-Time.* Physical Review D, 7 (10): 2850–2862, **1973**. doi: 10.1103/PhysRevD.7.2850.

[142] P. C. W. Davies. *Scalar production in Schwarzschild and Rindler metrics.* Journal of Physics A: Mathematical and General, 8 (4): 609–616, **1975**. ISSN 0305-4470. doi: 10.1088/0305-4470/8/4/022.

[143] W. G. Unruh. *Notes on black-hole evaporation.* Physical Review D, 14 (4): 870–892, **1976**. doi: 10.1103/PhysRevD.14.870.

[144] J. H. MacGibbon. *Can Planck-mass relics of evaporating black holes close the Universe?* Nature, 329 (6137): 308–309, **1987**. ISSN 1476-4687. doi: 10.1038/329308a0.

[145] C. I. Agency. *The World Factbook.* Washington, DC, **2019**.

[146] S. W. Hawking. *Black hole explosions?* Nature, 248: 30–31, **1974**. doi: 10.1038/248030a0.

[147] D. N. Page and S. W. Hawking. *Gamma rays from primordial black holes.* The Astrophysical Journal, 206: 1–7, **1976**. doi: 10.1086/154350.

[148] R. Hagedorn. *Hadronic matter near the boiling point.* Nuovo Cimento A Serie, 56: 1027–1057, **1968**. doi: 10.1007/BF02751614.

[149] S. W. Hawking. *Black holes from cosmic strings.* Physics Letters B, 231 (3): 237–239, **1989**. ISSN 0370-2693. doi: 10.1016/0370-2693(89)90206-2.

[150] S. W. Hawking, I. G. Moss, and J. M. Stewart. *Bubble collisions in the very early universe.* Physical Review D, 26 (10): 2681–2693, **1982**. doi: 10.1103/PhysRevD.26.2681.

[151] P. H. Frampton, M. Kawasaki, F. Takahashi, et al. *Primordial Black Holes as All Dark Matter.* Journal of Cosmology and Astroparticle Physics, 2010 (04): 023–023, **2010**. ISSN 1475-7516. doi: 10.1088/1475-7516/2010/04/023. ArXiv: 1001.2308.

[152] R. Bean and J. Magueijo. *Could supermassive black holes be quintessential primordial black holes?* Physical Review D, 66 (6): 063,505, **2002**. doi: 10.1103/PhysRevD.66.063505.

[153] B. J. Carr, K. Kohri, Y. Sendouda, et al. *New cosmological constraints on primor-*

*dial black holes*. Physical Review D, 81 (10), **2010**. ISSN 1550-7998, 1550-2368. doi: 10.1103/PhysRevD.81.104019. ArXiv: 0912.5297.

[154] J. Bovy and S. Tremaine. *On the Local Dark Matter Density*. The Astrophysical Journal, 756: 89, **2012**. ISSN 0004-637X. doi: 10.1088/0004-637X/756/1/89.

[155] H. Niikura, M. Takada, N. Yasuda, et al. *Microlensing constraints on primordial black holes with the Subaru/HSC Andromeda observation*. arXiv:1701.02151 [astro-ph], **2017**. ArXiv: 1701.02151.

[156] A. Barnacka, J.-F. Glicenstein, and R. Moderski. *New constraints on primordial black holes abundance from femtolensing of gamma-ray bursts*. Physical Review D, 86 (4), **2012**. ISSN 1550-7998, 1550-2368. doi: 10.1103/PhysRevD.86.043001.

[157] G. M. Fuller, A. Kusenko, and V. Takhistov. *Primordial Black Holes and r - Process Nucleosynthesis*. Physical Review Letters, 119 (6), **2017**. ISSN 0031-9007, 1079-7114. doi: 10.1103/PhysRevLett.119.061101.

[158] J. Yoo, J. Chanam, and A. Gould. *The End of the MACHO Era: Limits on Halo Dark Matter from Stellar Halo Wide Binaries*. The Astrophysical Journal, 601 (1): 311, **2004**. ISSN 0004-637X. doi: 10.1086/380562.

[159] D. P. Quinn, M. I. Wilkinson, M. J. Irwin, et al. *On the reported death of the MACHO era*. Monthly Notices of the Royal Astronomical Society: Letters, 396 (1): L11–L15, **2009**. ISSN 1745-3933. doi: 10.1111/j.1745-3933.2009.00652.x.

[160] L. Spitzer, Jr. *Equipartition and the Formation of Compact Nuclei in Spherical*

*Stellar Systems.* The Astrophysical Journal Letters, 158: L139, **1969**. ISSN 0004-637X. doi: 10.1086/180451.

[161] T. D. Brandt. *Constraints on MACHO Dark Matter from Compact Stellar Systems in Ultra-Faint Dwarf Galaxies.* The Astrophysical Journal, 824 (2): L31, **2016**. ISSN 2041-8213. doi: 10.3847/2041-8205/824/2/L31. ArXiv: 1605.03665.

[162] The LIGO Scientific Collaboration and the Virgo Collaboration, B. P. Abbott, R. Abbott, et al. *GWTC-1: A Gravitational-Wave Transient Catalog of Compact Binary Mergers Observed by LIGO and Virgo during the First and Second Observing Runs.* arXiv:1811.12907 [astro-ph, physics:gr-qc], **2018**. ArXiv: 1811.12907.

[163] Y. B. Zel'dovich and I. D. Novikov. *The Hypothesis of Cores Retarded during Expansion and the Hot Cosmological Model.* Astronomicheskii Zhurnal, 43: 758, **1966**. ISSN 0004-6299.

[164] J. D. Bekenstein. *Generalized second law of thermodynamics in black-hole physics.* Physical Review D, 9: 3292–3300, **1974**. ISSN 1550-7998. doi: 10.1103/PhysRevD.9.3292.

[165] B. J. Carr. *Primordial Black Holes: Do They Exist and Are They Useful?* **2005**.

[166] M. Y. Khlopov. *Primordial black holes.* Research in Astronomy and Astrophysics, 10: 495–528, **2010**. doi: 10.1088/1674-4527/10/6/001.

[167] A. Linde, S. Mooij, and E. Pajer. *Gauge field production in supergravity inflation:*

*Local non-Gaussianity and primordial black holes.* Physical Review D, 87 (10): 103,506, **2013**. doi: 10.1103/PhysRevD.87.103506.

[168] J. H. MacGibbon. *Quark- and gluon-jet emission from primordial black holes. II. The emission over the black-hole lifetime.* Physical Review D, 44: 376–392, **1991**. doi: 10.1103/PhysRevD.44.376.

[169] B. J. Carr and J. H. MacGibbon. *Cosmic rays from primordial black holes and constraints on the early universe.* Physics Reports, 307: 141–154, **1998**. ISSN 0370-1573. doi: 10.1016/S0370-1573(98)00039-8.

[170] R. Lehoucq, M. Cass, J.-M. Casandjian, et al. *New constraints on the primordial black hole number density from Galactic -ray astronomy.* Astronomy & Astrophysics, 502: 37–43, **2009**. doi: 10.1051/0004-6361/200911961.

[171] G. Tei and VERITAS Collaboration. *Searching for primordial black holes with the VERITAS gamma-ray experiment.* Journal of Physics Conference Series, 375 (5): 052,024, **2012**. doi: 10.1088/1742-6596/375/1/052024.

[172] J. Glicenstein, A. Barnacka, M. Vivier, et al. *Limits on Primordial Black Hole evaporation with the H.E.S.S. array of Cherenkov telescopes.* ArXiv: 1307.4898, **2013**.

[173] A. A. Abdo, A. U. Abeysekara, R. Alfaro, et al. *Milagro limits and HAWC sensitivity for the rate-density of evaporating Primordial Black Holes.* Astroparticle

Physics, 64: 4–12, **2015**. ISSN 0927-6505. doi: 10.1016/j.astropartphys.2014.10.007.

[174] C. E. Fichtel, D. L. Bertsch, B. L. Dingus, et al. *Search of the energetic gamma-ray experiment telescope (EGRET) data for high-energy gamma-ray microsecond bursts*. The Astrophysical Journal, 434: 557–559, **1994**. ISSN 0004-637X. doi: 10.1086/174758.

[175] M. J. Rees. *A better way of searching for black-hole explosions*. Nature, 266: 333, **1977**. doi: 10.1038/266333a0.

[176] S. E. Cutchin, J. H. Simonetti, S. W. Ellingson, et al. *Constraining the Rate of Primordial Black Hole Explosions and Extra-Dimension Scale Using a Low-Frequency Radio Antenna Array*. Publications of the Astronomical Society of the Pacific, 127: 1269, **2015**. ISSN 0004-6280. doi: 10.1086/684195.

[177] R. D. Blandford. *Spectrum of a radio pulse from an exploding black hole*. Monthly Notices of the Royal Astronomical Society, 181: 489–498, **1977**. ISSN 0035-8711. doi: 10.1093/mnras/181.3.489.

[178] J. H. MacGibbon and B. J. Carr. *Cosmic rays from primordial black holes*. The Astrophysical Journal, 371: 447–469, **1991**. doi: 10.1086/169909.

[179] J. H. MacGibbon, T. N. Ukwatta, J. T. Linnemann, et al. *Primordial Black Holes*. 5th International Fermi Symposium Nagoya, Japan, October 20-24, 2014, **2015**.

[180] M. I. Wilkinson and N. W. Evans. *The present and future mass of the Milky Way*

*halo.* Monthly Notices of the Royal Astronomical Society, 310: 645–662, **1999**. doi: 10.1046/j.1365-8711.1999.02964.x.

[181] X. X. Xue, H. W. Rix, G. Zhao, et al. *The Milky Way's Circular Velocity Curve to 60 kpc and an Estimate of the Dark Matter Halo Mass from the Kinematics of 2400 SDSS Blue Horizontal-Branch Stars.* The Astrophysical Journal, 684: 1143–1158, **2008**. doi: 10.1086/589500.

[182] Y. Sofue, M. Honma, and T. Omodaka. *Unified Rotation Curve of the Galaxy Decomposition into de Vaucouleurs Bulge, Disk, Dark Halo, and the 9-kpc Rotation Dip* . Publications of the Astronomical Society of Japan, 61: 227–236, **2009**. doi: 10.1093/pasj/61.2.227.

[183] O. Y. Gnedin, W. R. Brown, M. J. Geller, et al. *The Mass Profile of the Galaxy to 80 kpc.* Astrophysical Journal Letters, 720: L108–L112, **2010**. doi: 10.1088/2041-8205/720/1/L108.

[184] P. J. McMillan and J. J. Binney. *The uncertainty in Galactic parameters.* Monthly Notices of the Royal Astronomical Society, 402: 934–940, **2010**. doi: 10.1111/j.1365-2966.2009.15932.x.

[185] P. J. McMillan. *Mass models of the Milky Way.* Monthly Notices of the Royal Astronomical Society, 414: 2446–2457, **2011**. doi: 10.1111/j.1365-2966.2011.18564.x.

[186] M. Kuhlen, N. Weiner, J. Diemand, et al. *Dark matter direct detection with non-*

*Maxwellian velocity structure*. Journal of Cosmology and Astroparticle Physics, 2: 030, **2010**. doi: 10.1088/1475-7516/2010/02/030.

[187] T. N. Ukwatta, D. R. Stump, J. T. Linnemann, et al. *Primordial Black Holes: Observational characteristics of the final evaporation*. Astroparticle Physics, 80: 90–114, **2016**. doi: 10.1016/j.astropartphys.2016.03.007.

[188] M. Ackermann, M. Ajello, W. B. Atwood, et al. *The Third Catalog of Active Galactic Nuclei Detected by the Fermi Large Area Telescope*. The Astrophysical Journal, 810: 14, **2015**. ISSN 0004-637X. doi: 10.1088/0004-637X/810/1/14.

[189] A. Allafort, Y. T. Tanaka, N. Omodei, et al. *Fermi LAT detection of increased gamma-ray emission from the vicinity of the Sun*. The Astronomer's Telegram, 3214, **2011**.

[190] S. Archambault. *Search for Primordial Black Hole Evaporation with VERITAS*. In *Proceedings of 35th International Cosmic Ray Conference PoS(ICRC2017)*, volume 301, page 691. SISSA Medialab, **2018**. doi: 10.22323/1.301.0691.

[191] A. D. Dolgov and S. I. Blinnikov. *Stars and black holes from the very early universe*. Physical Review D, 89 (2): 021,301, **2014**. doi: 10.1103/PhysRevD.89.021301.

[192] G. Hinshaw, D. Larson, E. Komatsu, et al. *Nine-year Wilkinson Microwave Anisotropy Probe (WMAP) Observations: Cosmological Parameter Results*. As-

trophysical Journal, Supplement, 208: 19, **2013**. doi: 10.1088/0067-0049/208/2/19.

[193] A. S. Josan and A. M. Green. *Constraints from primordial black hole formation at the end of inflation.* Physical Review D, 82 (4): 047,303, **2010**. doi: 10.1103/PhysRevD.82.047303.

[194] E. Torres-Lomas and L. A. Urea-Lpez. *Primordial black hole production during preheating in a chaotic inflationary model.* volume 1548 of *American Institute of Physics Conference Series*, pages 238–243. **2013**. doi: 10.1063/1.4817051.

[195] T. P. Robitaille, E. J. Tollerud, P. Greenfield, et al. *Astropy: A community Python package for astronomy.* Astronomy & Astrophysics, 558: A33, **2013**. doi: 10.1051/0004-6361/201322068.

[196] J. D. Hunter. *Matplotlib: A 2d graphics environment.* Computing In Science & Engineering, 9 (3): 90–95, **2007**. doi: 10.1109/MCSE.2007.55.

[197] J. H. MacGibbon and B. R. Webber. *Quark- and gluon-jet emission from primordial black holes: The instantaneous spectra.* Physical Review D, 41: 3052–3079, **1990**. doi: 10.1103/PhysRevD.41.3052.

[198] T. U. Ukwatta, D. Stump, J. T. Linnemann, et al. *Milagro Limits on the Rate-Density of Primordial Black Holes.* ArXiv:1308.4912, **2013**.

[199] E. Bugaev, P. Klimai, and V. Petkov. *Photon spectra from final stages of a primordial black hole evaporation in different theoretical models.* In *Proceedings*

*of the 30th International Cosmic Ray Conference*, volume 3, pages 1123–1126. Mexico City, Mexico, **2008**.

[200] V. B. Petkov, E. V. Bugaev, P. A. Klimai, et al. *Searching for very-high-energy gamma-ray bursts from evaporating primordial black holes.* Astronomy Letters, 34: 509–514, **2008**. doi: 10.1134/S106377370808001X.

[201] M. Pospelov, A. Ritz, and M. B. Voloshin. *Secluded WIMP Dark Matter.* Physics Letters B, 662 (1): 53–61, **2008**. ISSN 03702693. doi: 10.1016/j.physletb.2008.02.052. ArXiv: 0711.4866.

[202] J. Shelton, S. L. Shapiro, and B. D. Fields. *A black hole window into p-wave dark matter annihilation.* Physical Review Letters, 115 (23), **2015**. ISSN 0031-9007, 1079-7114. doi: 10.1103/PhysRevLett.115.231302. ArXiv: 1506.04143.

[203] J. Sakurai and J. Napolitano. *Modern Quantum Mechanics.* Addison-Wesley, 2nd edition, **2011**. ISBN 978-0-8053-8291-4.

[204] Julio F. Navarro, Carlos S. Frenk, and Simon D. M. White. *A Universal Density Profile from Hierarchical Clustering - IOPscience.* The Astrophysical Journal, 490 (2), **1997**. doi: 10.1086/304888.

[205] F. Governato, A. Zolotov, A. Pontzen, et al. *Cuspy No More: How Outflows Affect the Central Dark Matter and Baryon Distribution in Lambda CDM Galaxies.* Monthly Notices of the Royal Astronomical Society, 422 (2): 1231–1240, **2012**. ISSN 00358711. doi: 10.1111/j.1365-2966.2012.20696.x. ArXiv: 1202.0554.

[206] B. Moore, F. Governato, T. Quinn, et al. *Resolving the Structure of Cold Dark Matter Halos.* The Astrophysical Journal Letters, 499 (1): L5, **1998**. ISSN 1538-4357. doi: 10.1086/311333.

[207] J. Diemand, M. Kuhlen, P. Madau, et al. *Clumps and streams in the local dark matter distribution.* Nature, 454: 735–738, **2008**. doi: 10.1038/nature07153.

[208] J. F. Navarro, A. Ludlow, V. Springel, et al. *The Diversity and Similarity of Cold Dark Matter Halos.* Mon. Not. Roy. Astron. Soc., 402: 21, **2010**. doi: 10.1111/j.1365-2966.2009.15878.x.

[209] P. Gondolo and J. Silk. *Dark matter annihilation at the galactic center.* Phys. Rev. Lett., 83: 1719–1722, **1999**. doi: 10.1103/PhysRevLett.83.1719.

[210] E. Vasiliev. *Dark matter annihilation near a black hole: Plateau vs. weak cusp.* Phys. Rev., D76: 103,532, **2007**. doi: 10.1103/PhysRevD.76.103532.

[211] S. L. Shapiro and J. Shelton. *Weak annihilation cusp inside the dark matter spike about a black hole.* Physical Review D, 93 (12): 123,510, **2016**. doi: 10.1103/PhysRevD.93.123510.

[212] O. Y. Gnedin, A. V. Kravtsov, A. A. Klypin, et al. *Response of dark matter halos to condensation of baryons: cosmological simulations and improved adiabatic contraction model.* The Astrophysical Journal, 616 (1): 16–26, **2004**. ISSN 0004-637X, 1538-4357. doi: 10.1086/424914. ArXiv: astro-ph/0406247.

[213] F. Zwicky. *Die Rotverschiebung von extragalaktischen Nebeln.* Helvetica Physica Acta, 6: 110–127, **1933**. ISSN 0018-0238.

[214] V. Rubin, N. Thonnard, and J. Ford, W.K. *Rotational properties of 21 SC galaxies with a large range of luminosities and radii, from NGC 4605 /R = 4kpc/ to UGC 2885 /R = 122 kpc/.* The Astrophysical Journal, 238: 471, **1980**. doi: 10.1086/158003.

[215] K. A. Olive. *TASI lectures on dark matter.* ArXiv e-prints, **2003**.

[216] Planck Collaboration, P. A. R. Ade, N. Aghanim, et al. *Planck 2013 results. XVI. Cosmological parameters.* ArXiv:1303.5076, **2013**.

[217] G. Steigman, B. Dasgupta, and J. F. Beacom. *Precise Relic WIMP Abundance and its Impact on Searches for Dark Matter Annihilation.* Phys. Rev., D86: 023,506, **2012**. doi: 10.1103/PhysRevD.86.023506.

[218] A. Albert, B. Anderson, K. Bechtol, et al. *Searching for Dark Matter Annihilation in Recently Discovered Milky Way Satellites with Fermi-Lat.* The Astrophysical Journal, 834 (2): 110, **2017**. ISSN 0004-637X. doi: 10.3847/1538-4357/834/2/110.

[219] M.-Y. Cui, Q. Yuan, Y.-L. S. Tsai, et al. *Possible Dark Matter Annihilation Signal in the AMS-02 Antiproton Data.* Physical Review Letters, 118 (19): 191,101, **2017**. doi: 10.1103/PhysRevLett.118.191101.

[220] D. Hooper, T. Linden, and P. Mertsch. *What does the PAMELA antiproton spectrum tell us about dark matter?* Journal of Cosmology and Astroparticle

Physics, 2015 (03): 021, **2015**. ISSN 1475-7516. doi: 10.1088/1475-7516/2015/03/021.

[221] J. S. Hagelin, G. L. Kane, and S. Raby. *Perhaps Scalar Neutrinos Are the Lightest Supersymmetric Partners*. Nucl. Phys., B241: 638–652, **1984**. doi: 10.1016/0550-3213(84)90064-6.

[222] Y. G. Kim and K. Y. Lee. *The Minimal model of fermionic dark matter*. Phys. Rev., D75: 115,012, **2007**. doi: 10.1103/PhysRevD.75.115012.

[223] Y. G. Kim, K. Y. Lee, and S. Shin. *Singlet fermionic dark matter*. JHEP, 05: 100, **2008**. doi: 10.1088/1126-6708/2008/05/100.

[224] S. Tulin, H.-B. Yu, and K. M. Zurek. *Beyond Collisionless Dark Matter: Particle Physics Dynamics for Dark Matter Halo Structure*. Phys. Rev., D87 (11): 115,007, **2013**. doi: 10.1103/PhysRevD.87.115007.

[225] J. A. Evans, S. Gori, and J. Shelton. *Looking for the WIMP Next Door*. JHEP, 02: 100, **2018**. doi: 10.1007/JHEP02(2018)100.

[226] R. Essig, E. Kuflik, S. D. McDermott, et al. *Constraining Light Dark Matter with Diffuse X-Ray and Gamma-Ray Observations*. JHEP, 11: 193, **2013**. doi: 10.1007/JHEP11(2013)193.

[227] R. Diamanti, L. Lopez-Honorez, O. Mena, et al. *Constraining Dark Matter Late-Time Energy Injection: Decays and P-Wave Annihilations*. JCAP, 1402: 017, **2014**. doi: 10.1088/1475-7516/2014/02/017.

[228] P. F. Depta, M. Hufnagel, K. Schmidt-Hoberg, et al. *BBN constraints on the annihilation of MeV-scale dark matter*. arXiv:1901.06944 [astro-ph, physics:hep-ph], **2019**. ArXiv: 1901.06944.

[229] H. An, M. B. Wise, and Y. Zhang. *Strong CMB Constraint On P-Wave Annihilating Dark Matter*. Phys. Lett., B773: 121–124, **2017**. doi: 10.1016/j.physletb.2017.08.010.

[230] O. Y. Gnedin and J. R. Primack. *Dark Matter Profile in the Galactic Center*. Phys. Rev. Lett., 93: 061,302, **2004**. doi: 10.1103/PhysRevLett.93.061302.

[231] M. Regis and P. Ullio. *Multi-wavelength signals of dark matter annihilations at the Galactic center*. Phys. Rev., D78: 043,505, **2008**. doi: 10.1103/PhysRevD.78.043505.

[232] B. D. Fields, S. L. Shapiro, and J. Shelton. *Galactic Center Gamma-Ray Excess from Dark Matter Annihilation: Is There A Black Hole Spike?* Phys. Rev. Lett., 113: 151,302, **2014**. doi: 10.1103/PhysRevLett.113.151302.

[233] T. Lacroix, C. Bhm, and J. Silk. *Ruling out thermal dark matter with a black hole induced spiky profile in the M87 galaxy*. Phys. Rev., D92 (4): 043,510, **2015**. doi: 10.1103/PhysRevD.92.043510.

[234] M. A. Amin and T. Wizansky. *Relativistic dark matter at the Galactic center*. Phys. Rev., D77: 123,510, **2008**. doi: 10.1103/PhysRevD.77.123510.

[235] M. Cannoni, M. E. Gomez, M. A. Perez-Garcia, et al. *New gamma ray signal*

*from gravitationally boosted neutralinos at the galactic center.* Phys. Rev., D85: 115,015, **2012**. doi: 10.1103/PhysRevD.85.115015.

[236] C. Arina, T. Bringmann, J. Silk, et al. *Enhanced Line Signals from Annihilating Kaluza-Klein Dark Matter.* Phys. Rev., D90 (8): 083,506, **2014**. doi: 10.1103/PhysRevD.90.083506.

[237] Fermi-LAT Collaboration. *Search for Gamma-ray Spectral Lines with the Fermi Large Area Telescope and Dark Matter Implications.* Physical Review D, 88: 082,002, **2013**. doi: 10.1103/PhysRevD.88.082002.

[238] M. Ackermann and others. *Updated search for spectral lines from Galactic dark matter interactions with pass 8 data from the Fermi Large Area Telescope.* Phys. Rev., D91 (12): 122,002, **2015**. doi: 10.1103/PhysRevD.91.122002.

[239] Y. Zhao, X.-J. Bi, P.-F. Yin, et al. *Constraint on the velocity dependent dark matter annihilation cross section from gamma-ray and kinematic observations of ultrafaint dwarf galaxies.* Phys. Rev., D97 (6): 063,013, **2018**. doi: 10.1103/PhysRevD.97.063013.

[240] L. Bergstrom and H. Snellman. *Observable Monochromatic Photons From Cosmic Photino Annihilation.* Phys. Rev., D37: 3737–3741, **1988**. doi: 10.1103/PhysRevD.37.3737.

[241] A. Ibarra, S. Lopez Gehler, and M. Pato. *Dark matter constraints from box-shaped*

*gamma-ray features*. JCAP, 1207: 043, **2012**. doi: 10.1088/1475-7516/2012/07/043.

[242] P. J. E. Peebles. *Gravitational collapse and related phenomena from an empirical point of view, or, black holes are where you find them.* General Relativity and Gravitation, 3: 63–82, **1972**. doi: 10.1007/BF00755923.

[243] T. Nakano and J. Makino. *On the cusp around central black holes in luminous elliptical galaxies*. The Astrophysical Journal, 525: L77, **1999**. doi: 10.1086/312338.

[244] P. Ullio, H. Zhao, and M. Kamionkowski. *A Dark matter spike at the galactic center?* Phys. Rev., D64: 043,504, **2001**. doi: 10.1103/PhysRevD.64.043504.

[245] D. Merritt. *Evolution of the dark matter distribution at the galactic center*. Phys. Rev. Lett., 92: 201,304, **2004**. doi: 10.1103/PhysRevLett.92.201304.

[246] D. Merritt, S. Harfst, and G. Bertone. *Collisionally Regenerated Dark Matter Structures in Galactic Nuclei*. Phys. Rev., D75: 043,517, **2007**. doi: 10.1103/PhysRevD.75.043517.

[247] S. L. Shapiro and V. Paschalidis. *Self-interacting dark matter cusps around massive black holes*. Phys. Rev., D89 (2): 023,506, **2014**. doi: 10.1103/PhysRevD.89.023506.

[248] G. R. Blumenthal, S. M. Faber, R. Flores, et al. *Contraction of Dark Matter*

*Galactic Halos Due to Baryonic Infall.* The Astrophysical Journal, 301: 27, **1986**. doi: 10.1086/163867.

[249] M. Gustafsson, M. Fairbairn, and J. Sommer-Larsen. *Baryonic Pinching of Galactic Dark Matter Haloes.* Phys. Rev., D74: 123,522, **2006**. doi: 10.1103/PhysRevD.74.123522.

[250] F. Iocco and M. Benito. *An estimate of the DM profile in the Galactic bulge region.* Phys. Dark Univ., 15: 90–95, **2017**. doi: 10.1016/j.dark.2016.12.004.

[251] D. Merritt. *Single and Binary Black Holes and their Influence on Nuclear Structure.* arXiv:astro-ph/0301257, **2003**. ArXiv: astro-ph/0301257.

[252] L. Sadeghian, F. Ferrer, and C. M. Will. *Dark matter distributions around massive black holes: A general relativistic analysis.* Phys. Rev., D88 (6): 063,522, **2013**. doi: 10.1103/PhysRevD.88.063522.

[253] R. Genzel, F. Eisenhauer, and S. Gillessen. *The Galactic Center Massive Black Hole and Nuclear Star Cluster.* Rev. Mod. Phys., 82: 3121–3195, **2010**. doi: 10.1103/RevModPhys.82.3121.

[254] A. M. Ghez and others. *Measuring Distance and Properties of the Milky Way's Central Supermassive Black Hole with Stellar Orbits.* The Astrophysical Journal, 689: 1044–1062, **2008**. doi: 10.1086/592738.

[255] N. J. McConnell and C.-P. Ma. *Revisiting the Scaling Relations of Black Hole

*Masses and Host Galaxy Properties*. The Astrophysical Journal, 764 (2): 184, **2013**.

[256] Y. Nomura and J. Thaler. *Dark Matter through the Axion Portal*. Phys. Rev., D79: 075,008, **2009**. doi: 10.1103/PhysRevD.79.075008.

[257] P. Ullio and L. Bergstrom. *Neutralino annihilation into a photon and a Z boson*. Phys. Rev., D57: 1962–1971, **1998**. doi: 10.1103/PhysRevD.57.1962.

[258] M. Perelstein and A. Spray. *Indirect Detection of Little Higgs Dark Matter*. Phys. Rev., D75: 083,519, **2007**. doi: 10.1103/PhysRevD.75.083519.

[259] M. Gustafsson, E. Lundstrom, L. Bergstrom, et al. *Significant Gamma Lines from Inert Higgs Dark Matter*. Phys. Rev. Lett., 99: 041,301, **2007**. doi: 10.1103/PhysRevLett.99.041301.

[260] J. M. Cline. *130 GeV dark matter and the Fermi gamma-ray line*. Phys. Rev., D86: 015,016, **2012**. doi: 10.1103/PhysRevD.86.015016.

[261] A. Rajaraman, T. M. P. Tait, and D. Whiteson. *Two Lines or Not Two Lines? That is the Question of Gamma Ray Spectra*. **2012**. doi: 10.1088/1475-7516/2012/09/003.

[262] F. James and M. Roos. *MINUIT: a system for function minimization and analysis of the parameter errors and corrections*. Comput. Phys. Commun., 10 (CERN-DD-75-20): 343–367. 38 p, **1975**.

[263] A. De Angelis, V. Tatischeff, M. Tavani, et al. *The e-ASTROGAM mission (exploring the extreme Universe with gamma rays in the MeV-GeV range).* Experimental Astronomy, 44 (1): 25–82, **2017**. ISSN 0922-6435, 1572-9508. doi: 10.1007/s10686-017-9533-6. ArXiv: 1611.02232.

[264] A. G. Cantrell, C. D. Bailyn, J. A. Orosz, et al. *The Inclination of the Soft X-ray Transient A0620–00 and the Mass of its Black Hole.* The Astrophysical Journal, 710 (2): 1127–1141, **2010**. ISSN 0004-637X, 1538-4357. doi: 10.1088/0004-637X/710/2/1127. ArXiv: 1001.0261.

[265] CERN. *CERN Yellow Reports: Monographs, Vol 4 (2017): High-Luminosity Large Hadron Collider (HL-LHC) Technical Design Report V. 0.1.* CERN, **2017**. doi: 10.23731/cyrm-2017-004.

[266] LSST Science Collaboration, P. A. Abell, J. Allison, et al. *LSST Science Book, Version 2.0.* ArXiv e-prints, **2009**.